Small-scale E-Region Irregularities in High-Latitude Plasma

A Thesis Submitted to the
College of Graduate and Postdoctoral Studies
in Partial Fulfillment of the Requirements
for the degree of Doctor of Philosophy
in the Department of Physics and Engineering Physics
Saskatoon

By

Siddhartha Choudhury

Permission to Use

In presenting this thesis in partial fulfilment of the requirements for a Postgraduate degree from the University of Saskatchewan, I agree that the Libraries of this University may make it freely available for inspection. I further agree that permission for copying of this thesis in any manner, in whole or in part, for scholarly purposes may be granted by the professor or professors who supervised my thesis work or, in their absence, by the Head of the Department or the Dean of the College in which my thesis work was done. It is understood that any copying or publication or use of this thesis or parts thereof for financial gain shall not be allowed without my written permission. It is also understood that due recognition shall be given to me and to the University of Saskatchewan in any scholarly use which may be made of any material in my thesis.

Requests for permission to copy or to make other use of material in this thesis in whole or part should be addressed to:

Dean
College of Graduate and Postdoctoral Studies
University of Saskatchewan
116 Thorvaldson Building, 110 Science Place
Saskatoon, Saskatchewan S7N 5C9
Canada

or

Head of the Department of Physics and Engineering Physics
116 Science Place
University of Saskatchewan
Saskatoon, Saskatchewan S7N 5E2
Canada

Abstract

Turbulence is pervasive in natural fluids. This includes rivers, the atmosphere, and the ionosphere, i.e., the plasma above 100 km altitude in the upper atmosphere. This thesis investigates ionospheric turbulence at altitudes between 100 and 120 km. In that region turbulence is triggered by Hall currents introduced by the fact that, given the presence of the geomagnetic field, ions and electrons respond very differently to electric fields of the kind that are found in the auroral regions. The turbulent properties of this region have been rather well characterized through numerous rocket flights and with ground-based radars observations. Turbulence in this case leads to the creation of large amplitude plasma density structures. This thesis focuses on the fact that the structures have been found over the years to move at velocities that are far slower than expected from the notion that they are driven by the electron motion and should therefore be moving at close to the so-called $\mathbf{E} \times \mathbf{B}$ drift introduced by the presence of electric fields. Based on fluid theory, this thesis offers an explanation for the slower motion making the point that it has to be due to electric field inside the density structures becoming increasingly small as their amplitude grows through the so-called Farley-Buneman instability mechanism. The electric field changes until the structures are moving so slowly that they can no longer grow in amplitude. Prior to getting into the new theory this thesis presents the context for the work. It starts with a discussion of plasmas, and more specifically ionospheric plasmas. It then goes over some of the salient properties observed by rocket instruments and ground-based radars. It then reviews how Hall currents create an unstable situation that leads to the growth of density structures. This is followed by a review of a subset of nonlinear theories that have attempted to explain the observations through nonlinear particle fluxes. The evolution in the theoretical thinking on this topic has lead to the development of the new theory presented in Chapter 5 of this thesis. The main highlights of the theory are that it offers an explanation for the decrease of the electric field inside structures on the basis of a notion of anomalous diffusion that had later evolved into the evolution of substructures that were described

through so-called mode-coupling theories and later on through the notion of an evolving tilt in the structures as they evolved. Based on the new theory I was able to calculate how and by what amount the turbulent structures make the average electric field smaller than the ambient field and how they change the currents in the medium. The theory has also been used here to calculate perturbed density and electric field profiles that look reasonable compared to observations although it does not perform as well in the lower part of the unstable region as it does near the top. A possible cause for this discrepancy could be that I did not take into account the fact that the lower part of the unstable region may well be affected by ambient density gradients associated with the bottom-side of the ionosphere.

Acknowledgements

I would like to express my deepest gratitude and thanks to my supervisor Dr. Jean-Pierre St.-Maurice to consider me as his graduate student and giving me the opportunity to work with him on Ionospheric irregularities as a subject to my thesis. His ideas and insight proved invaluable, and his guidance, support, and encouragements have helped me greatly throughout my studies and have allowed me to complete the work. His kindness, endless enthusiasm, and wisdom helped me to reach towards successful completion of the thesis.
I also thank the members of my thesis advisory committee, Prof. A. Kustov, Prof. A. Akkerman, Prof. Gap Soo Chang, Prof. Tom Steele, and Prof. Masoud Ghezelbash for their suggestions, guidance, and advice were key to help me complete this degree.

I have greatly appreciated my discussions with Prof. George Sofko and other members of ISAS, which always proved insightful and interesting. I also thank Dr. Ponomarenko for his constructive criticism and advice. It greatly helped my understanding. I also thank Kevin Kreiger, Gareth W. Perry, Ashton Reimer and every other member of the space and atmospheric physics group for an academic and friendly atmosphere. The same goes for the staff of the physics department (Cindy Jelinski, Debbie Gjertsen, and Marj Granrude)

My sincere thanks to Dr. Raj Kumar Choudhary and Prof. S.K. Dhaka will not be enough to express my gratitude. They have been great friends and excellent teachers who helped me in my efforts throughout my academic career.

Finally, without a doubt, I am indebted to my wife Sheli and our families for their moral support, tolerance, and understanding throughout the completion of this degree.

CONTENTS

List of Figures

List of Abbreviations

BARS	Bi-Static Auroral Radar System
CANOPUS	Canadian Auroral Network for the Open Program Unified Study
CASSIOPE	Cascade, Small Satellite, and Ionospheric Polar Explorer
CUPRI	Cornell University Portable Radar Interferometer
CW	Continuous Waves
EISCAT	European Incoherent Scatter
ERRRIS	E Region Rocket/Radar Instability Study
e-POP	Enhanced Polar Outflow Probe
EUV	Extreme ultra Violet
FB	Farley Buneman
FOV	Field of View
GD	Gradient Drift
GPS	Global Positioning Satellite
HF	High Frequency
IGRF	International Geomagnetic Reference Field
IGY	International Geophysical Year
ISAS	Institute of Space and Atmospheric Studies
ISR	Incoherent Scatter Radar
MLT	Magnetic Local Time
NASA	National Aeronautics and Space Administration
NL	Non-Linear
RADAR	Radio Detection and Ranging
RADARSAT	Radar Satellite
ROSE	Rocket and Scatter Experiments
SAR	Synthetic Aperture Radar
STARE	Scandinavian Twin Auroral Radar Experiment
STP	Standard Temperature and Pressure
SuperDARN	Super Dual Auroral Radar Network
UHF	Ultra High Frequency
UV	Ultra Violet
VHF	Very High Frequency
WKB	Wentzel, Kramers, and Brillouin

List of Symbols

$\mathbf{a}$	acceleration
α_d	flow angle
$\mathbf{B}$	magnetic Field
C_s	ion-acoustic speed
λ_D	Debye Length
$\mathbf{E}$	electric field
$\mathbf{E}_0$	ambient electric field
$\delta\mathbf{E}$	perturbed electric field
j	denotes species (electrons and ions)
k	Boltzman Constant
$\mathbf{k}$	wave vector
K	Kelvin Temperature
L	scale-length
m_i	mass of ions
nm	nano metre
n	number density of electrons and ions
n_0	number density at STP
n_j	number density of different species
δn	change in number density of electrons and ions
p	pressure
∇p	pressure gradient
q	charge
t	time
δt	change in time

List of Symbols

$\mathbf{V}$	velocity
$\mathbf{V}_e$	electron velocity
$\mathbf{V}_i$	ion velocity
$\delta\mathbf{V}_j$	perturbed velocity of species
ω	wave frequency
Ω	cyclotron frequency
x	position
ϵ_0	permittivity of free space
eV	electron Volt
T_e	electron temperature
T_i	ion temperature
$\mathbf{V}_{ph}$	phase velocity
$V_d = \lvert\mathbf{V_e} - \mathbf{V_i}\rvert$	
$\mathbf{V}_n$	neutral wind velocity
ρ	mass density
ν_j	collision frequency of different species
Ω_i	ion-cyclotron frequency
Ω_e	electron-cyclotron frequency
α	$\frac{\nu_i}{\Omega_i}\frac{1}{1+\Psi}$
$\mathbf{J}$	current density
$\delta\mathbf{J}$	change in current density
$\mathbf{E}^T$	Total electric field inside a blob or hole
γ	growth rate

Chapter 1

Introduction

1.1 Plasmas

A plasma is composed of charged particles exhibiting collective behavior. On the macroscopic scales, a plasma is generally in equilibrium aside from ion-electron beams. As charged particles move around, they can generate local enhancements of positive or negative charge subject to Coulomb forces. These local enhancements of positive and negative charges give rise to electric fields. The moving charged particles under the influence of electric fields, generate currents and subsequently, magnetic fields [*Chen*, 1996]. If these fields are strong enough, they start to affect the motion of the other charged particles in their surrounding.

What makes a plasma distinct from just an ordinary ionized gas is that in a plasma, positive charges, for example, are surrounded by dense clouds of electrons. There is a balance between the energy due to electrostatic attraction of electrons to a positive charge and the electron kinetic energy. Over a length described as the "Debye length", λ_D [*Gurnett and Bhattacharjee*, 2017], the influence of an isolated charge (a positive charge in the present example) is strongly shielded. Specifically, at a distance r from a given charge q, the potential that would be equal to $q/(4\pi\epsilon_0 r)$ in a vacuum now takes the form $qe^{-r/\lambda_D}/(4\pi\epsilon_0 r)$. An ionized gas becomes a plasma when its density is large enough for λ_D to be much smaller than the scales of interest in the system.

Owing to the dynamic shielding of individual charges over a Debye length, plasmas are considered to be the "fourth" state of matter. Weak long-range electrical forces remain, but at the same time, the gas is 'quasi-neutral' over distances larger than a Debye length. The charge equality is of course not perfect, but it amounts to a difference of one charge in more than one million in the ionospheric plasma [*Gurnett and Bhattacharjee*, 2017]. The remaining charge imbalance is enough

to produce electric fields and currents in response to applied electric fields or wind generators. The long-range forces are also known to introduce "collective" motions involving large groups of charged (but strongly shielded) particles. A plane wave description is often used to describe this collective behavior.

If an ordinary gas is heated to the point when the random kinetic energy of the molecules exceeds the ionization energy, a plasma gets produced. As a result of collisions, some of the electrons are knocked out of atoms, which in turn generates a mixture of electrons and ions. The ionization process requires energies of the order of 10 eV which is a high temperature compared to an ionospheric plasma of the kind dealt with in the present work. As is the case for planetary ionospheres, exposure of an ordinary gas to energetic photons in excess of 10 eV (such as in far ultraviolet light or X-rays) can generate a plasma. A balance between the ionization and recombination rates through chemical process, determines the steady-state ionization density of the various species. At the same time, the ionization source of the plasma has to be very strong to generate very high ionization in the medium. It might also be possible to maintain the degree of ionization if the medium is very tenuous which slows down the recombination rate [*Gurnett and Bhattacharjee*, 2017].

Plasmas are classified into two categories (natural and human-made). Almost 99 percent of the materials in the visible universe are in the state of plasma [*Gurnett and Bhattacharjee*, 2017]. The sun and most of the stars plus a significant amount of interstellar space is in the form of plasma. The Earth is surrounded by a medium comprised of neutral and non-neutral species (so called 'ionosphere'). This source of plasma is due to incoming ultraviolet and x-ray radiation from the Sun. Plasma is also present on the night-side of the earth when the recombination time-scale becomes very long. Due to Snell's law, the low-frequency radio waves used in communications get reflected from the ionosphere. Therefore, the ionosphere plays a vital role in radio-wave propagation [*Gurnett and Bhattacharjee*, 2017]. Earth is also surrounded by a region of magnetized plasma (magnetosphere) at higher altitudes.

Various applications of basic plasma physics are studied or used in human-made devices. Attempts to achieve controlled thermonuclear fusion is considered to be one of the most important applications of man-made devices. Controlled fusion involves very high temperatures. During the process of fusion, temperatures of the order of 10^7 K or more are required to overcome the

Coulomb repulsion. A fusion plasma can be quickly cooled by the walls of any ordinary container. Therefore considerable efforts have been made to contain plasmas through strong magnetic field using so-called "magnetic bottles" in earlier days and more recently so-called tokamaks [*Gurnett and Bhattacharjee*, 2017]. There are several other examples of human-made plasmas in laboratory applications that are of potential interest.

1.2 Interaction of the Solar Wind with the Magnetosphere

The solar wind is an outflow of high speed stream of particles from Sun's Corona into space. This extends far beyond the Earth's orbit until it becomes a weakly ionized gaseous medium (roughly around 1.5×10^{11} m). Although the most probable value of the solar wind speed is 500 km/s, it varies somewhere between 300 and 1400 km/s [*Baumjohann and Treumann*, 2012].

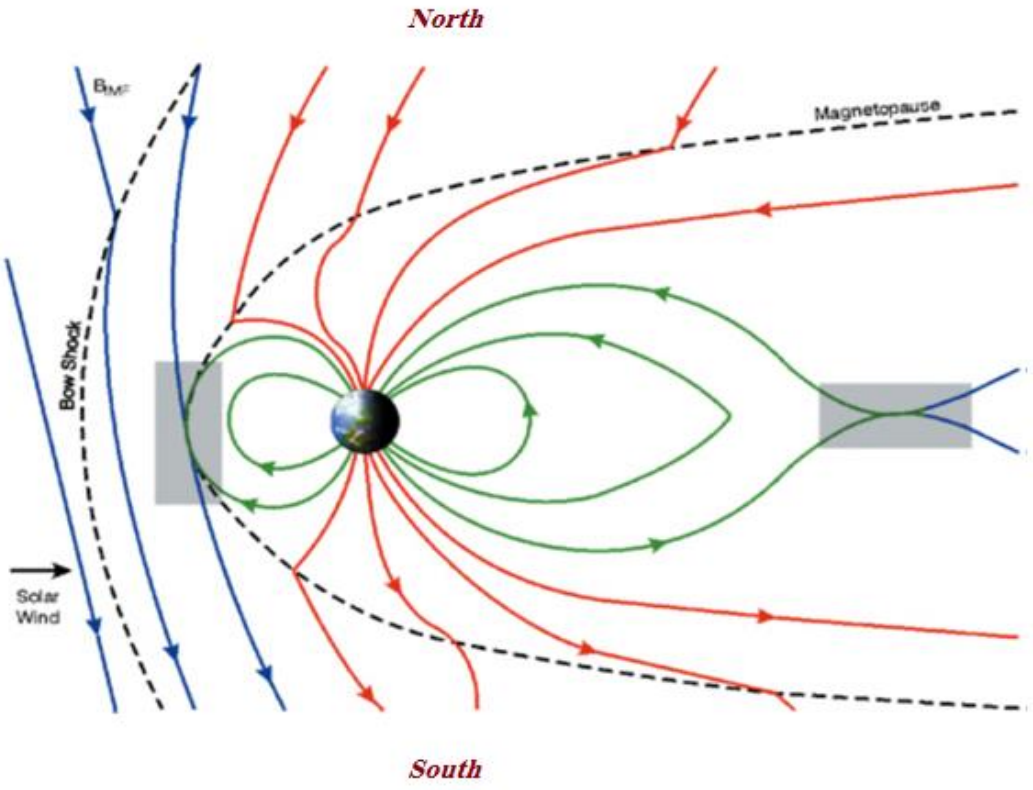

Figure 1.1: Solar Wind interaction with the Earth's magnetic field. Reproduced after *Baumjohann and Treumann* [2012]

The region where the Earth's dipolar magnetic field interacts with the solar wind, is called

the magnetosphere. The solar wind moves at supersonic speeds. A bow shock forms in front of the magnetosphere, and the solar wind plasma is decelerated at that point. Due to the interaction between the solar wind particles and the Earth's magnetosphere, the day-side magnetosphere is compressed and the magnetosphere towards the nightside is stretched towards the magnetotail [*Chian and Kamide*, 2007].

1.3 Ionospheric Currents and Conductivities

When a southward Inter Planetary Magnetic field (IMF) interacts with the magnetopause as shown in blue in fig. 1.1, the field line pattern shown in red in fig. 1.1 is generated. These open field lines have one end connected to the Earth with their other end joining towards the solar wind. The solar wind transports these red field lines across the polar cap region of Earth's ionosphere. After magnetic reconnection in the magnetotail the earth plasma returns to the dayside through what are now closed field lines via the auroral regions. For steady state equilibrium conditions, the field lines then end up to the front side of the magnetosphere and the cycle starts anew [*Baumjohann and Treumann*, 2012].

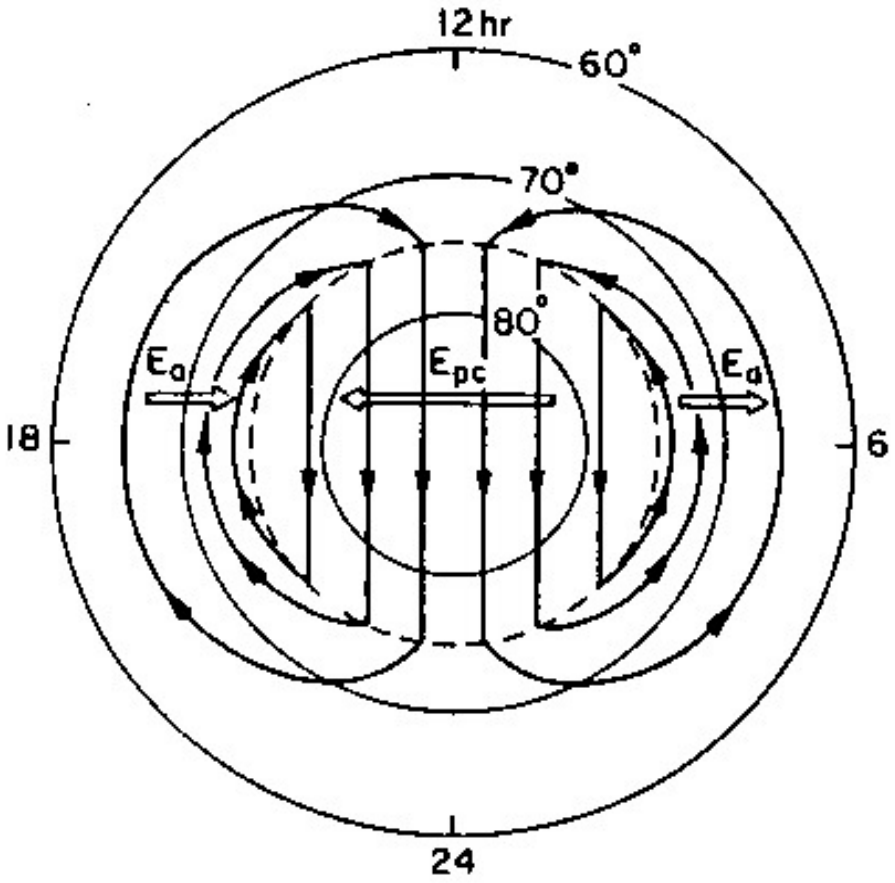

Figure 1.2: Convection pattern of ionospheric plasma at high latitude [*Kelley*, 2009]

At ionospheric altitudes the interaction just described sets up a 'convection pattern' which is described in cartoon form in Figure 1.2. From an observer sitting on the earth, this circulation is seen as originating from an electric field and the motion in regions where the cyclotron frequency is much greater than the collision frequency is described by an $\mathbf{E} \times \mathbf{B}$ drift.

1.3.1 Mobility and Electrical Conductivity

The collision frequency of ions and electrons in the ionosphere needs to be considered in order to assess the current systems that are associated with the auroral regions. The motion is described in terms of so-called mobilities and the mobilities are trivially related to the conductivity of the plasma.

Let's start with the hypothetical case of an isotropic plasma devoid of a magnetic field. Consider

first the electron case. The conductivity contribution from the electrons can be derived by equating the force due to the electric field and the electron-neutral collisions. If $-q$ is the charge we find that in a steady-state for this situation, we should have

$$-q\mathbf{E} - m_e \nu_{en} \mathbf{u}_e = 0 \tag{1.1}$$

$$\mathbf{u}_e = -\frac{q\mathbf{E}}{m_e \nu_{en}} \tag{1.2}$$

$$\mathbf{J}_e = -q n_e \mathbf{u}_e = \sigma_e \mathbf{E} \tag{1.3}$$

$$\sigma_e = \frac{q^2 n_e}{m_e \nu_{en}} = q n_e \mu_e \tag{1.4}$$

$$\mu_e = \frac{q}{m_e \nu_{en}} \tag{1.5}$$

Here $\mathbf{J}_e$ is the electric current density associated with electrons, m_e is the mass of the electrons, μ_e is the mobility of electrons, ν_{en} the electron-neutral collision frequency, $\mathbf{u}_e$ is the velocity of the electrons, and n_e is the number density of the electrons. Finally, σ_e is the electrical conductivity of the electrons. We have similar expressions for ions with a charge $+q$, namely,

$$q\mathbf{E} - m_i \nu_{in} \mathbf{u}_i = 0 \tag{1.6}$$

$$\mathbf{u}_i = \frac{q\mathbf{E}}{m_i \nu_{in}} \tag{1.7}$$

$$\mathbf{J}_i = q n_i \mathbf{u}_i = \sigma_i \mathbf{E} \tag{1.8}$$

$$\sigma_i = \frac{q^2 n_i}{m_i \nu_{in}} = q n_i \mu_i \tag{1.9}$$

$$\mu_i = \frac{q}{m_i \nu_{in}} \tag{1.10}$$

where J_i is the electric current density associated with ions, m_i is the mass of the ions, ν_{in} being the ion-neutral collision frequencies, μ_i being the mobility of ions, $\mathbf{u}_i$ is the velocity of the ions, and n_i being the number density of the ions and σ_i is the electrical conductivity of the ions. For a plasma with contributions from both positive and negative charges, the total conductivity (σ_0) due to electrons and ions can be written as,

$$\sigma_0 = q^2 \left[\frac{n_e}{m_e \nu_{en}} + \frac{n_i}{m_i \nu_{in}} \right] \tag{1.11}$$

With $\mu_e >> \mu_i$, we have $\sigma_0 \sim \frac{q^2 n_e}{m_e \nu_{en}}$. Detailed discussion about conductivities and mobilities have been introduced in *Ghosh* [2014].

In the presence of a magnetic field, the medium becomes anisotropic. There are now three conductivities. We use the words 'parallel conductivity' for the conductivity along the magnetic field, 'Pedersen conductivity' for the conductivity along the direction of an electric field that would be perpendicular to the magnetic field, and the word 'Hall conductivity' for the conductivity in the $\mathbf{E} \times \mathbf{B}$ direction. The parallel conductivity, $\sigma_{\parallel}$, and the parallel mobilities are given by the same expressions that were just presented for an isotropic plasma free of a magnetic field.

The ion and electron mobilities in the plane perpendicular to the magnetic field can be obtained by solving the momentum equations in the presence of the magnetic and electric forces and collisions. This is done in more detail later in this thesis. Suffice it to state here that the expressions can be viewed in many reference textbooks including *Baumjohann and Treumann* [2012]. For the electrons, the Pedersen conductivity, σ_{Pe}, and the Hall conductivity, σ_{He}, are given by

$$\sigma_{Pe} = \frac{{\nu_e}^2}{({\nu_e}^2 + {\Omega_e}^2)}\sigma_0 \tag{1.12}$$

$$\sigma_{He} = -\frac{\nu_e \Omega_e}{({\nu_e}^2 + {\Omega_e}^2)}\sigma_0 \tag{1.13}$$

$$\sigma_0 = \frac{n_e q^2}{m_e \nu_{en}} \tag{1.14}$$

$$\tag{1.15}$$

Similar expressions are obtained for the ions except for the fact that the Hall conductivity has a positive sign for the ions.

1.4 The Earth's Ionosphere

The Earth's ionosphere extends from 60 km to 1000 km in altitude beyond which the ionized medium is either referred to as the magnetosphere or, at lower latitudes, the plasmasphere. The ionosphere consists of a relatively large number of charged atoms and molecules. Various parts of the region respond differently to the solar radiation [*Russel*, 2014] through photo-ionization of neutral molecules by high-energy X-rays, ultraviolet (UV) and extreme-ultraviolet (EUV) radiation

coming from the sun. The balance between chemical production and recombination determines the net ionospheric densities in these regions. Importantly, one must also consider transport properties like diffusion and take into account the response of electric charges to the Earth's magnetic field in the process [*Schunk and Nagy*, 2009].

1.4.1 Ionospheric Regions

Ionospheric regions are mostly characterized by the reflection or refraction and sometimes diffraction of the waves propagating through the medium due to the presence of free electrons. The number of free electrons helps us determine the regions of high electron density as defined in the following order as D, E, F1 and F2 regions. As shown in Fig. 1.3, the D region extends between 50 and 90 km in altitude, and the E region extends between 90 and 150 km in altitude whereas the F region covers the region from 150 km altitude and above [e.g., *Schunk and Nagy*, 2009]. These regions will be discussed briefly in the following sub-sections.

It is from a historical perspective that the ionosphere has been described in terms of alphabetical layers. The E layer was detected first as result of experiments by Edward V. Appleton (also known as the Heaviside layer). The reason for his choice is not known for certain but it is thought that while describing the reflection of radio waves and the simultaneous electrification of the atmospheric medium, he probably used the letter E to represent the "electrification" of the atmosphere. The layers above and below were called F and D regions respectively. The D and F layers were named in this manner to maintain alphabetical extensions regarding their position. The F region was later further categorized and was divided into two distinct layers, namely, F1 and F2 layer [*Schunk and Nagy*, 2009].

1.4.2 Basic Ionospheric Properties

1.4.2.1 D-Region

As illustrated in Fig. 1.3, the D region ranges between 60 and 90 km altitude. Solar radiation of wavelength 122 nm causes the ionization (Lyman-alpha radiation) in the D region. The plasma density in the D region usually varies between 10^7 to 10^9 electrons per m^3 during the day. Due to the absence of solar photons, the D region quickly disappears after sunset [*Endawoke*, 2018,

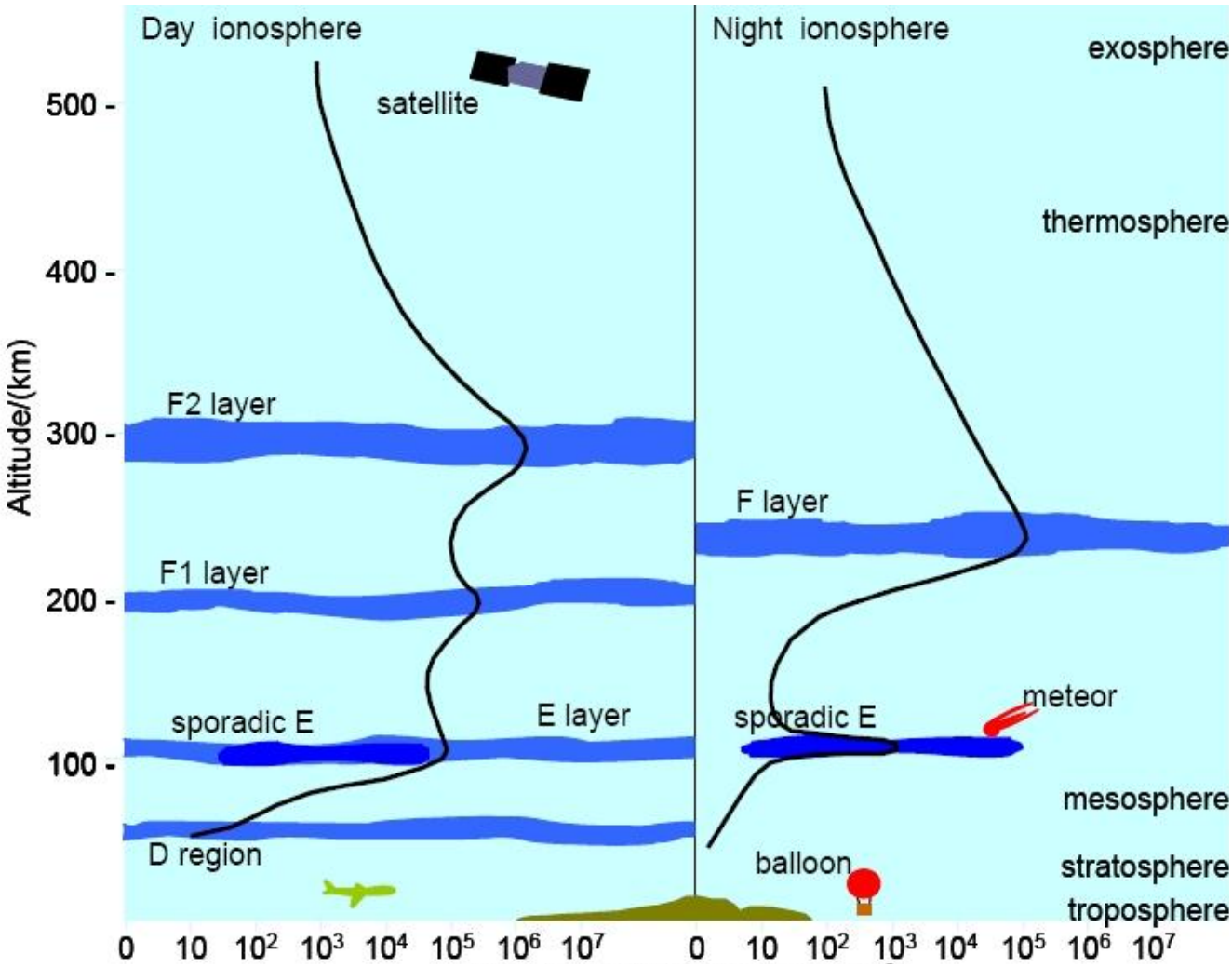

Figure 1.3: Diagram showing the various ionospheric regions as a function of altitude. From the Australian Bureau of Meteorology: Space Weather (2016) Available Online: http://www.sws.bom.gov.au/Educational/5/2/2 [Accessed: 28 Jul. 2018]

Schunk and Nagy, 2009]. The primary positive ions in this region are O_2^+ and NO^+. The cluster ions that dominate the D region up to 85 km form through a process of hydration starting with these primary ions [*Schunk and Nagy*, 2009, *Wayne*, 1991]. Aside from composition, an important parameter for the behavior of ionospheric plasma is the ratio of collision frequency ν to cyclotron frequency Ω. Due to the very high neutral density in the D region, there are many collisions between charged particles and neutrals. Eventually, both electrons and ions follow the neutral gas motions and therefore they are considered 'collisional'.

1.4.2.2 E-Region

As illustrated in Fig. 1.3 the E region is located above the D region, and it extends from 90 km going up to 150 km altitude. The primary source of ionization for the E region is the EUV radiation coming from the Sun with wavelengths between 1 to 10 nm. The resulting primary ions due to ionization in this region are O^+ and N_2^+ which then turn into O_2^+ and NO^+[*Schunk and Nagy*, 2009]. The daytime plasma density in the E region usually varies between 10^{10} to 10^{11} electrons per m^3. In the E region, the neutral density is much less than in the D region and therefore the cyclotron frequency Ω_e exceeds the collision frequency ν_e. As a result of this, the electrons are 'magnetized' and therefore follow an $\mathbf{E} \times \mathbf{B}$ drift motion. The ions in the E region remain 'unmagnetized' below 120 km due to the fact that ions have heavier mass and therefore smaller cyclotron frequency Ω_i [*St.-Maurice and Hamza*, 2009].

The E region can be subdivided into two categories: 'normal' E and sporadic E layer. The normal E layer responds very similarly to the D region to energetic solar radiation and fluctuates daily and seasonally in similar fashion although its density is substantially larger.

As described in *Haldoupis* [2011], sporadic E layers (E_s) are related to an ionospheric phenomenon detected in the 1930's using ionograms. These layers are considered to be highly variable thin layers mostly between 90 and 120 km in altitude and usually have a high metallic content. They are typically produced by neutral wind shears which drive a convergence in the ionization. The E_s layers can be denser than the regular E layer, and may therefore affect radio-wave propagation in unpredictable ways according to Snell's law. Sporadic layers can occur at different times of day and during different seasons. The occurrence of E_s with high intensities has been observed between the months of June-July in the northern hemisphere, and in the southern hemisphere, they are observed

between December and January [*Haldoupis*, 2011]. At high latitudes electric fields have also been shown to be capable of driving Es layers [*Kirkwood and Von Zahn*, 1991].

1.4.2.3 F-Region

The F region extends from 150 km in altitude and upwards as shown in Fig. 1.3. The daytime plasma density in the F region usually goes up to 10^{12} electrons per m^3 during high solar activity. The Solar EUV radiation with a wavelength between 10 to 100 nm is the primary factor for ionization in the F region. The dominant ions below 200 km are O_2^+ and NO^+, and above 200 km the main ion is O^+. The F1 and F2 layers differ from each other due to different responses of molecular ions. The F1 layer is a daytime phenomenon, and it ranges from 150 to 250 km in altitude [*Schunk and Nagy*, 2009]. The free electron density in this region often reaches up to ten times more than the normal E region peak density. The F2 layer has the highest ionization peak of the ionosphere. The enhanced free electron density at these heights is due to a significant reduction in the recombination rate owing to a reduction in the production of molecular ions at the expanse of atomic ions, namely O^+ ions. Ironically the O^+ production rate actually goes down with altitude but the reaction that turns them into NO^+ ions actually goes down even faster with altitude. As a result the O^+ density keeps going up with altitude during the daytime, until diffusion takes over near 250 km at which point the density starts to go down with increasing altitude. At the point where that happens, the F2 peak is formed. The F region is also subject to seasonal variations and changes due to solar activity.

The ionospheric region above the F2 peak is called the topside ionosphere. It extends upward with decreasing density. At some point there is a transition where O^+ become less abundant than H^+ or He^+. The transitional height where this occur is observed approximately around 500 km at night or around 800 km during the day [*Endawoke*, 2018].

1.4.3 Radio Wave Propagation in the Ionosphere

In 1902, A.E. Kennelly and O. Heaviside came with independent postulations that a highly electrically conducting ionosphere exist which could explain the successful radio-wave transmission experiment by G. Marconi. However, the verification of the possible existence of the Ionosphere

came around 1925 when E.V. Appleton and M.A.F. Barnett established the existence and the altitude of the Kennelly-Heaviside layer [*Kivelson*, 1995]. A brief introduction to radio wave propagation is important because not all radio waves have straight propagation. This affects the character of the radar investigations of irregularities that can be done. Furthermore radio waves can be absorbed by the D region during things like proton events that introduce very large D region densities in the system [*Brower et al.*, 2009]. Finally, SuperDARN radars use radar waves that are refracted to study E and F region irregularities and it is important to know that they can also be absorbed if there is a strong D region. The reader should be forewarned that for this section the notation is different from the rest of this thesis.

If effects due to the geomagnetic field can be ignored, then during the propagation of a radio wave, if the radio frequency matches the plasma frequency of the medium (ω_p) the wave is reflected. If a radio wave of a particular frequency goes through the medium without matching the plasma frequency (ω_p), the wave is not reflected but it could still be refracted according to Snell's law [*Davies*, 1965] if the frequency is sufficiently close to the plasma frequency.

In a magnetized medium like that of the earth, things are more complicated than just stated, as there are other frequencies that affect the propagation. In this more general case, the radio wave propagation is described through the Appleton-Hartree equations which are now being discussed briefly here. We begin with the formula which describes the complex refractive index n as:

$$n^2 = 1 - \frac{X}{1 - iZ - \frac{Y_T^2}{2(1-X-iZ)} \pm \sqrt{\frac{Y_T^4}{4(1-X-iZ)^2} + Y_L^2}} \tag{1.16}$$

where $X = \omega_p^2/\omega^2$, and $\omega_p^2 = Ne^2/\epsilon_0 m$ is the square of the electron plasma frequency. Also, $Y_L = (\omega_c/\omega)B_L/B$ where ω_c is the electron cyclotron frequency, $\omega_c = eB/m_c$. Finally, $Y_T = (\omega_c/\omega)B_T/B$, and $Z = \nu/\omega$ where ν is the electron collision frequency. In the plasma frequency expression N is the electron number density, ϵ_0 is the permittivity of free space, m is the electron mass, and B is the magnetic field. The subscripts T and L refer to the transverse and longitudinal components of the electromagnetic wave, respectively [*Davies*, 1965].

The real part, μ, of the complex index of refraction is given by

$$\mu^2 = 1 - \frac{2X(1-X)}{2(1-X) - Y_T^2 \pm \sqrt{Y_T^4 + 4(1-X)^2 Y_L^2}} \tag{1.17}$$

To explain radio wave propagation in the D region,it is sufficient to consider that the collision frequency is so large that $Z >> X, Y_T$ and Y_L. The magnetic field then plays no role and the complex index of refraction is much simpler, as it is then given by the simplified expression

$$n^2 = (\mu - i\chi)^2 = 1 - \frac{X}{1 - iZ} = 1 - \frac{X}{1 + Z^2} - \frac{iXZ}{1 + Z^2} \tag{1.18}$$

If a traveling wave is considered to be a solution the amplitude decays by an amount $\omega\chi$ per unit distance. Defining this to be the absorption coefficient κ, we find

$$\kappa = \frac{e^2}{2\epsilon_0 m} \frac{1}{\mu} \frac{N\nu}{\omega^2 + \nu^2} \tag{1.19}$$

$$\kappa = \frac{\omega_p^2}{2\mu} \frac{\nu}{\omega^2 + \nu^2} \tag{1.20}$$

Eqn. 1.20 shows that the maximum absorption occurs when $\nu = \omega$. In case of absorption of radio waves in D region, μ as mentioned in Eqn. 1.20 is nearly equal to 1 and therefore in the D region when ω is much greater than ν, we have

$$\kappa \sim \frac{e^2}{2\epsilon_0 m} \frac{N\nu}{\omega^2} \tag{1.21}$$

$$\kappa \sim \frac{\omega_p^2 \nu}{2\omega^2} \tag{1.22}$$

Eqn. 1.22 helps us to understand the attenuation of radio waves in the D region while propagating through the D region [*Davies*, 1965]. It can be seen that the attenuation varies as the inverse of the frequency squared. Therefore, low frequency waves cannot propagate through the D region as easily as higher frequency waves that are not absorbed as much. On the other hand, if N is small, then there is little to no absorption, and the signals can pass through to reach higher altitudes.

1.5 Ionospheric Turbulence

Finally, note that although this thesis is about space plasma physics, it may prove useful to keep in mind the connection with fluids in general: whether it is a river or a space plasma, fast flowing regions are most of the time filled with small-scale structures, which are associated with turbulence. Turbulence is very important because it controls the way in which energy and momentum are exchanged within the fluid. This thesis deals with some aspects of ionospheric turbulence in relation to fast motions in the E region following the growth of large amplitude electrostatic waves associated with fast ionospheric plasma flows. These structures are known as 'Farley-Buneman' (FB) waves after the names of the scientists who first provided a physical explanation for their generation.

1.5.1 Instability

In the context of ionospheric physics, turbulence is related to the growth of structures through positive feedback mechanisms known as 'instabilities'. Usually, this positive feedback can generally be nicely described with plane waves at first. As long as the amplitude of the structures is small, the evolution of the structures is easy to understand and can be conveniently described in terms of plane waves through Fourier analysis. At that stage, the imaginary component of the frequency can immediately tell us if positive feedback is triggered or not [*Chen*, 1996]. However, this convenience comes with a price. When the amplitude of a structure has grown too much, individual Fourier components need to be described in terms of coupling between individual plane waves. In the fluid description, this is triggered by the rising importance of effects on the evolution of the waves that are associated with convective derivatives which introduce non-negligible non-linear terms in the equations [*St.-Maurice and Hamza*, 2001].

In spite of the above statements it should be noted that it is actually not necessary to describe the initial feedback mechanisms in terms of plane waves. For example, a FB structure can be described by a simple region of density enhancement ('blob' for short) which is elongated along the ambient electric field direction. The equations tell us that to first order all we have is advection of the blob. The connection with Fourier analysis is found by noticing that $\omega = \mathbf{k} \cdot \mathbf{V}$, where ω is

the frequency of the waves, **k** is the wavevector, and **V** is basically equal to the electrons $\mathbf{E}\times\mathbf{B}$ drift [*St.-Maurice and Hamza*, 2009]. In a blob description, we find an advection speed which is exactly the same as ω/k so that one can say that the electrons are 'pulling' the blob. The linear theory also states that the structures grow if their speed exceeds the 'ion-acoustic speed' of the plasma. The presence of the ion-acoustic speed is associated with ordinary diffusion. When the phase velocity of the structure exceeds the ion-acoustic speed of the medium, the positive feedback mechanism associated with the instability is able to overcome the decay due to diffusion. At that point in the description, the blob and wave approaches are completely similar and produce entirely equivalent results [*St.-Maurice and Hamza*, 2001].

However, once the amplitude of the structures grows, the phase velocity (or the velocity of the blobs) requires that we consider non-linear effects associated with the product of density and velocity perturbations. Here, a plane wave decomposition requires that all possible plane waves, including initially stable ones, be considered for interactions. And yet, when they reach their maximum amplitude, the observations of the structures reveal a very simple property, namely that the structures move at the ion-acoustic speed, namely, at speed associated with neither growth nor decay in the amplitude. The question to answer is then: how do we end up with the largest amplitude structures being structures that should not grow at all? The answer to that question is much easier to figure out if we use a blob approach as opposed to a Fourier decomposition. Mostly, this is because, with a blob approach, one can tell more easily how the structures evolve when the amplitude becomes large [*St.-Maurice and Hamza*, 2001]. The nonlinear description of the evolution of the structures using the 'blob' approach will, in fact, be the centerpiece of the present thesis.

While this thesis is theoretically focused, it is important to establish the motivation behind the calculations. It is too easy to state something along the lines that 'the maximum growth amplitude is at a zero growth rate' without showing some of the basis for that statement. To a large extent the statement is based on radar data, and also, it is obviously a bit too encompassing. In situ observations by a rocket, with on board instrumentation is also very useful for a clearer understanding of the structures. Radars observe one direction at a time and operate with only one particular wave-vector. Rockets cover a wide area in a short time and are not limited to a single wave-vector. However, rockets suffer from space-time ambiguities, which is not the case for radars.

Thus, there is important complementary information from the two observation platforms, and both deserve to be scrutinized prior to producing theoretical descriptions.

1.6 Radar Studies of Ionospheric Turbulence: a Canadian Context

Canada has always been in the thick of the action when it comes to radar observations of ionospheric turbulence. This had led to numerous experimental and theoretical studies from Canadian scientists. Most recently, the five Canadian SuperDARN radars have been recognized for their key contributions to the study of ionospheric motion in response to the solar wind impact on the earth plasma. It is therefore of interest to briefly review how radar science has evolved in Canada.

As described in some detail by *Moorcroft* [2006], the 'Radio Section' established within National Research Council (NRC) in 1931 marked the beginning of radio science in Canada. There were several key people who joined NRC around that time. The early success of NRC came with the development of a "Cathode-ray tube direction finder " to detect boats. The attempt to use the detection method by electrical means seeded the role of Canada in development of radar and related techniques. Between 1942 and 1945, approximately 2000 radars with five or six different frequencies were built and shipped out of Canada. In late 1950's, Canada was very much involved in studying observations using bi-static radars. The interesting results led to a series of studies using Continuous Waves (*CW*). This became a Canadian specialty later on. In 1958, the Institute of Space and Atmospheric Studies (ISAS) was established and eventually it became a center of studies to relate the solar activity to climate.

In the 1970's the BARS radar system was built as part of the ground-based CANOPUS array of instrumentation (the early precursor of Go Canada). BARS was a VHF radar, was used to obtain echoes from the E-region, to study electric field. However, not long thereafter, the scientists started to realize that the E-region echoes were not providing good electric field data when the field was large because of the saturation of the phase velocity at the ion-acoustic speed, which was becoming increasingly evident. At that point, a new concept based on HF radars, was developed by two French scientists, J P Vilain and C. Hanuise. At HF, the radar rays would be deflected by the ionosphere just

enough to hit perpendicularity to the geomagnetic field in the F region. Ionospheric irregularities are largely dominated by structures aligned with the magnetic field, so that HF radars would be able to get meaningful echoes from an altitude at lower E regions where the structures move at the plasma $\mathbf{E} \times \mathbf{B}$ drift. A first HF radar was built in Scandinavia. An extra bonus was a far greater field of view (FOV) than with the E-region radars. From this was born the concept of building pairs of HF radars looking at the same region from two different directions. These were called DARN for 'Dual Auroral Radar Network', where the network concept came from building several radar pairs. Once that proved to produce promising results, the larger SuperDARN network was developed on the notion that many DARN radar pairs could be used to produce global convection maps. Canada, under the leadership of George Sofko, was among the founders of SuperDARN with the USA and France under the leadership of Ray Greenwald and J P Vilain. The newly formed group first met in Saskatoon in 1993 on the occasion of the turn-on of the first Canadian SuperDARN radar. The Saskatoon radar is still under operation. As of January 2002, there were 15 radars in operation altogether, out of which 9 radars are in the northern hemisphere and rest 6 of them were in the southern hemisphere. The ISAS team is in charge of operating the Saskatoon, Prince George, Rankin Inlet, Inuvik and Clyde River radars. Over 35 radars are now included in the SuperDARN network, in which ten countries are involved [*McWilliams*, 2012].

Radar studies of ionospheric irregularities have not been limited to ground-based radars only. Most notably, a radar-linked project from space has been set up through the e-POP payload onboard the CASSIOPE satellite. The satellite is designed to help scientists to expand their knowledge and expertise in the near-Earth space environment, and some of the mission involves radio instruments receiving signals from the SuperDARN radars in order to study HF propagation and polarization. The e-POP mission is focused at enhancing the knowledge of the Space Weather processes by providing high resolution in-situ and remote probe based observations related to various observables, namely, particles, electromagnetic fields, and auroral activities [*Yau*, 2013].

One important point to clarify is that if we put enough power in a radar we can see structures that are perfectly stable and are simply in thermal equilibrium with the plasma. Such radars are called "Incoherent Scatter Radars". Most recently a pair of such radars was built in Resolute Bay, known as, 'Advanced Modular Incoherent Scatter Radars' (AMISR). The Resolute Bay Observatory was initially funded by the US government under National Science Foundation (NSF), and operated by

SRI International. The facility has become the operational hub to Resolute Bay Incoherent Scatter Radar-North (RISR-N) funded by NSF, and for the Canadian RISR-C (Canada) radar operated by the University of Calgary. The two radars point in opposite directions. The RISR-N pointing to the North whereas the RISR-C points to the South. The SuperDARN Clyde River radar was funded specifically to look over the central field of view of RISR-C. Together these radars cover a vast area in space and help in the measurements of various ionospheric parameters (such as as electron number density and plasma velocities). This information can help enhance our knowledge of the coupling between the space environment and the upper atmosphere in reaction to solar wind perturbations. RISR-C is funded by the Canadian Foundation for Innovation (CFI) [*Donovan*, 2014]. RISR-N is now ten years old while, due to unforeseen delays, the Canadian RISR-C is now only in its 3rd year of operation.

On a different note, while NASA launched the oceanography satellite Seasat, Canada launched the first civilian satellite with a synthetic aperture radar under the SurSat (Surveillance Satellite) program meant to produce radar imagery data. Based on this experience, planning began for RADARSAT. The small 'RADARSAT constellation' fleet is to follow soon (planned launch 2018) as the ultimate evolution of the RADARSAT program, with the objective to improve the use of synthetic aperture (SAR) with greater reliability [*Dettwiler*, 2017].

1.7 Thesis Outline

This thesis deals with ionospheric E region irregularities observed by radars, and to a lesser extent, rocket instrumentation. Thus, in Chapter 2, I present a few salient examples of some key rocket and radar observations of E region turbulent structures to set up the context for the theoretical study that will be central to this thesis. Chapter 3 then goes over linear and non-linear theories that provide a necessary context for my theoretical contribution. In Chapter 4, I study the various approaches taken by scientists to explain the growth and decay of the structures using various non-linear tools until finally, in Chapter 5, I present my own work and its implications for our understanding of E region irregularities.

Chapter 2

Selected observations of E region irregularities.

2.1 Introduction

Before going into observations, I introduce Fig. 2.1 (reproduced after *Rose et al.* [1992]) to summarize the context for the properties of the instabilities of interest to this thesis. The top part of the figure displays the parameters that may control the plasma instability and below are the resulting fluctuation properties. At HF in particular (decameter structures), the ambient electron density gradient may play a crucial role if the ambient electric field is not strong enough, namely, less than 40 mV/m [*St.-Maurice and Hamza*, 2009]. Given that the non-local effects discussed in chapter 4 limit the existence of the structures to a fraction of one second, a growth rate of the order of at least 10 s^{-1} is needed,meaning that weak electric fields by themselves will not produce a fast enough growth at 10 m. Importantly, the ambient magnetic field is crucial to the growth of the structures because it forces the electrons to be moving with the $\mathbf{E} \times \mathbf{B}$ drift while below 120 km, the ions move very slowly and in other directions [*St.-Maurice and Hamza*, 2009]. This establishes the Hall currents that are key to the instabilities of interest. The bottom part of Fig. 2.1 emphasizes that the structures are 'electrostatic', that is, that they are caused by charge accumulations from which electric fields are introduced.

For a better understanding of the processes taking place in the E-region ionosphere, observation techniques using rockets and radars have been adopted by researchers for years. The techniques employed to study the plasma fluctuations through radar and rocket are entirely different. As discussed in *Rose et al.* [1992], the radar is pointed towards plasma waves propagating along the wave vector $\mathbf{k}$ which interacts with a wave with phase velocity $\mathbf{V}_p$. Radars are often used in the

backscatter mode. Along the scattering direction, only irregularities with Fourier components equal to the half-wavelength of the radar in magnitude are detected. By contrast, it is difficult for rocket instruments to identify the direction of wave propagation. It is also difficult to understand the scale-length of the fluctuations in rocket data [*Rose et al.*, 1992]. However, unlike radars, the rocket observations are not limited to structures of a specific size or orientation so that they provide a 'broadband view' of the structures and their altitude variation. This complementarity of the observation techniques is good but it also means that care must be taken when comparing and extracting information from rocket and radar observations.

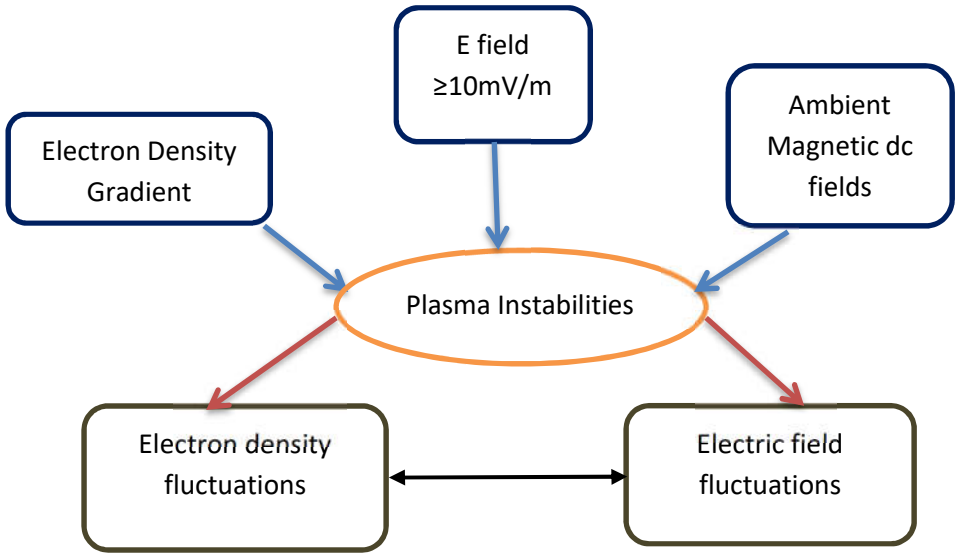

Figure 2.1: This diagram summarizes the context of plasma instabilities. The upper part shows the parameters that affect the instability, and the lower part displays the resulting fluctuations that can be observed with rockets or radars. From *Rose et al.* [1992]

2.2 Rocket Observations

In this section, I discuss rocket observations through a brief overview of the experiments and observations carried out during the "Rocket and Scatter Experiments"(ROSE) campaign. During this campaign in 1991, four rockets were launched. Two were launched from Kiruna (Sweden) and the other two from Andoya, Norway. With the rocket experiments on ROSE, both electron density and electric field fluctuations were measured in-situ during plasma unstable conditions, along with

the d.c. electric field [*Rose et al.*, 1992]. The most important quantity that helps understand the origin and maybe the evolution of the instabilities is the background electric field. For Farley-Buneman(FB) waves to be unstable (the focus of the present work), the perpendicular electric field component with respect to the background magnetic field should exceed 20 mV/m (e.g. *Fejer and Kelley* [1980]). Smaller electric fields can still create the instability through the gradient-drift mechanism. This happens when the electric field is found to have a component along the density gradient. The electric field was measured via two methods during the ROSE campaign, namely, with an onboard floating double probe system [*Rinnert*, 1992] and though incoherent scatter radar (ISR) observations of the plasma drift [*Kohl et al.*, 1992].

The neutral atmosphere also plays a critical role in the triggering of the instabilities. The neutral density influences the ion motion through collisions of the ions with the neutral molecules. While the effect is less important, the electron-neutral collision frequency also plays a role: as shown for example in *St-Maurice and Schlegel* [1983] and references therein, both collision frequencies appear in the dispersion relation of instabilities through the relative drift between ions and electrons. This in turn affects the instability growth rate and the altitude over which the plasma is found to be unstable. To measure the neutral density, an instrument was included in the payload in-situ during the campaign program [*Friker and Lübken*, 1992, *Rose et al.*, 1992].

The mass of an ion is also an important quantity in the dispersion relation through the role played by the ion-acoustic speed $C_s = \sqrt{(k(T_e + T_i)/m_i)}$ (k is the Boltzmann Constant, Te is the electron temperature and Ti is the ion temperature). This parameter is key to understanding the behavior of the instability [*Robinson and Honary*, 1990, *Rose et al.*, 1992]. To see if any metallic ions were present beyond NO^+ and O_2^+, an ion mass spectrometer was therefore included in the payload [*Rose et al.*, 1992, *SteinWeg et al.*, 1992].

To have an understanding of the background electron density gradient which is very crucial in studies related to the gradient-drift instability, some resonant probes were included into the payloads to study and understand the background electron density [*Rose et al.*, 1992]. Measurements of the d.c. magnetic field are also important for the study of the plasma instabilities since the radar backscatter depends on the magnetic aspect angle. Therefore, it was important to determine accurately the magnetic field direction and a magnetic field model (IGRF 85) was used to estimate it [*Rose et al.*, 1992]. To study if there was any magnetic perturbation a magnetometer was included

on the rocket payload, in the process giving additional information about the magnetic field and its variation through a determination of the currents and their altitude structure [*Lühr*, 1992].

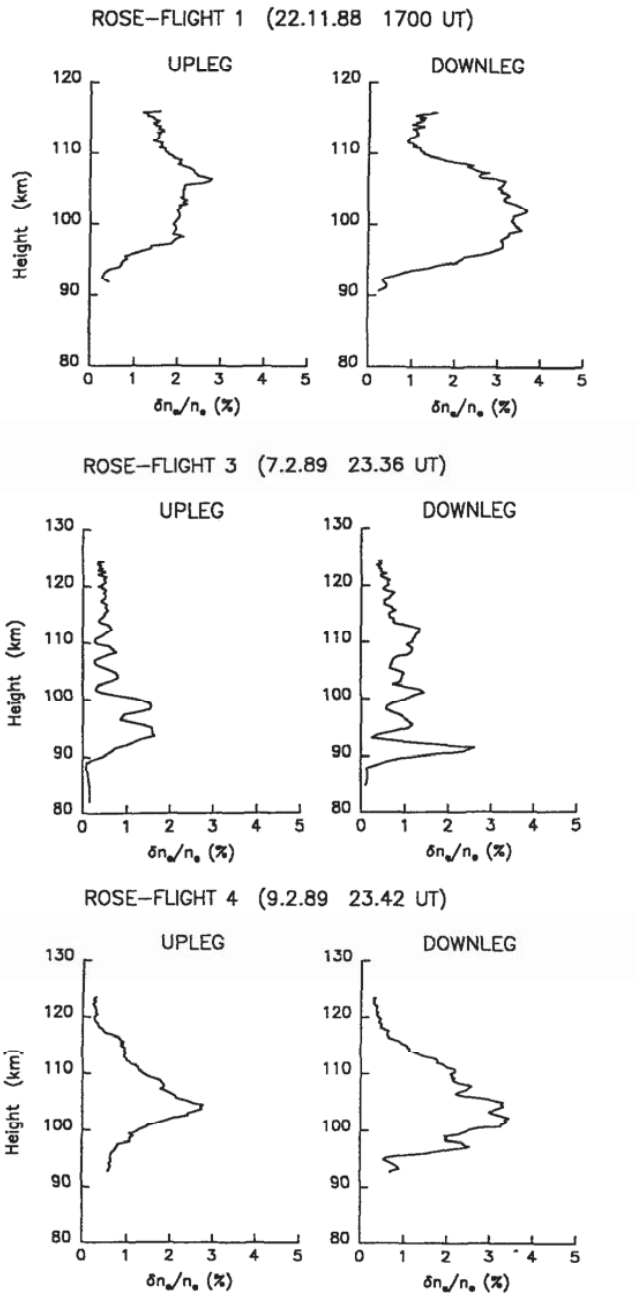

Figure 2.2: Broadband relative density fluctuations within the frequency range 30-1000 Hz for both upleg and downleg during the ROSE campaign flights. The results from F1,F3 and F4 are shown here [*Schlegel*, 1992].

In Fig. 2.2, the broadband relative density fluctuations $\overline{\Delta n_e/n_e}$ are reproduced from the ROSE

campaign. As discussed in *Schlegel* [1992], the results are shown after the densities were measured over the frequency range of 30-1000 Hz. The lower limit of integration was chosen to avoid bias which happens in the lower frequencies through the spinning and possible slight wobbling of the rocket. The density plots reveal the height range over which the related instability in the E region was excited. For the F1 flight (upper panel) this range covered the altitudes between 95 and 110 km. The upper boundary during F4 (lower panel) was above 110 km as can be seen clearly in the Fig. 2.2. Interestingly, the observed ambient electric field was stronger on that occasion. The profile during the F3 flight as shown in the figure, did not show a distinct maximum as the observed electric field was rather weak. No fluctuations were observed during the F2 flight [*Schlegel*, 1992]. The density fluctuations observed during the ROSE campaign were similar to the results published by many other authors earlier on this issue. In particular, the height profiles and the values of $\overline{\Delta n_e/n_e}$ generally less than 10 percent have been obtained by several researchers prior to the ROSE campaign [*Kelley and Mozer*, 1973, *Ogawa et al.*, 1976, *Pfaff et al.*, 1984] as mentioned in *Schlegel* [1992]. In fact, similar results related to the average density fluctuations have been reported during the equatorial electrojet events which are also subject to d.c. electric fields strong enough to destabilize the E region plasma [*Pfaff et al.*, 1987a,b, *Prakash et al.*, 1972].

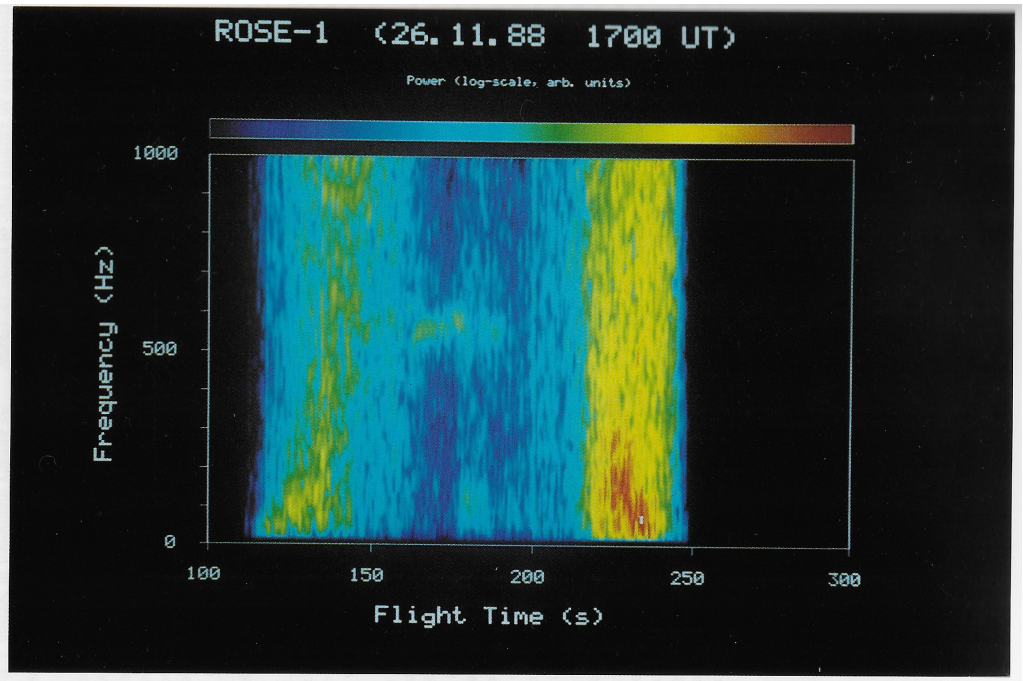

Figure 2.3: A measurement of electron density fluctuation power vs frequency and flight time for the F1 flight during the Rose campaign through a false color plot is shown [*Schlegel*, 1992].

In Fig. 2.3, a false color plot of fluctuation intensities vs frequency and time is shown for the F1 flight. It is composed of a spectrum in the frequency range of 10-1000 Hz. Two bands can be seen in which E region irregularities are visible, one during the upleg and the other during the down leg [*Schlegel*, 1992]. The strongest fluctuations in F1 occur while the frequencies are close to 200 Hz and near an altitude of 101 km during the upleg and about the same height during the down leg [*Schlegel*, 1992]. This feature has been observed separately in the past *Pfaff et al.* [1984, 1987a,b] and has been attributed to a tendency for lower frequency waves to be excited at lower altitudes than the higher frequency waves. The proposed explanation has been that the electron density gradient is large near the bottom side thereby creating favorable conditions for the gradient-drift instability, making this contribution particularly visible under moderate electric field conditions [*Schlegel*, 1992].

In another comprehensive E-region campaign called ERRRIS for 'E-region Rocket Radar Instability Study', one of the parameters under investigation was the full electric field, namely the ambient part in combination with that of the short scale two-stream waves. The primary focus of this simultaneous rocket and radar was to study the same medium through both techniques. As

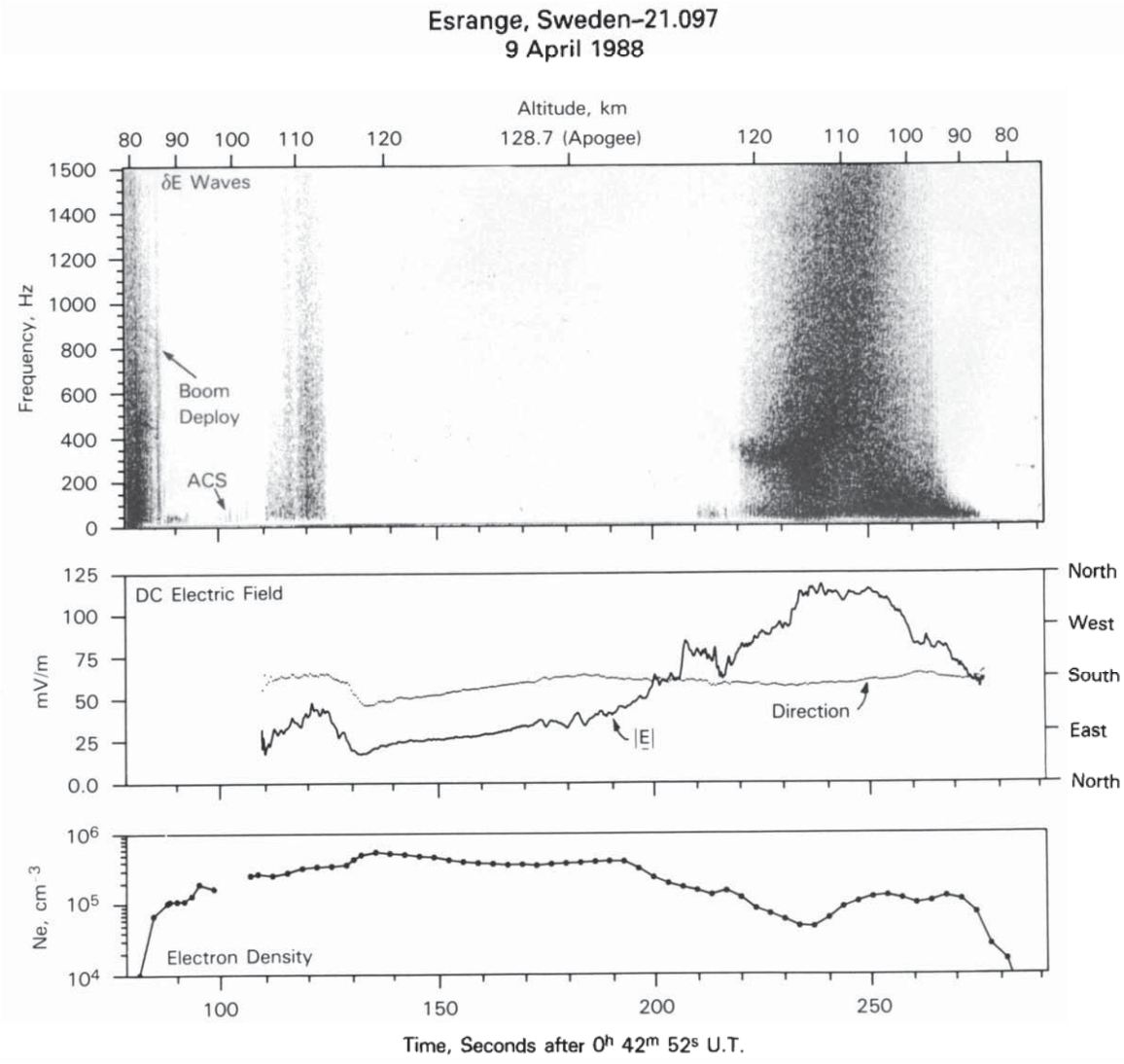

Figure 2.4: In-situ measurements of electric field and density taken during rocket flight (21.097) in the ERRRIS campaign. The top panel shows a frequency spectrum of 0-1600 Hz for the electric field. The simultaneous d.c. electric field observation is shown in the middle panel, and the plasma density observed with the Langmuir probe is shown in the lowest panel. From *Pfaff* [1991].

mentioned in *Pfaff et al.* [1992], each rocket during this campaign was fitted with electric field probes to measure the background electric field and the wave electric field. In Fig. 2.4 a narrow broadband fluctuation between 104 and 114 km depicts a slightly unstable electrojet during upleg and the same instrument during the down leg, identified a very strong, broader layer of waves ranging between 90 and 122 km, indicating a region of unstable electrojet [*Pfaff et al.*, 1992]. The unstable region was far more turbulent on the down-leg where the ambient d.c. electric field was much stronger than on the upleg. As shown in the second panel of Fig. 2.4, the peak electric field observed during the upleg was around 40 mV/m and while it was more than 100 mV/m on the downleg. This large d.c. electric field acts as a driver for the Farley-Buneman waves and its turbulence. This was therefore confirmed by the in-situ probes. It was also concluded that the strong d.c. electric fields impact the observed extent of the altitude region where the instability occurs [*Pfaff et al.*, 1992]. During the two-stream electrojet conditions the d.c. electric field was very strong and as a result the large amplitudes high frequency (short wavelength) waves were created near the top of the unstable layer, where two-stream oscillations are expected to be driven.

Based on the examples shown here and many similar observations, we can summarize the state of in-situ rocket observations as follows: both the density and electric field fluctuations increase in amplitude as the strength of the ambient electric field increases. The broadband density fluctuation level is usually less than 7 or 8% and is seen to increase with the ambient electric field strength. While the turbulence is found at the expected altitudes, its altitude range increases with the strength of the ambient electric field, mostly by extending to higher altitudes. We should add that the strong linkage between the density and electric field fluctuations indicates that the waves are electrostatic. Finally, lower frequency waves tend to dominate the spectrum near the bottom of the unstable region near 100 km altitude.

2.3 Radar Observations

The ionospheric region has been extensively studied using radars with operating frequencies of 10 MHz and greater. The transmitting frequency of the radar is usually well above the maximum plasma frequency of the ionosphere, and therefore most of the signals are lost into space [*Fejer and Kelley*, 1980]. Whether ionized or not, the atmosphere contains irregularities of many sizes.

When radio waves penetrate a given atmospheric region, a small fraction of the incident energy is scattered in various directions. For monostatic radars, the signals scattered by ionospheric irregularities spaced by half a wavelength are reinforced for a direction pointing back towards the radar and add up to a signal that may or may not be strong enough to be detected through Bragg scattering [*Hargreaves*, 1992].

Even a completely quiet ionosphere that's in full thermal equilibrium has density fluctuations. While the intensity of these structures is very small, it is measurable with powerful enough radars, namely, the so-called Incoherent Scatter Radars (ISRs). For this stable situation, the spectrum of the radio waves scattered from a given location is so well-known that it can be used to extract the plasma density from the total scattered power while the spectral shape itself provides information on the electron and ion temperatures and the plasma drift. A radar selects the spatial component at half the wavelength of the incident radio wave. Note that for the thermal equilibrium waves sampled by ISRs, the shape of the spectrum reveals that low frequency oscillations associated with ion-acoustic oscillations decay in a few oscillations. Since the amplitude of these ion-acoustic waves is very small near thermal equilibrium, it takes a tremendous amount of power to get an echo from the stable plasma [*Hargreaves*, 1992].

When there are large departures from thermal equilibrium, the ionospheric plasma often becomes turbulent, and the amplitude of the fluctuations increases by several orders of magnitude. The requirement for the power used by radars then goes down enormously (from MW pulses down to a few kW). These lower power radars are simply called 'coherent' radars. Two types of coherent radars are used for irregularity studies, namely, monostatic (pulsed) and bistatic (continuous and pulsed). Bistatic radars have their transmitting and receiving antennas at different sites, while the monostatic radars use the same antenna for transmitting and receiving [*Fejer and Kelley*, 1980].

Incoherent and coherent scatter radars both Fourier analyze the medium and observe how the plasma structures change as a function of time and space. Incoherent scatter radars look at a wave spectrum that can be handled analytically because these waves are stable. They 'only' require linear (but kinetic) theory based on production from thermal agitation. Usually, the distribution function is considered to have a Maxwellian (Gaussian) shape [*Sahr and Fejer*, 1996]. From this, a complete spectral shape calculation can be undertaken. Namely, starting from initial Maxwellian conditions for the excitation function, a Laplace transform can be taken, and a spectrum can be computed.

As stated above, ion-acoustics waves dominate the spectrum at low frequencies even though they typically decay in 2 to 3 oscillations when the electron and ion temperatures are comparable.

While coherent radars look at much larger amplitude structures and are therefore far cheaper and easier to operate, it proves difficult to extract much information from the spectrum aside from the Doppler shift. In the F region, this still proves to be very useful as the frame of reference of the waves is the plasma $\mathbf{E}\times\mathbf{B}$ drift (both ions and electrons move at the same velocity). In the E region, ions and electrons do not move at the same speed, and the Doppler shift of the waves presents a challenge, as will be discussed in future chapters in this thesis. There is also one feature that is common to most ionospheric turbulent situations in that the structures are strongly aligned with the magnetic field, owing to the high electron mobility along the magnetic field lines, which tends to wipe out parallel electric fields over short distances. In other words, and as illustrated through Fig. 2.5 taken from *Sahr and Fejer* [1996], turbulent structures, be they ion-acoustic waves or otherwise, are only observable by coherent radars if observing perpendicular to the geomagnetic field. Put in another way, if the alignment of the radars is even as small as 2° away from perpendicularity nothing is normally observed by coherent radars [*Sahr and Fejer*, 1996]. Beyond 5° away from perpendicularity to the magnetic field the spectrum comes from thermal noise at all angles, meaning that large amplitude waves can normally only be seen from structures that are perpendicular to the magnetic field.

2.3.1 What do Coherent Radars Observe in the E Region?

- The volume cross-section of backscatter from the ionosphere is determined by the mean square electron density fluctuations $< \Delta N^2 >$, and the normalized spatial power spectrum, f($\mathbf{k}$) of the density fluctuations [*Farley et al.*, 1981].

- From the wave momentum Eqn. [*Fejer and Kelley*, 1980], $\mathbf{k}_t = \mathbf{k}_w + \mathbf{k}_s$, where t,w and s stands for transmitted, plasma waves and scattered signals. In case of backscatter $\mathbf{k}_s = -\mathbf{k}_t$, and therefore, $k_w = 2k_t$. In that case, the wavelength of the electron density fluctuations (the plasma waves) probed by the radar, has to be equal to half the radar wavelength.

- Beyond 100 km altitude, the neutral atmosphere is very thin. Therefore, it cannot scatter detectable amounts of radio wave energy. The coherent echoes observed from VHF radars

from 100 km or above must be the result of Bragg-like scatter from large-scale irregularities (plasma density with significant amplitude). This emphasizes the existence of meter-scale irregularities in [*Sahr and Fejer*, 1996].

- The observed Doppler shifts are proportional to the radar operating frequency [*Greenwald and Ecklund*, 1975]. In the E region as well as in SuperDARN data in general the spectra are usually presented in Doppler velocity units $\Delta\omega/\Delta k$ instead of actual frequencies in Herz. Here $\Delta\omega$ is the difference between the incident and scattered frequency while $\Delta k = 2k_t$ is the scattered wavenumber. The average frequency in terms of a mean phase velocity usually lies in the range from 0 to 500 m/s. [*Sahr and Fejer*, 1996].

- Many modern radar experiments usually provide the power spectrum of the scatter, not just the scattered power and mean Doppler velocity. A classification of “types" has been adopted which characterizes the first and second moments (mean Doppler and Doppler width) of the spectra. Examples of several power spectra are shown in Fig. 2.6. A classification template has been developed by *Sahr and Fejer* [1996] and others before them for a determination of echo “type", as shown in Fig. 2.6 and Fig. 2.7.

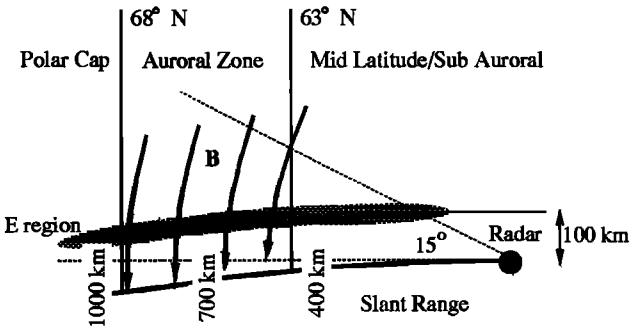

Figure 2.5: Typical coherent scatter radar geometry for northern high latitude backscatter. The radio waves encounter the irregularities while propagating nearly perpendicular ($\sim \pm 2°$) to the magnetic field. From *Sahr and Fejer* [1996]

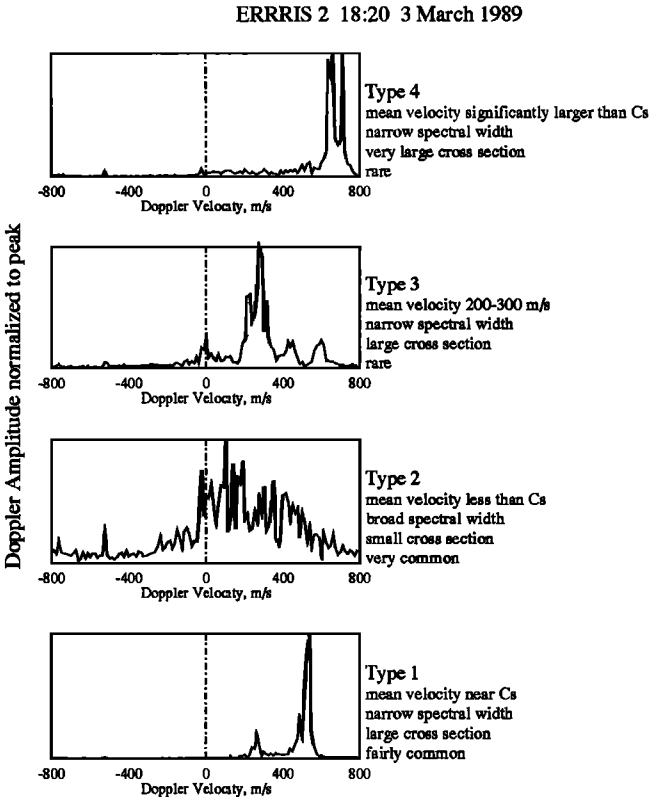

Figure 2.6: Examples of four different echo types. The most common nomenclature of four "types" based on mean Doppler velocity and the spectral width has been listed here. The data were drawn from a 50 MHz radar (CUPRI) as part of the ERRRIS experiment described by *Pfaff* [1991] and published in *Sahr and Fejer* [1996].

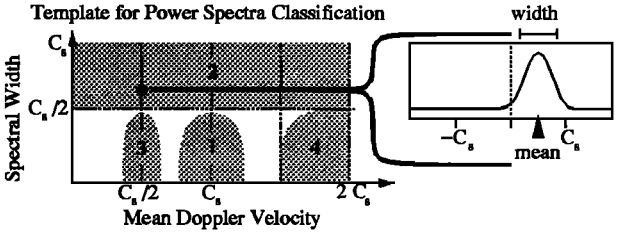

Figure 2.7: Template for determining electrojet echo "type" based upon the Doppler width and the mean Doppler velocity. From[*Sahr and Fejer*, 1996]

2.3.2 Spectral Characteristics

Fig. 2.8 provides a summary by *Moorcroft* [2002] based on his study of the E region spectral spectral properties seen by various radars during auroral events. The ion acoustic speed, C_s, is an

important marker while seeking to identify electrostatic plasma waves to categorize radar auroral echoes [*Moorcroft*, 2002]. Fig. 2.8 (panels a, b and c) shows the observed relationship between spectral width and mean phase speed. The relative-drift between electrons and ions in the auroral E-region, $\mathbf{V}_d$, is nearly equal to the $\mathbf{E} \times \mathbf{B}$ drift at 110 km and below. This $\mathbf{E} \times \mathbf{B}$ drift of electrons ($\mathbf{V}_d$) is the source of free energy which in turn plays a crucial role in creating the plasma irregularities in the E region. As a result of this, $\mathbf{V}_d$ and the angle it makes with $\mathbf{k}$ (the so called 'flow angle') are very important quantities to help us to study and identify various echo types. Echoes can be classified mainly in two categories, firstly those with a more or less constant phase velocity (V_p) and secondly those which are approximately proportional to $\mathbf{k} \cdot \mathbf{V}_d$ (velocity along the radar line of sight). Most of this behavior is represented in Fig. 2.8 (panels d,e and f), which shows the relationship with the phase speed and the component of the $\mathbf{V}_d$ [*Moorcroft*, 2002].

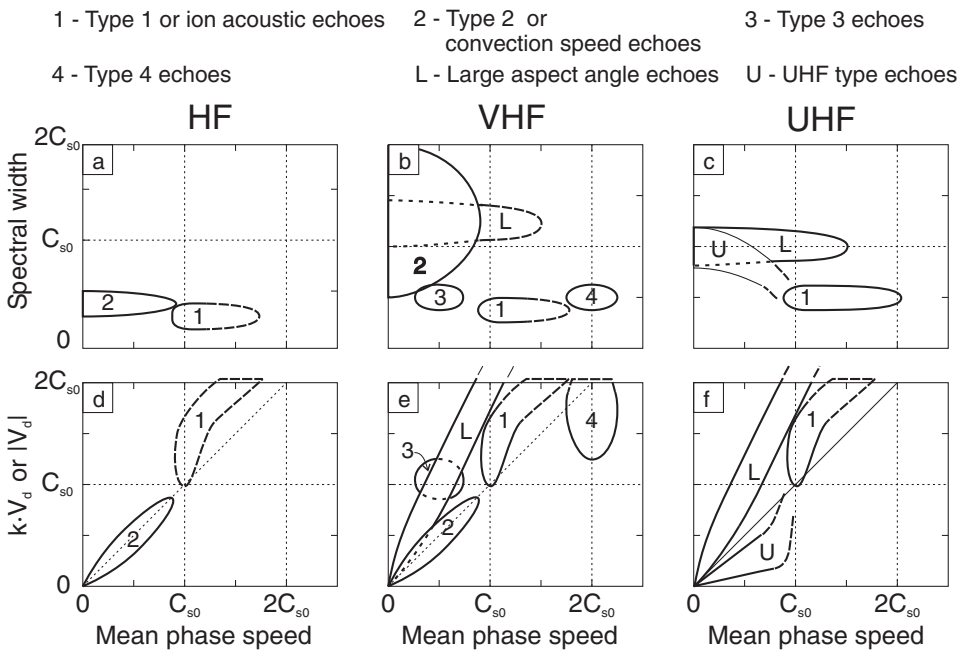

Figure 2.8: This figure shows a schematic of observations related to radar aurora for four major echo types as shown in this figure. Relationship between $\delta\omega$ and mean phase speed along with the relationship between $\mathbf{k} \cdot \mathbf{V}_d$ and mean phase speed is shown. From *Moorcroft* [2002]

Different echo types have been discussed based on the spectral width and Doppler velocity [*Kustov et al.*, 1995]. Type 1 echoes usually have narrow spectra and they move with speeds close

to C_s. From the bottom panels of Fig. 2.8, looking into $\mathbf{V}_d$ one can infer that the phase velocities increase due to increased electron temperature. Still, this clashes with the FB instability theory which predicts that the most unstable waves should go at a velocity that is very close to the $\mathbf{E} \times \mathbf{B}$ drift [*Buneman*, 1963, *Farley*, 1963] while the waves going at the ion-acoustic speed show have by contrast no growth at all and waves with slower phase speeds should not exist at all. The implication is that as the amplitude of the waves grow their phase speed decreases until a maximum amplitude is reached when the growth rate is zero, namely, when the structures do move at the ion-acoustic speed. After that, the waves decay by transfering their energy to stable modes or through some other non-linear processes that feeds the electrons by heating them. One way or the other it has become clear that when they reach their maximum amplitude, the growth rate of the waves has become zero [*Moorcroft*, 2002, *St.-Maurice and Hamza*, 2009]. It is in fact possible that if the mechanism responsible for slowing the structures down continues to operate, then their amplitude will start to decrease. This would explain why the spectral width oF type 1 structures is normally far from being very narrow. This is, in fact, a central point that will be used in the present thesis.

As mentioned in *Cohen and Bowles* [1967], type 2 echoes were initially detected and studied in the equatorial electrojet using VHF radars and later on, in the auroral region [*Balsley and Ecklund*, 1972]. These echoes usually have very broad spectra and their mean Doppler speeds is much less than C_s. According to *Kofman and Nielsen* [1990], the phase speed would be nearly equal to the line-of-sight component of $\mathbf{V}_d$ if that component is itself less than C_s. A way to understand type 2 waves is to consider the evolution of a plane wave that turns into a highly elongated structure with its wave vector perpendicular to the long axis. As explained in *St.-Maurice and Hamza* [2001], the structures evolve edges along the elongated direction. These produce Fourier components along the direction perpendicular to the growth direction. Consequently, the plane wave breaks into intermittent substructures. As only diffusion operates in the elongated direction (no destabilizing factor along the ambient electric field direction) the structures decay with a spectral width which is close to the ion-acoustic speed of the medium in velocity units.

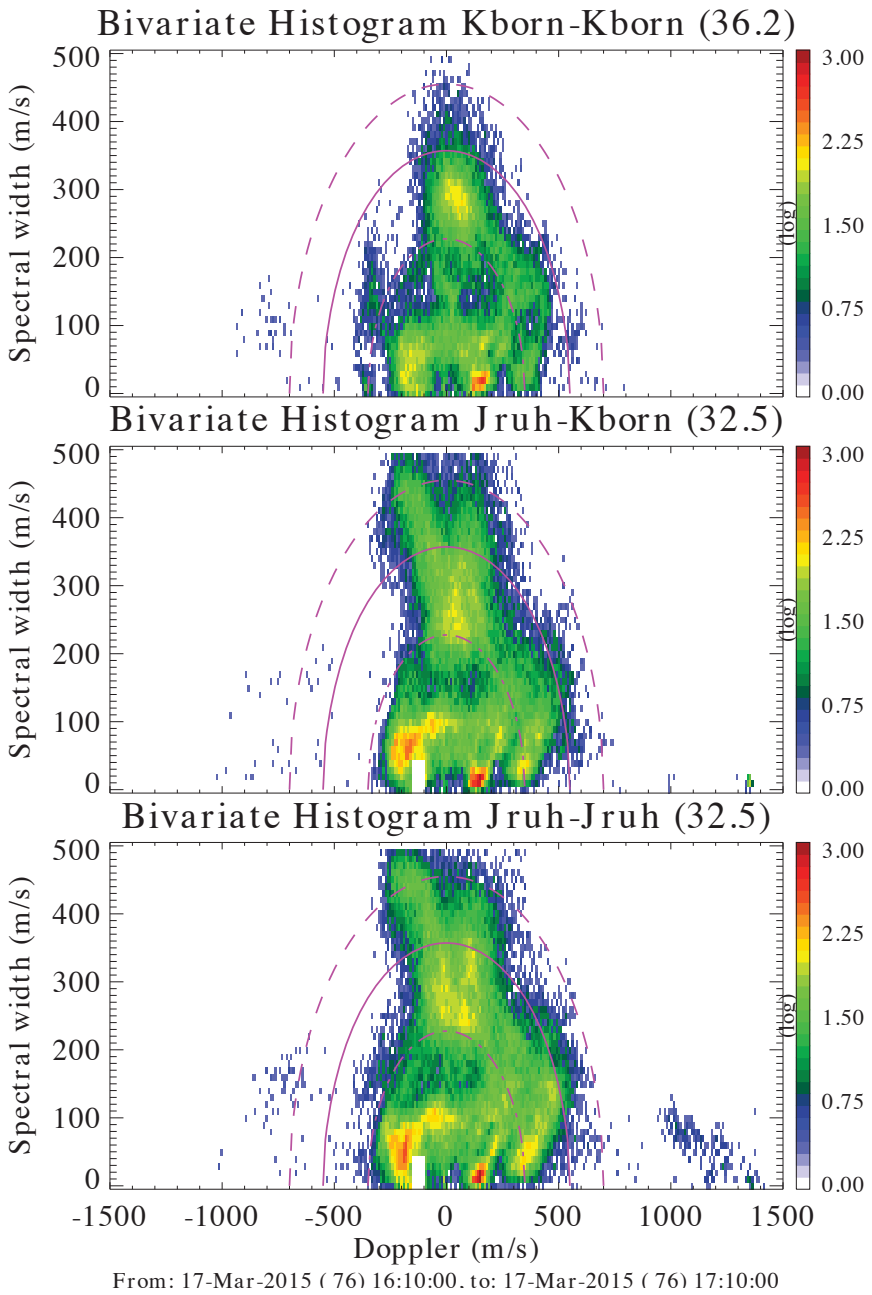

Figure 2.9: Results from observations made in Northern Germany at 32.5 and 36 MHz during the strong magnetic storm of March 17, 2015. The 2-D histograms display all four types of E region echoes from the type 2 population (wide and slow) to type 1 (Doppler shifts at the ion -acoustic speed with spectral widths less than 100 m/s in velocity units) to type 3 (Doppler width less than 50 m/s with Doppler shifts of the order of 100 m/s) to type 4 (granular echoes with very small spectral width and Dopper shifts in excess of 1000 m/s). The red traces are meant to illustrate the connection between type 1 and 2 waves. From [*Chau and St.-Maurice*, 2016].

Type 3 echoes usually have narrow spectra with Doppler velocities between (150 – 200) m/s and can be observed with spectral widths as small as 30 m/s. As shown in Fig. 2.9, they can either be positively or negatively Doppler shifted with both spectra sometimes observed simultaneously. Type 3 echoes can be observed approximately between 90 and 100 km altitude [*Chau and St.-Maurice*, 2016]. These authors also found that the slow, narrow echoes evolve from very narrow to somewhat wider together with a slight increase in their Doppler speed and an increase in their altitude.

As also shown in Fig. 2.9 type 4 echoes have narrow spectra, but their speed is of the order of the magnitude of the $\mathbf{E} \times \mathbf{B}$ drift, that is of the order of 2 C_s or more rather than C_s for type 1 waves. Type 4 echoes have so far been hard to isolate, although interferometry seems to position them at higher altitudes of the unstable region. They tend to be weaker than type 1 waves and be positioned in their vicinity [*Chau and St.-Maurice*, 2016]. Most such echoes were observed using VHF radars [*Fejer et al.*, 1986]. Many explanations have been proposed for these waves. *Providakes et al.* [1988] have suggested that they were due to hot electrons although they could not reach the observed velocities and their theory could not explain the very narrow spectral widths. Another suggestion has been that these echoes were produced when a high electric field excited the waves in unfavorable conditions in a way where the splitting of the ion-acoustic waves is observed, leading to slow and fast components at least at HF [*St.-Maurice et al.*, 1994a]. Most recently, *Chau and St.-Maurice* [2016] proposed instead that type 4 simply come from the top of the unstable region, where the growth rates are small (hence the narrow spectra) while the Doppler shift came from the sum of the ion drift and threshold speed, whichis nearly equal to the electron $\mathbf{E} \times \mathbf{B}$ drift. The waves would also be easier to detect in relation to precipitation events producing ionization near 120 km altitude (requires keV electrons). As seen through the bottom panel of Fig. 2.9, for the event that they analyzed *Chau and St.-Maurice* [2016] found that the type 4 Doppler velocities varied between 1200 and 1400 m/s with a spectral width less than 80 m/s.

2.3.3 Discussion of Radar Aurora at Different Frequencies

We now return to Fig. 2.8 with a comparison of observations at different frequencies, and discuss a number of interesting issues mentioned in *Moorcroft* [2002]. In Fig. 2.8, the first row shows different echo types.

- *Ion-acoustic echoes at HF:* Ion-acoustic echoes are generated by the FB instability if the Doppler velocity is close to C_s. However, at HF, the threshold phase velocity changes remarkably while the ambient density gradients are present [*Fejer and Farley*, 1975, *St.-Maurice et al.*, 1994b]. This stated, on the basis of the intermittency theory presented by *St.-Maurice and Hamza* [2001, 2009] the impact of the density gradients would depend on the strength of the electric field.

- *Spectral widths observed through HF and VHF:* Spectral shapes observed through HF, VHF, and UHF radars are similar and are not related to the differences in the spectral width [*Moorcroft*, 2002]. In addition, *Eglitis et al.* [1995] suggested that the spectra observed at HF would usually have a Lorentzian-shape while spectra seen through the VHF and UHF radars would usually be more Gaussian-like.

- *Broad spectra at VHF:* The type 2 echoes that are observed using VHF radars are usually broader in shape than any other echoes in different frequency ranges. What is it about the size associated with VHF wavelengths that leads to such echoes with so broad in shape while comparing with the higher or lower frequency ranges? Given that the spectral width should increase with turbulence through a shorter lifetime of individual irregularities, this would indicate a stronger turbulence level for structures of the order of 1 m in size [*Moorcroft*, 2002]. Most of the type 2 observations at high latitudes were done at large aspect angles *Watermann et al.* [1989]. It may well be that the structures decay more quickly once they have achieved a larger aspect angle. Caution is therefore indicated in view of the fact that only very few small aspect angle studies related to type 2 spectra are available at high latitudes, as indicated in *Moorcroft* [2002]. By comparison, there are far more extensive studies of the spectral width that have been made at the equator so that a comparison between the two regions would be desirable.

- *Echoes at UHF:* At both HF and VHF, there are many examples of mean Doppler shifts in type 2 echoes for which $\mathbf{V}_{ph} \simeq \alpha \mathbf{k} \cdot \mathbf{V}_d$ ($\alpha > 1$ for UHF echoes). However, at UHF, no echoes have this property. In fact, echoes moving at a lower phase velocity rapidly show an increase in their phase velocity until it is close to C_s. Beyond that, the Doppler shift appears to remain essentially constant [*Moorcroft*, 2002].

2.4 What to bring home from the observations

It is quite evident that the E-region irregularities occur frequently all over the globe. They are particularly common at high latitudes and at the equator. They are observed by in-situ rocket-measurements and also seen through radar echoes with frequencies varying from HF at 8 MHz to UHF at more than 1 GHz. The rocket flights have verified the electrostatic characteristics of the irregularities. This was confirmed while observing simultaneous events related to strong density and the electric field fluctuations with no indication of significant magnetic fluctuations [*St.-Maurice and Hamza*, 2009].

The majority of the E region irregularities are triggered by Hall currents. This situation arises below 120 km where the ion collision frequency becomes larger than the ion cyclotron frequency. As a result, the ions tend to follow the neutrals increasingly closely with decreasing altitude, whereas the electrons remain strongly magnetized above 80 km. When an electric field is applied in a direction perpendicular to the geomagnetic field, the $\mathbf{E} \times \mathbf{B}$ drifting electrons carry the Hall currents. These Hall currents in turn become the source of free energy in the E region [*St.-Maurice and Hamza*, 2009]. The Hall currents and their association with electrons in the E region indicate that one should focus on two basic theories related to the formation of irregularities at high latitudes, namely, Farley-Buneman at higher wave-number and the gradient-drift instability at lower wave-numbers. The rocket data support the notion that the FB instability plays a stronger role in the top part of the unstable region, while the gradient-drift instability, with its lower frequencies, seems to be more prevalent in the lower parts of the unstable region. A central point of the radar data that has emerged over the years is that for the most part (with due exceptions) the phase velocity of the FB structures at their maximum amplitude is the phase velocity associated with zero growth rate conditions. From that point of view, type II structures have to be decaying structures, since they are seen in directions closer to the ambient electric field direction and are moving at speeds slower than the speed required for a structure to be growing. From a Fourier description, such structures would have to be produced through mode-coupling, namely, by taking energy away from growing modes and transferring it into decaying modes. In this thesis, a different but basically physically equivalent description will be used for the decay, which in turn should help improve the understanding of the physics at play in the nonlinear evolution of the structures.

Chapter 3

Linear Theory

3.1 Linear Fluid Theory

In this chapter, the linear treatment of the Farley-Buneman (FB) instability is revisited in order to develop a clear view of the treatment of the problem. After going over the fluid treatment of the FB instability, the additional effects of the Gradient-Drift (GD) instability will be introduced, followed by an introduction to the kinetic theory treatment.

Even fluid theories can become complicated if ions and electrons cannot be considered to be isothermal. The more complicated electron non-isothermal treatment proves to be useful particularly near the bottom of the unstable layer [*Dimant and Sudan*, 1997, *Kissack et al.*, 1995] while the nonisothermal ion treatment is useful near the top of the layer [*Dimant and Oppenheim*, 2004]. Here, I intend to focus on the basic physics behind the instability and therefore only present the simple isothermal fluid theory treatment. Through this I provide the reader with a few basic concepts to help understand the physical picture involved. In the process I introduce a few terms like convective speed and anti-diffusion and discuss the growth and decay of a structure in those terms. I do not rush to provide a Fourier analysis of the problem so as to emphasize the parallel between plane waves and the evolution of finite size elongated structures.

As shown below, the waves or their elongated structure counterparts propagate through the medium with the electron $\mathbf{E} \times \mathbf{B}$ drift and ion-inertia is responsible for the growth of the Farley-Buneman instability. The first theoretical models describing this Farley-Buneman instability were developed separately by *Farley* [1963] using a kinetic theory and *Buneman* [1963] using a fluid theory. Note that the derivation of the gradient-drift instability is very similar although, the growth arises through the transport of higher density plasma into a lower density background (and

vice-versa) without the need for ion inertia to be a factor [*Rogister and d'Angelo*, 1970].

3.1.1 Electron and Ion Motion:

First of all, we need to study the motion of electrons and ions in the background plasma in the plane perpendicular to **B** in the presence of an electric field. The pressure gradient force matters, but only to second order. The effects due to gravity can be neglected. Therefore, to leading order, the steady state ion and electron equations of motion become

$$0 = n_i e(\mathbf{E}_0 + \mathbf{V}_i \times \mathbf{B}) - \rho_i \nu_i(\mathbf{V}_i - \mathbf{V}_n) \tag{3.1}$$

$$0 = n_e e(\mathbf{E}_0 + \mathbf{V}_e \times \mathbf{B}) - \rho_e \nu_e(\mathbf{V}_e - \mathbf{V}_n) \tag{3.2}$$

where n_j is the number density of species j (ion or electron),$\mathbf{V}_j$ is the velocity of the species (ions, electrons and the neutrals), $\rho_j = n_j m_j$ (the mass density) and ν_j is the momentum transfer collision frequency with the neutrals and $\mathbf{E}_0$ is the ambient (background) electric field. We also assume that $\mathbf{E}_0 \perp \mathbf{B}$ and derive the following set of equations for ions and repeat the same process for electrons. However, the approximations are considered while discussing the ratio of various collision frequencies. For the ions

$$\frac{\nu_i}{\Omega_i}(\mathbf{V}_i - \mathbf{V}_n) = \frac{\mathbf{E}_0}{B} + \frac{\mathbf{V}_i \times \mathbf{B}}{B} \tag{3.3}$$

This is rewritten as

$$\frac{\nu_i}{\Omega_i}\mathbf{V}_{in} = \frac{\mathbf{E}}{B} + \frac{\mathbf{V}_{in} \times \mathbf{B}}{B} \tag{3.4}$$

where $\Omega_i = \frac{eB}{m_i}$ is the ion-cyclotron frequency, $\mathbf{V}_{in} = \mathbf{V}_i - \mathbf{V}_n$ is the relative ion-neutral speed and $\mathbf{E} = \mathbf{E}_0 + \mathbf{V}_n \times \mathbf{B}$ is the electric field in the frame of reference of the neutral gas.

From Eqn. 3.4 we also obtain

$$\frac{\mathbf{V}_{in} \times \mathbf{B}}{B} = \frac{\Omega_i}{\nu_i}\frac{\mathbf{E} \times \mathbf{B}}{B^2} - \frac{\Omega_i}{\nu_i}\mathbf{V}_{in} \tag{3.5}$$

Eqn. 3.3 can now be solved elegantly by calculating the cross-product with **B** which gives the

following:

$$\frac{\nu_i^2}{\Omega_i^2}\mathbf{V}_{in} = \frac{\nu_i}{\Omega_i}\frac{\mathbf{E}}{B} + \frac{\mathbf{E}\times\mathbf{B}}{B^2} - \mathbf{V}_{in} \tag{3.6}$$

After multiplying Eqn.3.6 with $\mathbf{B}/B$ Ω_i/ν_i and then substituting Eqn. 3.6 back in Eqn. 3.4 to obtain:

$$\mathbf{V}_i = \mathbf{V}_n + \frac{\nu_i/\Omega_i}{1+\nu_i^2/\Omega_i^2}\frac{\mathbf{E}}{B} + \frac{1}{1+\nu_i^2/\Omega_i^2}\frac{\mathbf{E}\times\mathbf{B}}{B^2} \tag{3.7}$$

This shows that the net ion velocity $\mathbf{V}_i$ has contributions from background the neutral velocity $\mathbf{V}_n$ along with the velocity contributions due to Pedersen (along the $\mathbf{E}$ direction) and Hall drifts (along the $\mathbf{E}\times\mathbf{B}$ direction). Repeating these steps for the electrons with $\Omega_e = \frac{eB}{m_e}$ for the electron-cyclotron frequency and ν_e being the electron collision frequency, we get

$$\mathbf{V}_e = \mathbf{V}_n - \frac{\nu_e/\Omega_e}{1+\nu_e^2/\Omega_e^2}\frac{\mathbf{E}}{B} + \frac{1}{1+\nu_e^2/\Omega_e^2}\frac{\mathbf{E}\times\mathbf{B}}{B^2} \tag{3.8}$$

Looking into Eqn. 3.7 and Eqn. 3.8 one can say that the ratios Ω_i/ν_i and ν_e/Ω_e play an important role. In the E region, below 120 km the ratio of Ω_i/ν_i is small. However, in the same region, the electrons almost $\mathbf{E}\times\mathbf{B}$ drift since ν_e/Ω_e is small. As a result we can to first order write the electron and ion velocities as

$$\mathbf{V}_e \approx \mathbf{V}_n - \frac{\nu_e}{\Omega_e}\frac{\mathbf{E}}{B} + \frac{\mathbf{E}\times\mathbf{B}}{B^2} \tag{3.9}$$

$$\mathbf{V}_i \approx \mathbf{V}_n + \frac{\Omega_i}{\nu_i}\frac{\mathbf{E}}{B} \tag{3.10}$$

From Eqn. 3.9 and since $\nu_e/\Omega_e << 1$ above 90 km, one can say that at the E region heights the electrons are strongly magnetized. Similarly, from Eqn. 3.10 it can be seen that the ions have a tendency to follow the neutrals along with also a small (but not entirely negligible) Pedersen drift along the electric field direction.

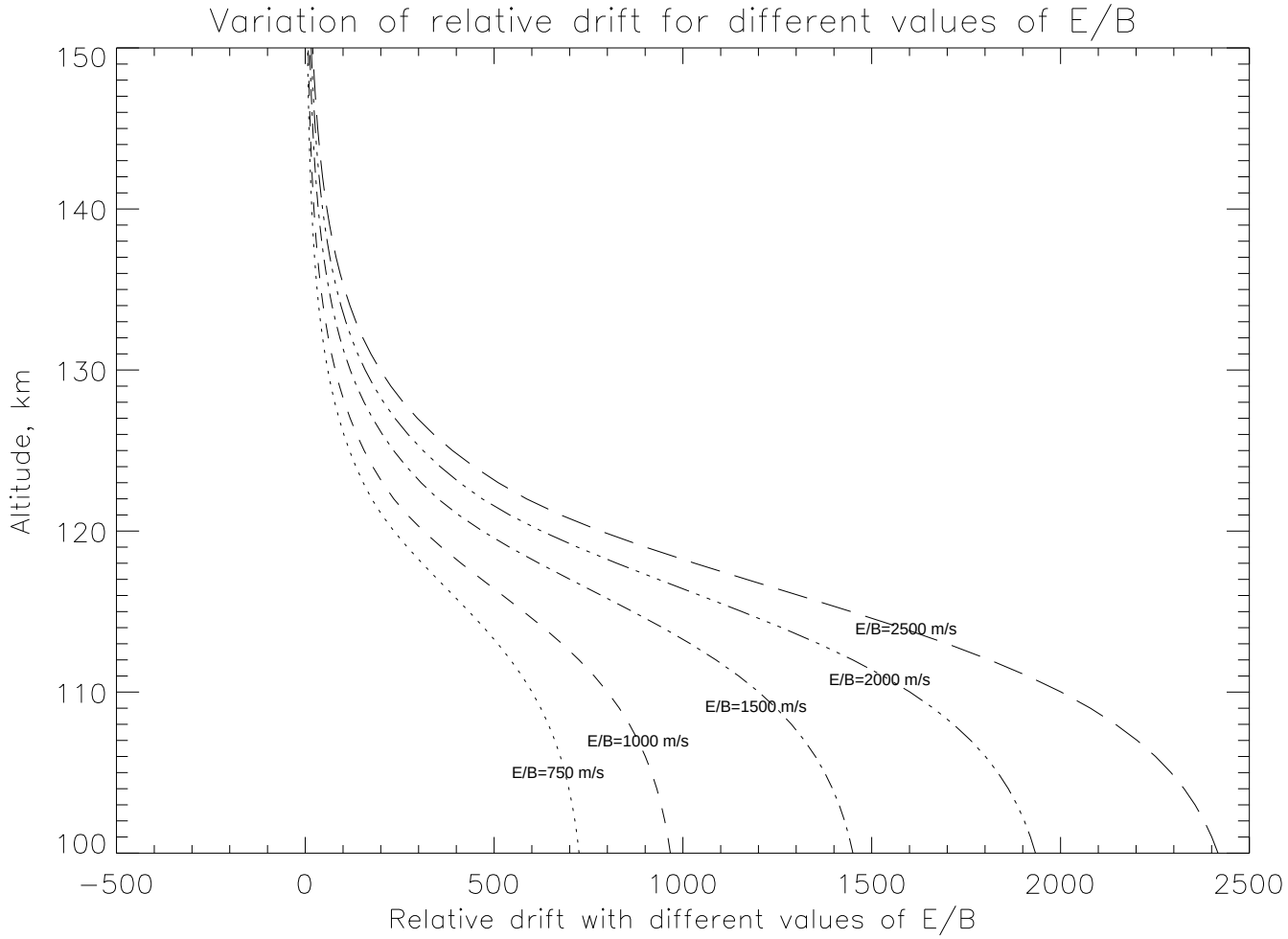

Figure 3.1: Altitude variations of $|V_e - V_i|$ for different values of E_0/B. MSIS 90E model neutral densities parameters have been used to plot this profile together with collision frequencies presented in *Schunk and Nagy* [2009].

As shown in Fig. 3.1 the difference between the electron and the ion velocities is significant in the E region at altitudes below 120 km. Of course the value of E_0/B is key in producing these differences. More details about the features presented here can be found in *Baumjohann and Treumann* [2012], *Drexler* [2005], *Kelley* [2009].

3.1.2 Farley-Buneman Instability Theory

The standard treatment of Farley-Buneman instability theory would start with a Fourier analysis of the momentum and continuity in time and space. This treatment can be found for instance in the

book by *Kelley* [2009].

Here, I follow an alternative description proposed by *St.-Maurice and Hamza* [2001] where all time and space dependent parameters are kept instead. Two very different time scales are identified for the problem at hand. The fast time scale involves the description of the motion of a “blob” or “hole”. The slow time scale involves diffusion and ion-inertia which introduces the computation of a growth rate.

3.1.2.1 Fast time-scale description

The description of fast time scales is based on the setup of a polarization electric field in blob or holes. I want to explain the motion of the structures involved through Fig. 3.2 which is based on a diagram initially made by Josef Drexler [*Drexler*, 2005]. Suppose there is a local enhancement (“blob") or a depletion (“hole") with an arbitrary shape $\delta n/n_0$. Note that for this model to line up with the plane wave analysis normally used to describe the structures, the variations in y have to be much slower than in the x-direction. A function $f(x, y)$ could describe a density enhancement or depletion. For the instability mechanism to work, we assume that the structure must be elongated along y (i.e., along the $\mathbf{E}_0$ direction). As a result of the elongated geometry, the initial perturbation has to propagate in the direction of the electron drift. This has to do with the fact that, since the electrons are magnetized, they are $\mathbf{E} \times \mathbf{B}$ drifting while the ions stay behind because they are collisional. This elongated geometry creates an electric field perturbation $\delta\mathbf{E}$, which accelerates the background ions (as opposed to the ions in the density perturbation) [*Drexler*, 2005]. At first, the electron motion produces a negative charge on the edge of the blob as shown in Fig. 3.2.

The electrons carry a perturbed current as shown below:

$$\delta\mathbf{J}_e = -e\left[\delta n_e\left(\frac{\mathbf{E}_0 \times \mathbf{b}}{B}\right) - n_0\frac{\delta\mathbf{E}}{B}\frac{\nu_e}{\Omega_e} + n_0\frac{\delta\mathbf{E}\times\mathbf{B}}{B}\right] \tag{3.11}$$

It is important to note that in Eqn. 3.11 there is no $\mathbf{V}_n$ because the system is solved in the neutral frame of reference. The first term in this equation comes from the current due to perturbed electron density $\mathbf{E}_0 \times \mathbf{B}$ drift. The second term is the result of the currents carried by the background electrons.

For the ions, the perturbed current is from the background ions reacting to the $\delta\mathbf{E}$ polarization

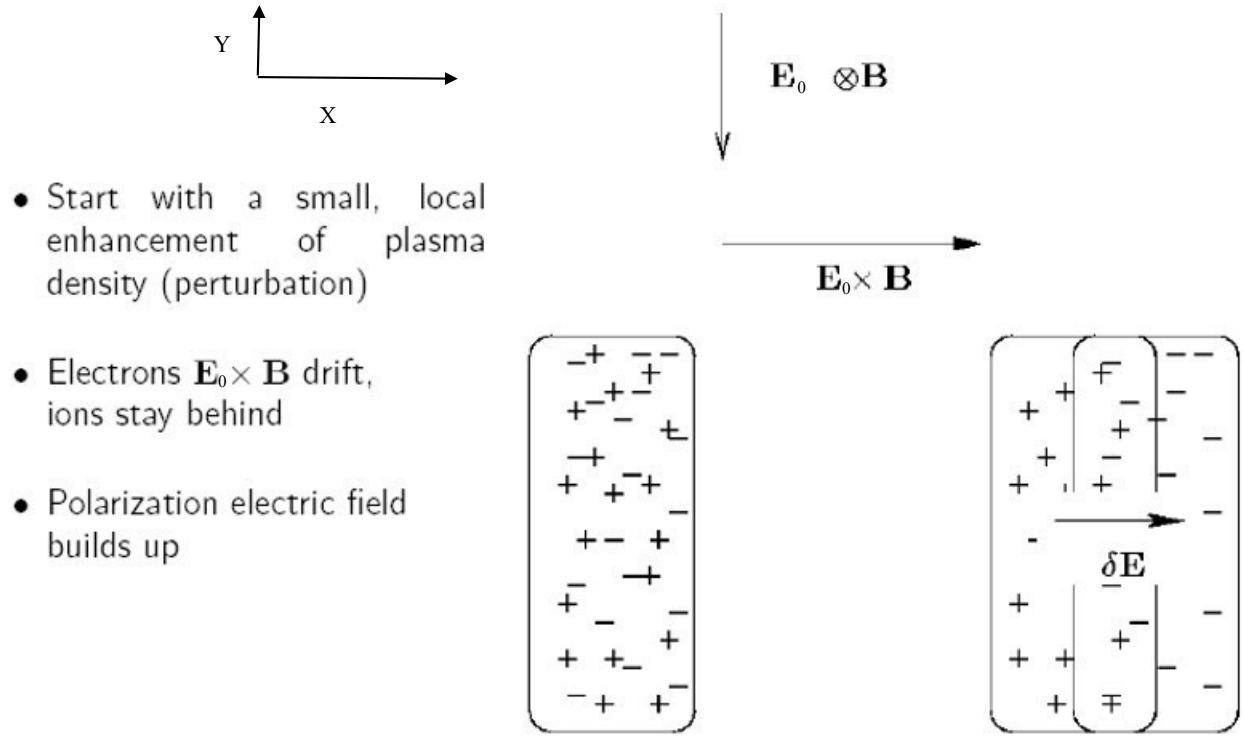

Figure 3.2: Diagram of a plasma density enhancement traveling in the $\mathbf{E}_0\times\mathbf{B}$ drift direction, illustrating the processes that provide propagation of field-aligned irregularities. The panel to the left shows the density enhancement δn over the background density n_0. The panel on the right-hand side shows the charge separation and the perturbed electric field $\delta\mathbf{E}$ in the blob produced by the electron $\mathbf{E}_0 \times \mathbf{B}$ drift (along +X direction). The electric field $\mathbf{E}_0$ is along the -Y direction. Based on a diagram by *Drexler* [2005]

field. This means that from Eqn. 3.10 we get:

$$\delta \mathbf{J}_i = e n_0 \frac{\Omega_i}{\nu_i} \frac{\delta \mathbf{E}}{B} \tag{3.12}$$

The $\delta\mathbf{E}$ field is a polarization field in the $\mathbf{E}_0 \times \mathbf{B}$ direction that comes from balancing the perturbed electron Hall currents with the perturbed ion Pedersen currents. Note that as a result of the presence of this $\delta\mathbf{E}$ another polarization field in the $\delta\mathbf{E} \times \mathbf{B}$ direction will be set up and so on. This double polarization effect is part and parcel on the nonlinear theory presented in Chapter 5. Here we focus on the linear theory and do not take double polarization effects into account.

Thus, very soon after a perturbed electron current is setup through their $\mathbf{E}_0 \times \mathbf{B}$ drift, the polarization electric field builds up until the background ions acquire a Pedersen current such that there is no current in the $\mathbf{E}_0 \times \mathbf{B}$ direction. This meanns that the polarization electric field inside the structure is such as to cancel the Perturbed Hall currents with perturbed Pedersen currents. In other words we end up with

$$\delta \mathbf{J} = \delta \mathbf{J}_i + \delta \mathbf{J}_e = 0 \tag{3.13}$$

meaning that we end up with

$$n_0 \frac{\Omega_i}{\nu_i} \frac{\delta \mathbf{E}}{B} + n_0 \frac{\nu_e}{\Omega_e} \frac{\delta \mathbf{E}}{B} = \delta n_e \frac{\mathbf{E}_0 \times \mathbf{b}}{B} + n_0 \frac{\delta \mathbf{E} \times \mathbf{B}}{B} \tag{3.14}$$

In the linear theory the last term on the right-hand-side is thrown away, being considered as a nonlinear correction that only produces 'anomalous fluxes' along an infinitely long structure (i.e., a plane wave). With the last term out and with $\delta\mathbf{E}$ and $\mathbf{E}_0 \times \mathbf{b}$ being in the same x-direction, we end up with

$$\frac{\delta E}{B} = \frac{\delta n}{n_0} \frac{\nu_i}{\Omega_i} \frac{E_0/B}{1 + \Psi_0} \tag{3.15}$$

where $\Psi_0 = \nu_e \nu_i / \Omega_e \Omega_i$.

We now return to the perturbed electron continuity equation with the assumption that $n_e = n_i$ and find

$$\frac{\partial}{\partial t} \delta n + \frac{\delta}{\delta x} \left[n_0 \delta V_e + \frac{E_0}{B} \delta n \right] = 0 \tag{3.16}$$

with n_0 as constant. This becomes:

$$\frac{\partial}{\partial t}\left(\frac{\delta n}{n_0}\right) + \frac{\delta}{\delta x}\left[- \frac{\nu_e}{\Omega_e}\frac{\delta E}{B} + \frac{E_0}{B}\frac{\delta n}{n_0}\right] = 0 \tag{3.17}$$

Using Eqn. 3.15 for the relation between δE and δn and end up with

$$\frac{\partial}{\partial t}\left(\frac{\delta n}{n_0}\right) + \frac{E_0/B}{1+\Psi_0}\frac{\partial}{\partial x}\left(\frac{\delta n}{n_0}\right) = 0 \tag{3.18}$$

In the more general derivation $V_d = |\mathbf{V}_e - \mathbf{V}_i|$ would replace E_0/B. This will be discussed in chapter 5.

3.1.2.2 Longer time scales

Longer time scales involve the effects of ion inertia and ambipolar diffusion. For these, we must consider the ion momentum equation first.

$$\frac{\partial \delta \mathbf{V}_i}{\partial t} - \frac{e\delta \mathbf{E}}{m_i} = -\nu_i \delta \mathbf{V}_i - \frac{\nabla p_i}{n_0 m_i} \tag{3.19}$$

Recalling that $\Omega_i = eB/m_i$ and $p_i = nk_BT_i$ (where k_B is the Boltzmann constant) and T_i being constant for the isothermal situations, we get:

$$\frac{\partial \delta \mathbf{V}_i}{\partial t} - \frac{\delta \mathbf{E}}{B}\Omega_i = -\nu_i \delta \mathbf{V}_i - C_i^2 \nabla \frac{\delta n}{n_0} \tag{3.20}$$

where $C_i = \sqrt{k_B T_i/m_i}$ is the ion-sound speed of the plasma. Once we take the divergence of Eqn. 3.20, we get

$$\nabla \cdot \left[\frac{\partial \delta \mathbf{V}_i}{\partial t} + \nu_i \delta \mathbf{V}_i\right] = \Omega_i \nabla \cdot \frac{\delta \mathbf{E}}{B} - C_i^2 \nabla^2 \frac{\delta n}{n_0} \tag{3.21}$$

and from the perturbed ion continuity equation we have, $\partial \delta n/\partial t = -n_0 \nabla \cdot \delta \mathbf{V}_i$. Therefore if we substitute this result in Eqn. 3.21 we have the following:

$$-\frac{\partial^2}{\partial t^2}\frac{\delta n}{n_0} - \nu_i \frac{\partial}{\partial t}\frac{\delta n}{n_0} = \Omega_i \nabla \cdot \frac{\delta \mathbf{E}}{B} - C_i^2 \nabla^2 \frac{\delta n}{n_0} \tag{3.22}$$

We can find an expression for perturbed electric field $\delta\mathbf{E}$ though a study of the electron equations. Strting with the electron continuity equation and assuming charge neutrality, we have:

$$\frac{\partial}{\partial t}\delta n = -\mathbf{V}_e \cdot \nabla\delta n - n_0 \nabla \cdot \delta\mathbf{V}_e \tag{3.23}$$

Now turning our attention to the perturbed electron momentum equation and if we define Ω_e as positive, we have

$$\delta\mathbf{V}_e = -\frac{\nu_e}{\Omega_e}\frac{\delta\mathbf{E}}{B} - \frac{\nu_e}{\Omega_e^2}\frac{\nabla p_e}{n_0 m_e} + \frac{\delta\mathbf{E}\times\mathbf{B}}{B^2} + \frac{(\nabla\delta p)\times\mathbf{B}}{n_0 e B^2} \tag{3.24}$$

If we take the divergence of Eqn. 3.24 and substitute in Eqn. 3.23, we find that since $\nabla\cdot(\delta\mathbf{E}\times\mathbf{B}) = 0$ for an electrostatic perturbation, the divergence of the last term is always zero

$$\nabla\cdot\frac{\delta\mathbf{E}}{B} = -\frac{\Omega_e}{\nu_e}\Big[\frac{\partial}{\partial t} + \mathbf{V}_e\cdot\nabla\Big]\frac{\delta n}{n_0} + \frac{1}{\Omega_e}C_e^2\nabla^2\frac{\delta n}{n_0} \tag{3.25}$$

where $C_e^2 = k_B T_e/m_e$. Eqn. 3.25 can be combined with Eqn. 3.22 to give us:

$$-\frac{\psi_0}{\nu_i}\frac{\partial^2}{\partial t^2}\frac{\delta n}{n_0} = (1+\psi_0)\frac{\partial}{\partial t}\frac{\delta n}{n_0} + V_e\cdot\nabla\frac{\delta n}{n_0} - \frac{\psi_0}{\nu_i}C_s^2\nabla^2\frac{\delta n}{n_0} \tag{3.26}$$

where $C_s^2 = (\Omega_i/\Omega_e)C_e^2 + C_i^2 = [k(T_e+T_i)]/m_i$ is the square of ion-acoustic speed of the plasma. After re-arranging the terms we finally get

$$\Big[\frac{\partial}{\partial t} + \frac{\mathbf{V}_e}{1+\psi_0}\cdot\nabla\Big]\frac{\delta n}{n_0} = -\frac{\psi_0}{\nu_i(1+\psi_0)}\Big[\frac{\partial^2}{\partial t^2}\frac{\delta n}{n_0} - C_s^2\nabla^2\frac{\delta n}{n_0}\Big] \tag{3.27}$$

A similar, though more general, derivation that is free of Fourier analysis can be found in *Drexler* [2005]. An important point about this derivation is that it was not derived with Fourier analysis as is often the case. However, we can replace $\partial/\partial t$ by $i\omega$ and ∇ by $-i\mathbf{k}$ to immediately recover the standard dispersion relation expression.

3.1.3 Introduction of parallel electric fields

While the previous subsection provides the most basic physics, the waves/structures can (and do) evolve electric field perturbations along the magnetic field direction. This affects the growth rate of

the structures. In fact, if the parallel electric field is too large, the structures cannot grow. Only very small perturbations in the parallel electric fields can be allowed if there is to be growth. Another way to put it is that the perturbations must be strongly aligned with the magnetic field, which is in fact observed since, as mentioned in Chapter 2, radar echoes are typically observed with aspect angles less than 2°.

In this section here, I introduced $\delta\mathbf{E}_{\parallel}$ to show the important modifications it introduces into the instability. I use Fourier analysis in the direction parallel to the magnetic field to keep the derivation simple. A more general derivation that does not use Fourier analysis along any direction including the parallel direction can be found in *Drexler* [2005].

We assume that because of their much lighter mass, we only need to consider to response of the electrons to the parallel electric field of the structures. From the electron momentum balance along the parallel direction we then get

$$\delta\mathbf{V}_{e\parallel} = \frac{-e\delta\mathbf{E}_{\parallel}}{m_e\nu_e} - \frac{1}{\nu_e}\frac{\nabla_{\parallel}p_e}{n_0 m_e} \tag{3.28}$$

$$\delta\mathbf{V}_{e\parallel} = -\frac{\Omega_e}{\nu_e}\frac{\delta\mathbf{E}_{\parallel}}{B} - \frac{1}{\nu_e}\frac{\nabla_{\parallel}p_e}{n_0 m_e} \tag{3.29}$$

Taking next $\nabla\cdot\delta\mathbf{V}_{e\parallel}$ we obtain,

$$\nabla\cdot\delta\mathbf{V}_{e\parallel} = -\frac{\Omega_e}{\nu_e}\frac{\nabla\cdot\delta\mathbf{E}_{\parallel}}{B} - \frac{1}{\nu_e}\frac{\nabla_{\parallel}^2 p_e}{n_0 m_e} \tag{3.30}$$

In similarity with the derivation without a parallel electric field we also have

$$\delta\mathbf{V}_{e\perp} = \frac{\nu_e}{\Omega_e}\Big[-\frac{\delta\mathbf{E}_{\perp}}{B} - \frac{\nabla_{\perp}p}{n_0 m_e}\Big] - \frac{\delta\mathbf{E}\times\mathbf{B}}{B^2} - \frac{(\nabla\delta p)\times\mathbf{B}}{B^2 n_0 e} \tag{3.31}$$

Now taking divergence of eqn. 3.31 we get,

$$\nabla\cdot\delta\mathbf{V}_{e\perp} = \frac{\nu_e}{\Omega_e}\Big[-\frac{\nabla_{\perp}\cdot\delta\mathbf{E}_{\perp}}{B} - \frac{\nabla_{\perp}^2 p}{n_0 m_e}\Big] \tag{3.32}$$

$$\nabla\cdot\delta\mathbf{V}_{e\perp} = \frac{\nu_e}{\Omega_e}\Big[-\frac{\nabla_{\perp}\cdot\delta\mathbf{E}_{\perp}}{B} - C_e^2{\nabla_{\perp}}^2\frac{\delta n}{n_0}\Big] \tag{3.33}$$

Similarly, from eqn. 3.30,

$$\nabla \cdot \delta \mathbf{V}_{e\parallel} = -\frac{\Omega_e}{\nu_e}\frac{\nabla_\parallel \cdot \delta \mathbf{E}_\parallel}{B} - \frac{1}{\nu_e} C_e^2 {\nabla_\parallel}^2 \frac{\delta n}{n_0} \tag{3.34}$$

Before adding eqn.3.33 and eqn.3.34, we put the parallel components in terms of perpendicular components and therefore we have,

$$\frac{\nabla_\parallel^2 \cdot \delta \mathbf{E}_\parallel}{B} = \frac{k_\parallel^2}{k_\perp^2}\frac{\nabla_\perp \cdot \delta \mathbf{E}_\perp}{B} \tag{3.35}$$

$$\nabla_\parallel^2 \frac{\delta n}{n_0} = \frac{k_\parallel^2}{k_\perp^2}\nabla_\perp^2 \frac{\delta n}{n_0} \tag{3.36}$$

Now adding eqn.3.33 and eqn.3.34 using values from eqn.3.36, we get

$$\nabla_\perp \cdot \delta \mathbf{V}_{e\perp} + \nabla_\parallel \cdot \delta \mathbf{V}_{e\parallel} = \Big(-\frac{\nu_e}{\Omega_e}\frac{\nabla_\perp \cdot \delta \mathbf{E}_\perp}{B} - \frac{\nu_e}{\Omega_e \Omega_i}\frac{k_B T_e}{m_i}\nabla_\perp^2 \frac{\delta n}{n_0}\Big)\Big(1 + \frac{{\Omega_e}^2}{{\nu_e}^2}\frac{k_\parallel^2}{k_\perp^2}\Big) \tag{3.37}$$

Define Ψ as,

$$\Psi = \Psi_0\Big(1 + \frac{\Omega_e^2}{\nu_e^2}\frac{k_\parallel^2}{k_\perp^2}\Big) \tag{3.38}$$

with $\Psi_0 = \frac{\nu_e \nu_i}{\Omega_e \Omega_i}$ as before. We can now rewrite eqn.3.37 using eqn. 3.38 to obtain,

$$\nabla \cdot \delta \mathbf{V}_e = \Psi\Big(-\frac{\Omega_i}{\nu_i}\frac{\nabla_\perp \cdot \delta \mathbf{E}_\perp}{B} - \frac{1}{\nu_i}\frac{k_B T_e}{m_i}\nabla_\perp^2 \frac{\delta n}{n_0}\Big) \tag{3.39}$$

Now re-arranging the terms of eqn. 3.39, we get the following as,

$$\frac{\nabla_\perp \cdot \delta \mathbf{E}_\perp}{B}\Big(\Psi\frac{\Omega_i}{\nu_i}\Big) = \nabla \cdot \delta \mathbf{v}_e - \frac{\Psi}{\nu_i}\frac{k_B T_e}{m_i}\nabla_\perp^2 \frac{\delta n}{n_0} \tag{3.40}$$

From the equation of continuity, we also know that,

$$\frac{\partial}{\partial t}\frac{\delta n}{n_0} + \mathbf{V}_e \cdot \nabla \frac{\delta n}{n_0} = -\nabla \cdot \delta \mathbf{V}_e \tag{3.41}$$

From the ion equation, we have,

$$-\frac{\delta^2}{\delta t^2}\frac{\delta n}{\delta n_0}-\nu_i\frac{\partial(\delta n/n_0)}{\partial t}=\Omega_i\nabla_\perp\cdot\frac{\delta\mathbf{E}_\perp}{B}-C_i^2\nabla_\perp^2\frac{\delta n}{n_0} \tag{3.42}$$

Rearranging the terms for eqn. 3.42 we get the following as,

$$\frac{\nabla_\perp\cdot\delta\mathbf{E}_\perp}{B}=-\frac{1}{\Omega_i}\frac{\partial^2}{\partial t^2}\frac{\delta n}{n_0}-\frac{\nu_i}{\Omega_i}\frac{\partial}{\partial t}\frac{\delta n}{n_0}+\frac{C_i^2}{\Omega_i}\nabla_\perp^2\frac{\delta n}{n_0} \tag{3.43}$$

Using eqn. 3.41 in eqn.3.40 and comparing eqn.3.40 and eqn. 3.43 we get,

$$C_s^2\nabla_\perp^2\frac{\delta n}{n_0}-\frac{\partial^2}{\partial t^2}\frac{\delta n}{n_0}-\nu_i\frac{\partial}{\partial t}\frac{\delta n}{n_0}=\frac{\nu_i}{\Psi}\frac{\partial}{\partial t}\frac{\delta n}{n_0}-\frac{\nu_i}{\Psi}\mathbf{V}_e\cdot\nabla\frac{\delta n}{n_0} \tag{3.44}$$

Finally, we arrive at,

$$\Big(\frac{\partial}{\partial t}+\frac{\mathbf{V}_e}{1+\Psi}\cdot\nabla\Big)\frac{\delta n}{n_0}=\frac{\Psi/\nu_i}{1+\Psi}\Big(C_s^2\nabla_\perp^2\frac{\delta n}{n_0}-\frac{\partial^2}{\partial t^2}\frac{\delta n}{n_0}\Big) \tag{3.45}$$

After the end of this derivation in Eqn. 3.45, Ψ represents a more generalized form to include the effects of the $E_\parallel$.

3.1.4 Analyzing the dispersion relation using a multi-timing technique

In the derivation that I presented it was already implicitely assumed that there was a fast time scale associated with the set up of the polarization field through a balance between perturbed Hall and Pedersen currents. Ion inertia and diffusion were considered to be associated with much longer time scales. Nevertheless, the final dispersion relation contains a second time derivative. As argued in *Hamza and St-Maurice* [1993] and as I am about to present, a multi-timing analysis of the equation turns this second time derivative into a second derivative in space. Viewing the system through that point of view proves useful later on when nonlinear processes are introduced in the analysis.

We recognize that the fast time-scale gave

$$\left[\frac{\partial}{\partial t_f}+\frac{\mathbf{V}_e\cdot\nabla}{1+\Psi}\right]\frac{\delta n}{n_0}=0 \tag{3.46}$$

This implies,

$$\frac{\partial}{\partial t_f} = -\frac{\mathbf{V}_e \cdot \nabla}{1+\Psi} \tag{3.47}$$

Eqn. 3.47 shows that the structures (blob/hole) move with a drift velocity $\mathbf{V}_e$. Using,

$$\frac{\partial}{\partial t} = \frac{\partial}{\partial t_{fast}} + \epsilon \frac{\partial}{\partial t_{slow}} \tag{3.48}$$

with $|\epsilon| << 1$ we end up with,

$$\frac{\partial}{\partial t_{slow}}\left(\frac{\delta n}{n_0}\right) = \frac{-\Psi}{\nu_i(1+\Psi)}\left[\frac{\partial^2}{\partial {t_{fast}}^2}\frac{\delta n}{n_0} - C_s^2\nabla^2\frac{\delta n}{n_0}\right] \tag{3.49}$$

or

$$\frac{\partial}{\partial t_{slow}}\left(\frac{\delta n}{n_0}\right) = \frac{-\Psi}{\nu_i(1+\Psi)}\left[\frac{(\mathbf{V}_e \cdot \nabla)^2}{(1+\Psi)^2}\frac{\delta n}{n_0} - C_s^2\nabla^2\frac{\delta n}{n_0}\right] \tag{3.50}$$

$$\frac{\partial}{\partial t_{slow}}\left(\frac{\delta n}{n_0}\right) = \frac{\Psi}{\nu_i(1+\Psi)}\left[-\frac{V_e^2}{(1+\Psi)^2} + C_s^2\right]\nabla^2\frac{\delta n}{n_0} \tag{3.51}$$

since V_e is assumed to be constant.

From Eqn. 3.46 we can say that convective derivative is a wave since $f(x - Vt)$ is solution to wave equation and solution to $\left[\frac{\partial}{\partial t} + V\frac{\partial}{\partial x}\right] = 0$. In other words, the structure or the enhancement is moving with a velocity $V = V_e/(1+\Psi)$.

From Eqn. 3.51 we can see that if $V < C_s$, we have ordinary diffusion, and the structure decays. However, for $V > C_s$ then we have anti-diffusion. As shown in Fig. 3.3 if a structure is not elongated enough, diffusion in the y-direction gains in importance. Thus, the fastest growing structures are those for which the y derivatives in the density perturbations are much smaller initially than the x derivatives in the density perturbations. Once anti-diffusion is strong enough an elongated structure will continue to be elongated as illustrated in Fig. 3.3 where regular diffusion elongates the structure in the y-direction, but in the x-direction, anti-diffusion acts inward and compresses it [*Drexler*, 2005, *St.-Maurice and Hamza*, 2001].

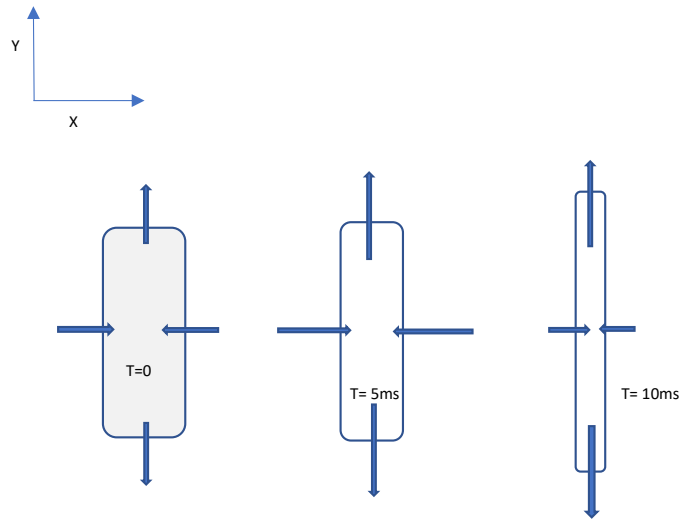

Figure 3.3: Evolution of a structure in the x-y plane under the influence of diffusion in the y direction and “anti-diffusion" from the Farley-Buneman instability in the x-direction, shown at three different times. Reproduced after [*Drexler*, 2005]

3.1.5 Gradient-Drift growth mechanism

While the focus has been thus far on Farley-Buneman it should be kept in mind as was first pointed out by *Rogister and D'Angelo* [1972] that there is a very similar instability associated with density gradients, called the gradient-drift (GD) instability. The treatment is very similar to the FB treatment to the point that the eigenfrequency is identical and that we simply need to add another growth rate to the equation. Indeed the FB growth rate and GD growth rate can be considered together as a new total growth rate [*St.-Maurice et al.*, 1994b].

To deal with the GD instability, we consider a geometry with a plasma density wave with its wavevector along the x direction. When a propagating wave has a gradient in density along the direction of the background electric field (-y as shown in Fig. 3.4), this density gradient provides a destabilization mechanism. Due to the perturbed electric field ($\delta\mathbf{E}$) there is a generation of $\delta\mathbf{E}\times\mathbf{B}$ drift along the y direction. As a result of this, the electrons are moved from the regions of high localized densities towards the region of low densities. There is then a gradual increase of $\delta n/n_0$. The situation is opposite in the region of depleted density enhancing the more negative value of $\delta n/n_0$ [*Baumjohann and Treumann*, 2012, *Drexler*, 2005, *Hargreaves*, 1992].

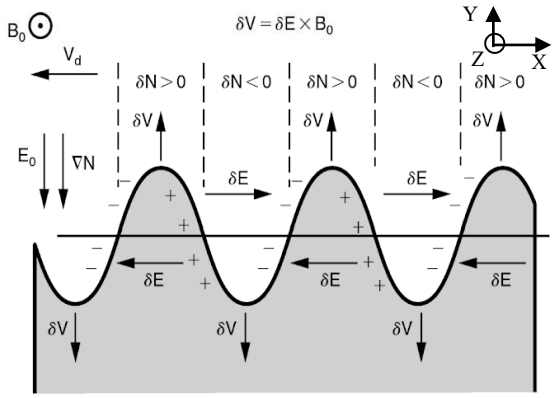

Figure 3.4: A schematic diagram of gradient drift instability driven by an electric field is shown here. Dark regions represent high density and the light regions are of low density. From *Kelley* [2009]

In the work by *Drexler et al.* [2002], the calculations related to the derivation for growth rate has been shown. Based on few of his equations, I want to emphasis here, the discussion on two time-scales, namely, fast and slow time-scales. For simplicity, we focus on the background density gradient effects here. We consider perturbed electron velocity, namely $\delta V_e = \frac{\delta E}{B}$ along y direction. The continuity equation is shown as:

$$\frac{\partial \delta n}{\partial t} = -\frac{\partial}{\partial x}\delta(nV_{ex}) - \frac{\partial}{\partial y}\delta(nV_{ey}) \tag{3.52}$$

However, in the x direction charge neutrality must be valid. Neglecting the y derivatives in the perturbed quantities again, and assuming that the unperturbed V_{e0y} is negligible, we find that

$$\frac{\partial \delta n}{\partial t} = -\frac{\partial}{\partial x}\delta(n_0 V_{i0}) - \delta V_{ey}\frac{\partial n_0}{\partial y} \tag{3.53}$$

followed by a few calculations as shown in *Baumjohann and Treumann* [2012], *Drexler* [2005] we arrive at:

$$\frac{\delta E}{B} = \frac{\nu_i}{\Omega_i}\frac{V_d}{(1+\psi)}\frac{\delta n}{n_0} = \frac{\nu_i}{\Omega_i}V_d\frac{\delta n}{n_0} \tag{3.54}$$

and, with $V = \frac{V_d}{1+\psi}$ substituting the result from Eqn. 3.54 back into Eqn. 3.53, we get

$$\frac{\partial \delta n}{\partial t} = -n_0 V\frac{\partial}{\partial x}\frac{\delta n}{n_0} - n_0\frac{\nu_i}{\Omega_i}V\frac{\delta n}{n_0}\frac{\partial n_0/\partial y}{n_0} \tag{3.55}$$

Next we define the background density scale L in the y direction via,

$$L = -\left(\frac{1}{n_0}\frac{\partial n_0}{\partial y}\right)^{-1} \tag{3.56}$$

The negative sign indicates that the gradient in the negative y-direction which makes L positive. L is considered positive if it is in the direction of decreasing density, and positive if it is in the direction of increasing density [*Baumjohann and Treumann*, 2012, *Drexler*, 2005, *Kelley*, 2009]. With this, we arrive at

$$\left[\frac{\partial}{\partial t} + V\frac{\partial}{\partial x}\right]\frac{\delta n}{n_0} = \frac{\nu_i}{\Omega_i}V\frac{\delta n}{n_0}\frac{1}{L} \tag{3.57}$$

The left-hand-side describes, as before, the fast time scales associated with wave propagation, while the right-hand-side is associated with the slow time scales related to the growth of the waves.

3.2 Aspect angle complications arising from nonlocal effects

I have already shown that if the aspect angle is too large the instability cannot grow. An interesting feature uncovered by *Drexler* [2005] and *Drexler et al.* [2002] is that because the eigenfrequency is actually a function of height, weak as this dependence may be, it will introduce a change in the value of $k_{\parallel}/k_{\perp}$, namely, in the aspect angle. *Drexler et al.* [2002] found furthermore that the aspect angle must increase monotonically with time. This means that one should keep in mind that the growth time of the unstable structures is necessarily finite.

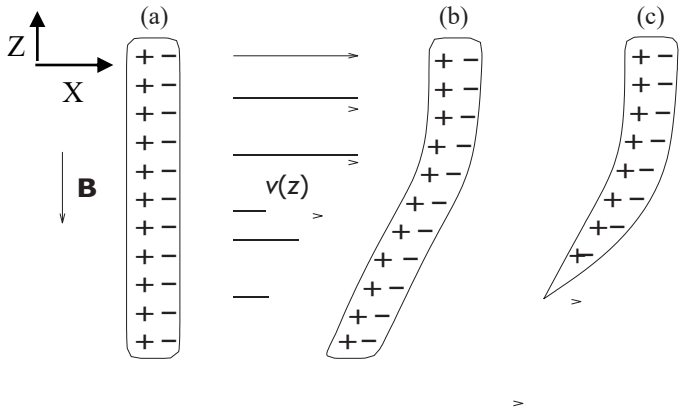

Figure 3.5: Sketch of a shoebox-like density enhancement that shows how a magnetic field-aligned structure evolves with time in physical space. At first the shoebox is aligned along the magnetic field-direction shown here as the vertical direction. The direction of the electron $\mathbf{E} \times \mathbf{B}$ drift points to the right along the x-axis. From *Drexler* [2005].

It is important to understand the physical process at work here. To that goal, Fig. 3.5 produces a sketch of the evolution of a shoebox-like density enhancement (blob) in space which is initially elongated with the magnetic field direction with $\mathbf{k}_{\|} \sim 0$ [*Drexler*, 2005]. The evolution of the shoebox is triggered by the fact that V_d increases with height. happens due to the fact that frequency increases with height. As a result, the edge of the box that is positively charged ends up on the same magnetic field line as the negatively charged edge. This means that the parallel electric field increases monotonically with time, and with it the aspect angle. This also means that sooner or later the structures will develop a decaying amplitude and will ultimately disappear from the system. Interestingly enough, the parallel electric field will accelerate the electron and heat them through frictional heating, meaning that the electrons will end up with the energy of the waves. The fact that the electron temperature increases hand in hand with the instability growth rate has been observed repeatedly (e.g., *Foster and Erickson* [2000] and references therein).

An equivalent point of view based on a wave analysis is presented in Fig. 3.6. In this case instead of thinking in terms of a faster velocity at the top we think of a greater frequency. The is equivalent since $\omega = \mathbf{k} \cdot \mathbf{V}_d/(1 + \Psi)$. Again if we assume that there is no phase variation initially the aspect angle is zero. As shown the figure this does not last forever as the faster oscillations higher lead to a phase that changes increasingly strongly with time.

The upward motion of the center-of-mass of the structure that can be seen in Fig. 3.5 can be

described by a group velocity, which means that as the aspect angle grows with time the structures runs away from the unstable region. Indeed *Moorcroft* [1984] pointed out that as the aspect angle increases the component of the group velocity along the magnetic field can exceed 40 km/s by the time the aspect angle is too large for a structure to grow. Since the region is only about 20 km thick the implication is that the structures will decay after a time scale of the order of 0.5 s.

Drexler [2005] has offered a mathematical treatment of this problem through the derivation of the following generalized amplitude equation to decribe the growth of the unstable waves:

$$\frac{\partial \ln A}{\partial t} + V_{g\parallel}\frac{\partial \ln A}{\partial z} = \gamma_{FB} + \gamma_{GD} - \frac{1}{2}V_{g\parallel}\left(\frac{1}{k_\parallel}\frac{\partial k_\parallel}{\partial z} + \frac{2}{\omega'}\frac{\partial \omega'}{\partial z} + \frac{\Psi}{\mathbf{k}_\perp \cdot \mathbf{V}_d}\frac{\partial \mathbf{k}_\perp \cdot \mathbf{V}_d}{\partial z} + \frac{\partial \ln n_0}{\partial z}\right) \quad (3.58)$$

where A is the amplitude of the wave, $\gamma_{FB} = \frac{(\omega'^2 - k^2 C_s^2)\Psi}{(1+\Psi)\nu_i}$ and $\gamma_{GD} = \frac{\omega'}{k}\frac{\nu_i}{\Omega_i(1+\Psi)} \mid \hat{\mathbf{k}}_\perp \times \nabla_\perp \ln n_0 \mid$ are the standard local growth rates for Farley-Buneman and gradient-drift instabilities. Also, $\omega' = \mathbf{k}_\perp \cdot \mathbf{V}_d/(1+\Psi)$, $\Psi = \Psi_0\left(1 + \frac{k_\parallel^2 \Omega_e^2}{k_\perp^2 \nu_e^2}\right)$, $\Psi_0 = \frac{\nu_e \nu_i}{\Omega_e \Omega_i}$ and $\gamma_{conv} = \frac{1}{2}V_{g\parallel}\left(\frac{1}{k_\parallel}\frac{\partial k_\parallel}{\partial z} + \frac{2}{\omega'}\frac{\partial \omega'}{\partial z}\right)$ and $\gamma_{vert} = -\frac{V_{g\parallel}}{2}\frac{\partial \ln n_0}{\partial z}$ are the two growth terms from the non-local effects. The first non-local term γ_{conv} is known as convective growth rate as it is related to a convective nature of instability [*Chen*, 1996] and the second term γ_{vert} is related to growth owing to the presence of a vertical plasma density gradient. These terms contribute to a change in amplitude and therefore growth/decay of the wave. *Drexler* [2005] pointed out that the only important nonlocal term is the one with gradient in the background plasma density. Since it is multiplied by the group velocity, it can cause substantial growth or decay of the wave in later stages. It should also be noted that when $k_\parallel << k_\perp$ (near zero aspect angle) we have $V_{gr\parallel} \rightarrow 0$ and the amplitude is then simply described by the linear isothermal theory discussed in a previous section.

For many years it was thought that $\mathbf{k}_\parallel$ was a free parameter. However, with the non-local effects described in *Drexler* [2005], the so-called 'eigenfrequency' is a function of altitude as shown Fig. 3.6. Therefore, a single frequency cannot describe the evolution of a wave train, at least not if a plane wave solution is assumed to describe the system. If one nevertheless chooses to describe the perturbations in terms of train of plane waves, a judiciously chosen number of plane waves can be used. No matter what, a time scale of the order of 1 second agrees with the previous parallel group velocities calculation by *Moorcroft* [1984]. This means that for a 10 m structure, an electric field of 50 mV/m or greater is enough to overcome the non-local effect and have a decent amplitude

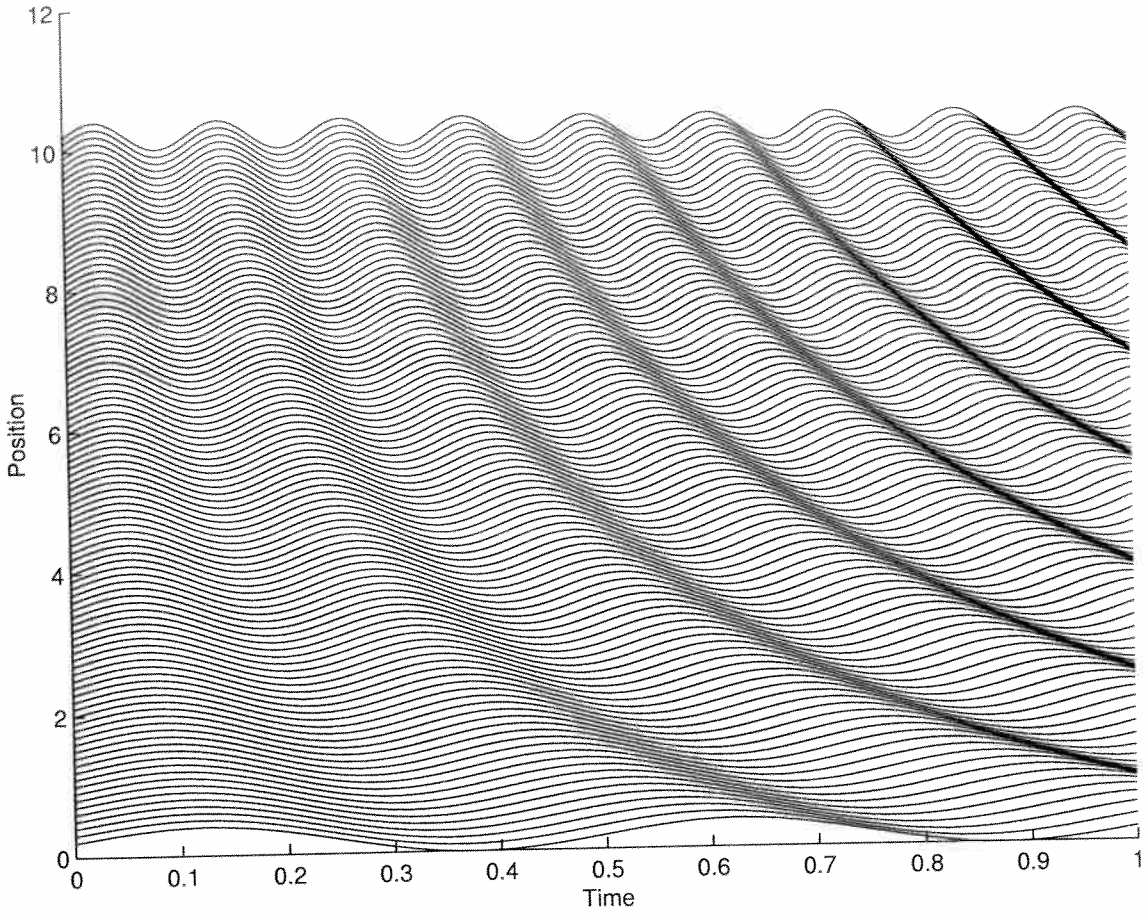

Figure 3.6: This figure shows a series of oscillations. Initially, at $t = 0$ the phase of the oscillations is same at all heights. A phase change starts to develop with time which is related to $k_{||}$ along magnetic field direction. From [*Drexler et al.*, 2002].

gain. For faster growing modes associated with smaller wavelengths, the primary focus is on the perpendicular non-linearities leaving behind the final stages of evolution associated with non-local effects. An example of this is shown in Fig. 3.7.

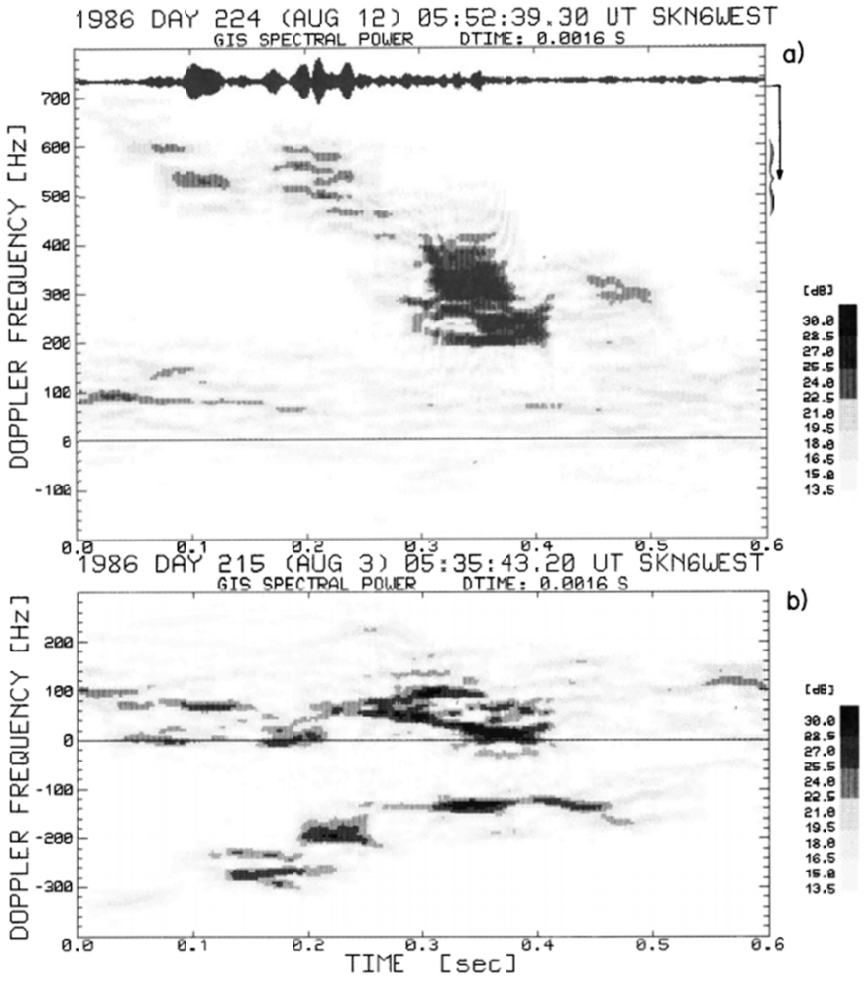

Figure 3.7: The 64-ms window FFT power spectra shown for two separate ' Doppler velocity events' observed by one of the 50 MHz radars used during the CW experiments reported by *Prikryl et al.* [1990]. The time series was processed by successive advances of a 64-ms window by 1.6 ms. The largest amplitude was found near the ion acoustic speed (close to 200 Hz on the top figure), while the smallest amplitude had a much larger Doppler shift that may well have been comparable to the plasma $\mathbf{E} \times \mathbf{B}$ [*Prikryl et al.*, 1990].

Fig. 3.7 will be discussed in more detail in chapter four. Nonlinear theories based on E field perpendicular to B will be handled in chapter 4.

3.3 Kinetic Description of the Linear Theory

A more general treatment of the plasma is based on kinetic theory, which deals with the velocity distribution of the particles. The fluid equations are based on velocity moments of the velocity distributions and are therefore less general, i.e., contain less information.

In kinetic theory, the velocity distribution of a particular species, $f(\mathbf{r}, \mathbf{V}, t)$, describes the probability of finding particles in a velocity interval $(\mathbf{V}, \mathbf{V} + \delta\mathbf{V})$ and at a position interval $(\mathbf{r}, \mathbf{r} + \delta\mathbf{r})$ at time t. The Boltzmann equation is used to describe f as discussed in *Farley* [1963] and is written as

$$\frac{\partial f}{\partial t} + \mathbf{V} \cdot \nabla f + \frac{q}{m}(\mathbf{E} + \mathbf{V} \times \mathbf{B}) \cdot \nabla_V f = \left.\frac{\partial f}{\partial t}\right)_c \tag{3.59}$$

where q, m, $\mathbf{r}$ and $\mathbf{V}$ are the charge, mass, position and velocity of the particle respectively, $\mathbf{B}$ is the magnetic field and $\nabla_V f$ is the gradient of f in velocity space. The term on the right-hand-side of Eqn. (3.59) is a collision operator. In the ionosphere it describes binary collisions, and is therefore described in general by the Boltzman collision integral [*Farley*, 1963]. For simplicity it is often replaced by the Langevin collision operator, which reads:

$$\left(\frac{\partial f}{\partial t}\right)_c = -\nu \left(f - \frac{N}{N_m} f_m\right) \tag{3.60}$$

where ν is the average collision frequency and N and N_m are the number density associated with f and f_m. The operator describes the tendency for collisions to damp out the perturbations in the distribution function over a time of order of ν^{-1} [*Farley*, 1963]. For applications to the lower ionosphere the collision model is used to describe the collision of electrons and ions with the neutrals, so that f_m is the neutral velocity distribution function.

When dealing with perturbations in the velocity distribution as is the case for a study of instability mechanism, we use $f = f_0 + f_1$ and apply the collision operator to each part of the distribution separately. We therefore deal with

$$\left.\frac{\partial f_1}{\partial t}\right)_c = -\nu \left[f_1 - \frac{N_1}{N_m} f_m\right] \tag{3.61}$$

To write the full equation for f_1 we likewise break the acceleration into two terms

$$\mathbf{a} = \mathbf{a}_0 + \mathbf{a}_1 \tag{3.62}$$

where $\mathbf{a}_0$ is the acceleration without perturbation and $\mathbf{a}_1$ is the perturbed acceleration. If we assume the small order of perturbation to vary harmonically as $\exp[i(wt - \mathbf{k} \cdot \mathbf{r})]$ we can then write for f_1

$$i(\omega - \mathbf{k} \cdot \mathbf{V})f_1 + \frac{q}{m}\mathbf{E}_1 \cdot \nabla_v f_0 + \frac{q}{m}(\mathbf{V} \times \mathbf{B}_0) \cdot \nabla_V f_1 = \left.\frac{\partial f_1}{\partial t}\right)_c \tag{3.63}$$

This equation is describing the velocity distribution in a cylindrical coordinate system centered on the $\mathbf{E}_0 \times \mathbf{B}$ drift so that $\mathbf{E}_0 \cdot \nabla_V f_1$ is no longer present in the equation as long as it can be assumed that the distribution functions are axisymmetric. In the $\mathbf{E}_0 \times \mathbf{B}$ centered coordinate expressed in cylindrical coordinates, the velocity divergence is described in this case through $a_0 \cdot \nabla_V f_1 = \Omega \frac{\partial f_1}{\partial \Theta}$ where Θ is an angle measured from the $\mathbf{E} \times \mathbf{B}$ point in velocity space. Note that the absence of an explicit $\mathbf{E}_0 \cdot \nabla_\mathbf{V}$ term does not mean that there is no $\mathbf{V}$ derivative in the electric field direction. Rather, it means that a cylindrical coordinate is being used.

Now if we include collisions through the Langevin collision operator we find

$$i(\omega - i\nu - \mathbf{k} \cdot \mathbf{V})f_1 + \frac{q}{m}\mathbf{E}_1 \cdot \nabla_V f_0 + \frac{q}{m}(\mathbf{V} \times \mathbf{B}_0) \cdot \nabla_V f_1 = \nu \frac{N_1}{N_m} f_m \tag{3.64}$$

If one can assume that both f_0 and f_m are Maxwellians and that the temperatures of the ions and neutrals (but not the electrons) are the same, the dispersion relation can be retrieved using a method of characteristics that integrates along the ion trajectories expressed in the cylindrical coordinate system. After a fair amount of algebra that can be nevertheless found in various textbooks (for example, *Ichimaru* [1973]) one finds (e.g., *St-Maurice and Schlegel* [1983])

$$(k\lambda_D)^2 + \frac{T_e}{T_i}\frac{\left[1 + \frac{\omega - \mathbf{k}\cdot\mathbf{V}_d + i\nu_i}{\omega V_{Ti}} Z\left(\frac{\omega - \mathbf{k}\cdot\mathbf{V}_d + i\nu_i}{kV_{Ti}}\right)\right]}{\left[1 + \frac{i\nu_i}{kV_{Ti}} Z(\frac{\omega - \mathbf{k}\cdot\mathbf{V}_d}{kV_{Ti}})\right]} + \frac{\left[1 + \frac{\omega + i\nu_e}{k_\parallel V_{Te}} e^{-\mu_e} \sum_{n=-\infty}^{\infty} I_n(\mu_e) Z(\frac{\omega + i\nu_e - n\Omega_e}{k_\parallel V_{Te}})\right]}{\left[1 + \frac{i\nu_e}{k_\parallel V_{Te}} e^{-\mu_e} \sum_{n=-\infty}^{\infty} I_n(\mu_e) Z(\frac{\omega + i\nu_e - n\Omega_e}{k_\parallel V_{Te}})\right]} = 0 \tag{3.65}$$

where

$$\mu_e = 1/2(k_\perp V_{Te}/\Omega_e)^2 \tag{3.66}$$

$$\Omega_e = eB/m_e \tag{3.67}$$

$$\lambda_D^2 = kT_e/4\pi n_0 e^2 \tag{3.68}$$

$$V_{T_i,T_e} = (2kT_{i,e}/m_{i,e})^{1/2} \tag{3.69}$$

$$k_\parallel = k\cos\theta \tag{3.70}$$

$$k_\perp = k\sin\theta \tag{3.71}$$

k is the wave vector, θ is the angle with the magnetic field, $\mathbf{V}_d$ is the relative motion between electrons and ions, ν_i, ν_e is the ion and electron neutral collision frequencies respectively, n_0 is the background density, γ is the imaginary part of the growth-rate, Z is the plasma dispersion function and I_n is the modified Bessel Functions.

This approach was first developed by *Farley* [1963], where he neglected the Debye length effects ($k\lambda_D \rightarrow 0$) and he only considered $k_\parallel = 0$. Later on, *Chaturvedi and Ossakow* [1979] included the $k_\parallel$ effects and also assumed $T_e = T_i$. Later on, while studies were done with $Te \neq Ti$ by *St-Maurice and Schlegel* [1983], it was found that in the case where $T_e > T_i$ where the wavelength and the phase velocity of the unstable wave both increase. Also, the growth rate decreases considerably because Landau damping increases with increasing T_e. Interesting point to note that for fluid modes the growth rate keeps increasing as k gets larger (smaller wavelengths) whereas in the kinetic regime there is a point at which growth stops at shorter wavelengths.

Chapter 4

Non-linear Theories

Linear theory can only tell us why and where, in altitude, the irregularities should be present and under what circumstances. Controlling factors are the electric field, ion-acoustic speed, density gradients, and altitude, as discussed in Chapter 3 on linear theory. However, a linear theory is not capable to deal with the amplitude of the structures or their phase velocity. It cannot be used to describe the spectral width or spectral shape seen through radar or rocket spectra because linear theory ignores wave saturation mechanisms and related effects that are produced by non-linear and non-local processes [*St.-Maurice and Hamza*, 2009].

Non-linear questions to ask include the following:

1. Amplitude of the waves: in principle, non-linear processes limit the amplitude of the waves. The first thing non-linear effects do is to limit the amplitude of the waves through the introduction of saturation. Related observations have been discussed in the Chapter 2, where it was shown that in the E-region the waves are moving with velocities much less than E/B and much closer to the ion-acoustic speed. Plasma physicists have been traditionally keying on the maximum growth rates when dealing with large amplitude waves. However, the example in hand does not reflect this situation.

2. Dominant phase velocity, $\mathbf{V}_p$, at saturation: the waves reach their largest amplitude when moving at the ion-acoustic speed [*St.-Maurice and Hamza*, 2009].

3. Spectral shape: as mentioned in [*Hamza and St-Maurice*, 1993], if the medium is more turbulent, then the spectrum becomes wider. A wide spectrum means a wide range of frequencies to consider while a very narrow spectrum means that there is basically a single frequency of interest.

4. The electrons are heated by the Farley-Buneman (FB) waves [*St-Maurice and Schlegel*, 1983].

5. Anomalous conductivities: some researchers have been stating that the heating of electrons in the plasma is related to anomalous resistivity. This notion has proven to be incorrect [*St.-Maurice and Hamza*, 2001]. However, when there is instability, currents can be interrupted and are therefore affected. This property can be related to the concept of anomalous conductivities [*St.-Maurice and Hamza*, 2009]. The real question to ask is: does turbulence affect the conductivities through Pedersen and Hall drifts modifications in the presence of the turbulent structures?

To deal with non-linear effects *St-Maurice and Schlegel* [1983] assumed originally that the amplitude of a wave would be proportional to the growth. It was assumed that if the waves grow faster, they will end up with large amplitude and if the waves grew slowly, they would not reach a large amplitude. This result did not seem righ because it did not produce large amplitudes at the ion-acoustic speed, as was becoming increasingly evident after more experimental results came in. This meant that the growth rate itself had nothing to do with the amplitude of the waves at saturation. However, later on, it was found experimentally that as the amplitude grows the frequency decreases *Prikryl et al.* [1990]. This was the main reason why the largest amplitudes were not found in the modes with the fastest growth rate modes [*St.-Maurice and Hamza*, 2009].

Another point discussed by *St-Maurice and Schlegel* [1983] was that at 110 km altitude the aspect angle, as defined through the ratio $k_{\parallel}/k_{\perp}$, is close to 1° for the largest growth rate of the instability, meaning that the fastest growth rates were to be observed at aspect angles close to 1°. Conversely, at altitudes closer to 100 km the largest growth rate is found to be near $k_{\parallel} = 0$. It was a common notion amongst the researchers around that time that there is more free energy if the growth rate is large. However, later on, it became clear that the growth rate is related to the spectral width $\Delta\omega$ and not to ω. If a wave grows fast, $\Delta\omega$ will increase. As a result, instead of relating the amplitude of the wave to the growth rate, later studies have been focusing on how to relate the growth rate (γ) of the plasma waves to $\Delta\omega$ [*Hamza and St-Maurice*, 1993].

Non-linearities in the E-region plasma are usually assumed to come from wave-wave interactions or mode-coupling. Following the early lead by *Sudan* [1983a], the main generator of the coupling was taken to be the $\nabla \cdot (\delta n \delta \mathbf{V})$ term from the continuity equation, with δn and $\delta \mathbf{v}$ being the

fluctuating density and electron velocity, respectively. We will not be dealing with other possible non-linearities in this thesis. This includes nonlinear Kinetic theory, which is best implemented to study the non-linear effects, including Doppler width or change in amplitude, through particle simulation codes [*Oppenheim et al.*, 1995]. The numerical simulations have proven to be handy as they do not care about the transport coefficients, temperature, drift or the electric field. Oppenheim and his co-workers have focused on 'Particles in Cells' computations for the electrons in the presence of a plasma rendered unstable via the Farley-Buneman mechanism.

Solving problems related to non-linearities in the E-region through the use of $\nabla \cdot (\delta n \delta \mathbf{V})$ has been looked at in order to explain the observations. To work with this nonlinearity we therefore need to establish a connection between the perturebed electron density and the perturbed velocities inside a medium. The change in density with respect to the background generates a perturbed electric field $\delta\mathbf{E}$. This drives a $\delta\mathbf{E} \times \mathbf{B}$ drift in the electrons. This $\delta\mathbf{V}$ can introduce a perturbed current ($\delta\mathbf{J}$) and a perturbed electric field component along the ambient electric field direction.

In Chapter 2 (Observations), structures observed by radars and rockets were discussed. We want to explain the basic properties of these structures based on nonlinearities introduced by the product of δn with $\delta\mathbf{V}$. In the plane-wave approximation wave-wave coupling amounts to combining various eigenmodes combine to generate large-amplitude steady-state fluctuations. This mode-coupling approach is discussed in detail in the present Chapter. Note that the product of the terms δn and $\delta\mathbf{V}$ is a flux and that the nonlinear effects are introduced through the divergence of this flux. In the next sections, I discuss the evolution of the techniques that were implemented to study E-region irregularities non-linearly while also addressing the non-linear questions raised at the beginning of this section.

4.1 Anomalous Diffusion:

Let's start with the discussion of amplitude saturation and techniques that have been used to study them theoretically. For shorter wavelengths associated with the FB mechanism, in particular, methods were developed to study how the plasma waves saturate. One approach has been anomalous diffusion. It provided a way to saturate unstable plasma waves at relatively small amplitudes while explaining an ion-acoustic saturation in the phase velocities. Anomalous diffusion was first

considered for this problem by [*Robinson*, 1986, *St.-Maurice*, 1987, *Sudan*, 1983b].

Sudan [1983b] argued that the nonlinear behavior comes from the momentum transfer between the electrons and the waves, thereby resulting in the cross-field electron diffusion. It was interpreted using effective electron collision frequency (ν^*). In other words, due to anomalous transport associated with changes in the electron orbit, ν changes to ν^*. As a result of this ψ increases to become so large as to make the electrons go at C_s [*Sudan*, 1983b]. That is to say:

$$\psi^* = \frac{{\nu_e}^* \nu_i}{\Omega_e \Omega_i} \tag{4.1}$$

and

$$\omega_k^{NL} = \frac{kV_0 \cos\theta}{1 + \Psi + \Psi^*} \tag{4.2}$$

In the saturated state,

$$\omega_k^{NL} = kC_s = \frac{kV_0 \cos\theta}{1 + \Psi + \Psi^*} \tag{4.3}$$

This means that Ψ^* increases to shut-off the instability and simultaneously causes a shift in phase to keep nonlinear phase velocity at C_s. Sudan also assumed,

$$V_0/C_s = \frac{1 + \epsilon}{1 + \Psi} \tag{4.4}$$

where $\epsilon > 0$. Unstable waves were generated along $\theta = 0$ which saturate at $\Psi^*(\theta = 0) = \epsilon(1 + \Psi)$. Nonlinearly unstable waves existed for $\theta > \theta_c$, where $\cos\theta_c = (1 + \epsilon)^{-1}$. For $\theta < \theta_c$, the saturation angle of these irregularities was determined by

$$\Psi^*(\theta < \theta_c) = (1 + \Psi)[\frac{(1 + \epsilon)\cos\theta}{(1 + \Psi)} - 1] \tag{4.5}$$

Clearly this meant that $\Psi^*(\theta)$ was a decreasing function of θ, which means saturated amplitude of the irregularity would be maximum in the $\mathbf{E} \times \mathbf{B}$ direction and decrease monotonically away from the $\mathbf{E} \times \mathbf{B}$ direction [*Sudan*, 1983b]. Sudan concluded in his work that the wave-induced diffusion is responsible for the stabilization of the Farley-Buneman waves by causing their phase speeds to be reduced to the ion-acoustics speed of the medium. *Sudan* [1983a] reported that rocket measurements related to the E-region electric field fluctuations were consistent with the wave

amplitudes. *Robinson* [1986] went further and related Sudan's anomalous diffusion to electron 'anomalous' heating wave heating by "friction" which, he argued, was a result of the effective collisions between the electrons and the waves. However, *St.-Maurice* [1987] studied the role played by anomalous diffusion on the evolution and possible saturation of the waves. He related ψ^* to $\delta n/n$ and calculated the net flux of the particles which depended on δn and $\delta\mathbf{V}$ using the known connection between δn and $\delta\mathbf{V}$ to calculate electron fluxes and to find ν^* which was expressed in terms of $(\frac{\delta n}{n})^2$. St.-Maurice obtained the expression for diffusion coefficient $D^* = \nu_e^* T_e/m_e\Omega_e^2$ as

$$D^*(\theta) = \Sigma_k \left|\frac{\delta\mathbf{E}_{kw}c}{\mathbf{B}_0}\right|^2 \frac{\sin^2(\theta-\theta')k^2(D+D^*(\theta'))}{(\omega_\mathbf{k}-\mathbf{k}\cdot\mathbf{u_e})^2}\frac{\Psi_0(\theta-\theta')}{1+\Psi_T(\theta-\theta')} \tag{4.6}$$

where

$$\Psi_0(\phi) = \Psi + \Psi^*(\phi) = \frac{\nu_i[\nu_{en}+\nu_e^*(\phi)]}{\Omega_i\Omega_e} \tag{4.7}$$

and where

$$D + D^*(\theta) \equiv \left[\nu_{en} + \nu_e^*(\theta+\frac{\pi}{2})\right]T_e/(m_e\Omega_e^2) \tag{4.8}$$

In Eqn. 4.6 θ is the angle at which the diffusion coefficient is being probed, while θ' is the angle between the wave vector $\mathbf{k}$ and the $\mathbf{u}_e$ or $\mathbf{E}\times\mathbf{B}$ drift. For the rest, Ψ is the usual expression in terms of ν_e^* instead of ν_e at $k_\parallel = 0$ and is now direction-dependent. Eqn. (4.6) was similar to what had been originally presented by *Sudan* [1983a], except for the factor $\Psi_0/(1+\Psi_T)$ in the integral. More importantly, according to the definition of ν_e^* mentioned in *St.-Maurice* [1987], the waves move in the $\mathbf{E}\times\mathbf{B}$ direction with respect to the neutrals at speeds of the order of ion-acoustic speed. If (4.6) is represented in terms of perturbed densities for the expression of ν_e^* we can write it as

$$\nu_e^*(\theta+\pi/2) = \Sigma_k \left|\frac{\delta n_{kw}c}{N}\right|^2 \frac{\sin^2(\theta-\theta')k^2\Omega_e^2)}{\nu_e n+\nu_e^*(\theta)}\frac{\Psi_0(\theta-\theta')}{1+\Psi_T(\theta-\theta')} \tag{4.9}$$

This equation has been discussed in *St.-Maurice* [1990]. If the wave energy is large only when the wave vectors point in the $\mathbf{E}\times\mathbf{B}$ direction, the fluctuation density δn_{kw} in Eqn. 4.9 can be approximated with a delta function at $\theta = 0$. This is presumably a valid first order model for well developed Farley-Buneman wave since the wave energy in that case peaks strongly in the $\mathbf{E}\times\mathbf{B}$ direction [*Ierkic et al.*, 1980]. In that case, it is easy to see that $\nu_e^*(\pi/2)$, or $D^*(0)$, vanishes because

of the $\sin(\theta - \theta')$ term in Eqn. 4.6 or Eqn. 4.9. This means that there can be no wave-induced diffusion to stabilize the growth in the $\mathbf{E} \times \mathbf{B}$ direction and anomalous diffusion can therefore not be responsible for the saturation of the large amplitude waves.

To summarize about the anomalous diffusion theories advanced to explain saturation at the ion-acoustic speed: (1) the direction of anomalous diffusion described initially by *Sudan* [1983b] should have been along the ambient electric field direction rather than along the $\mathbf{E} \times \mathbf{B}$. (2) The problem with anomalous diffusion was further compounded when *Robinson* [1986] added the frictional heating term between the waves and the electrons as if the waves had been particles. It reads as if the electrons are carrying energy in the form of wave packets. The problem here was that we are dealing here with very low-frequency waves. Given this, the wave packets cannot suddenly change the energy and momentum of electrons since for low-frequency waves, the electrons just $\mathbf{E} \times \mathbf{B}$ drift in the total electric field. As for electron heating by waves, it has been shown later on that the electrons can be heated through the parallel electric field effects coming from the late evolution in the waves which take place as they decay [*St.-Maurice and Hamza*, 2009].

If the two-dimensional anomalous diffusion mechanism was to matter, *St.-Maurice* [1987] later suggested that focus need to be given on a mechanism where a particular mode can produce its own turbulence, allowing, in turn, for the presence of secondary waves along the $\delta\mathbf{E} \times \mathbf{B}$ direction to be large enough to slow down the electrons to the ion-acoustic speed along primary direction [*St.-Maurice and Hamza*, 2009]. As mentioned in *St.-Maurice* [1987], the inferred $|\frac{\delta n}{n}|$ seemed distinctly higher than observed for this mechanism to work. It was pointed out, furthermore, that saturation with this mechanism implied $|\mathbf{E}_{blob}| > |\mathbf{E}_0|$ which should not be the case during instability since the role of instability is to decrease the rate at which it is produced. Increasing the electric field would do just the opposite. Therefore it was concluded that anomalous diffusion theory could provide a successful explanation to neither the wave amplitude saturation nor the dominant phase speed at saturation.

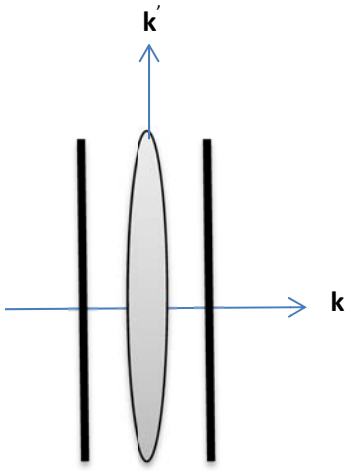

Figure 4.1: This diagram shows that the original **k** (small wavelength) is in the x-direction and the **k′** (large wavelength) along the y-direction. Through this example, it has been shown that the two wave vectors (along x and y) interact as discussed through $\nabla \cdot (\delta n \delta \mathbf{V})$.

4.2 Mode-Coupling:

With the above considerations in mind, Fig. 4.1 shows a very interesting point that needs to be considered, namely: in the irregularity studies being dealt with here, the process starts with elongated structures with short **k′**. Large **k** means small wavelengths along the x-direction. Big **k** are affected by short **k′** producing diffusion. This is the point which reflects that we need to use $\nabla \cdot (\delta n \delta \mathbf{V})$ not just $(\delta n \delta \mathbf{V})$. In *St.-Maurice* [1987] it has been discussed that the turbulence along the wavefronts produced $\nabla \cdot (\delta n \delta \mathbf{V})$. However, he never considered that into his work. Nevertheless, this brings us to consider mode-coupling as a strong possible saturation mechanism candidate, provided that $\mathbf{k}' \perp \mathbf{k}$ matters the most.

The mode-coupling idea starts by Fourier analyzing $\nabla \cdot (\delta n \delta \mathbf{V})$ which introduces the operator $i\mathbf{k}' \cdot \delta n_{\mathbf{k}-\mathbf{k}'} \delta \mathbf{V}_{\mathbf{k}'}$. The mode-coupling formalism is of course based on a plane wave decomposition of the turbulent density structures. Readers must be aware that the plane-waves are not solutions to non-linear equations [*St.-Maurice and Hamza*, 2009]. Sudan concluded that mode-coupling leads to power-law spectrum and cascading. What happens is that a structure is at first produced at a specific wavelength and ends up interacting with another structure with a different wavelength.

4.2.1 Sato's approach to mode-coupling

Along the above lines involving anomalous diffusion (which, however, had not been formulated at the time), *Tsuda and Sato* [1968] suggested that the observed type II echoes could be higher harmonic modes resulting from a continuous cascade of the wave energy from linearly unstable mode via mode coupling. Most importantly for the context of the present thesis, the non-linear evolution of the instability based on the coupling between modes perpendicular to one another, namely for situations of the kind described with Fig. 4.1 was, in fact, studied both numerically [*Sato and Tsuda*, 1968] and analytically [*Sato*, 1971]. This non-linear analysis was originally motivated to seek a better understanding of equatorial electrojet irregularities. The wavelength of the most unstable wave, in this case, was expected to be of the order of 100 meters but the radar observations are available mainly for 3-meter irregularities of type II which could be produced by the non-linear decay process from larger to smaller components [*Sato*, 1973]. *Sato* [1973] superimposed type I irregularities with type II and provided a theoretical basis unifying the two in his work. This approach introduced a first-hand concept of stabilizing the instability mainly by mode coupling by producing smaller irregularities [*Sato*, 1971]. Sato used gradients along the wavefront, assumed that there would be no net current and went on to calculate the resulting perturbation electric field. Then he showed that the phase velocity of the final structures had to decrease. The analogy to his paper is that

$$\mathbf{F}^* = \left\langle \delta n \delta \mathbf{V} \right\rangle \tag{4.10}$$

$$= n_0 \left\langle \frac{\delta n}{n_0} \frac{\delta \mathbf{E} \times \mathbf{b}}{B} \right\rangle \tag{4.11}$$

$$= n_0 \left\langle \frac{\delta n}{n_0} \frac{\delta E}{E_0} \frac{\mathbf{E}_0}{B} \right\rangle \tag{4.12}$$

$$= n_0 \left\langle \frac{\delta n}{n_0} \frac{\nu_i}{\Omega_i} \frac{1}{1+\Psi} \frac{\delta n}{n_0} \frac{\mathbf{E}_0}{B} \cos\phi \right\rangle \tag{4.13}$$

$$= \left\langle n_0 \alpha \left| \frac{\delta n}{n_0} \right|^2 \frac{\mathbf{E}_0}{B} \cos\phi \right\rangle \tag{4.14}$$

where ϕ is the phase difference between the fluctuating electric field and the fluctuating density while $\alpha = \frac{\nu_i}{\Omega_i} \frac{1}{1+\Psi}$. In the fluid regime considered by Sato and us as well, $\phi \approx 0$.

From Eqn. 4.14, one can extract an expression for the perturbed electric field from the

requirement that there be no current along the $\mathbf{E}_0$, or z-, direction. This gives

$$\delta E_z = -\alpha^2 \left|\frac{\delta n}{n_0}\right|^2 E_0^z \tag{4.15}$$

so that

$$E_{tot}^z = E_0 + \delta E_z = E_0 \left[1 - \alpha^2 \left(\frac{\delta n}{n_0}\right)^2\right] \tag{4.16}$$

As long as the electric field correction is only a fraction of the ambient electric field ($\alpha \delta n/n << 1$) we can also write

$$E_{tot}^z \approx E_0 \frac{1}{1 + \alpha^2 |\frac{\delta n}{n_0}|^2} \tag{4.17}$$

It follows that for small enough density or electric field perturbations, the phase velocity in the $\mathbf{E}_0 \times \mathbf{B}$ direction is expected to be given by

$$v_{ph} = \frac{E_0}{B}\left[1 - \alpha^2 \left(\frac{\delta n}{n_0}\right)^2\right] \approx \frac{E_0/B}{1 + \alpha^2 |\frac{\delta n}{n_0}|^2} \tag{4.18}$$

A more general approach is required if the correction to the ambient electric field is not small enough. In that case, the perturbed electric field induces another electric field correction in the $\mathbf{E}_0 \times \mathbf{B}$ direction which in turn changes the value of the polarization in the electric field direction and makes it smaller. One way to handle this situation is described in the next Chapter. Sato obtained the following expression for this more general case, by requiring that there be no currents along the z-direction at the z-nodes:

$$\delta E_z = -\frac{\mu_H^e}{\mu_P^i} V_{0y} \left|\frac{\delta N}{N_0}\right|^2 \frac{1}{1 + \left(\frac{\mu_H^e}{\mu_P^i}\right)^2 \left|\frac{\nabla N}{N}\right|^2} \tag{4.19}$$

$$= -\frac{1}{\mu_H^e} V_{0y} \alpha^2 \left|\frac{\delta n}{n_0}\right|^2 \frac{1}{1 + \alpha^2 \left|\frac{\delta n)}{n_0}\right|^2} \tag{4.20}$$

$$= -E_0^z \frac{\alpha^2 |\delta n/n_0|^2}{1 + \alpha^2 |\delta n/n_0|^2} \tag{4.21}$$

In Eqn. 4.21, μ_H^e is the Hall mobility for electrons and μ_P^i is Pedersen mobility for the ions. The end result for the final electric field value is the same as before, except that there is no longer any

small correction approximation. That is,

$$E_{tot}^z = E_0^z + \delta E_z = E_0^z \frac{1}{1 + \alpha^2(\delta n/n_0)^2} \tag{4.22}$$

At this point, it is important to note that the electron flux is being canceled by an equal ion flux from the ambient plasma so that the anomalous flux has been replaced by a polarization field. Therefore, in the Sato framework, the anomalous flux should be viewed only as a short-lived transient given by

$$\mathbf{F}^* = n_0 \alpha \left|\frac{\delta n}{n_0}\right|^2 \frac{\mathbf{E}_0 + \delta \mathbf{E}_z}{B} = n_0 \frac{\mathbf{E}_0}{B} \frac{\alpha \left|\frac{\delta n}{n_0}\right|^2}{1 + \alpha^2 |\delta n/n_0|^2} \tag{4.23}$$

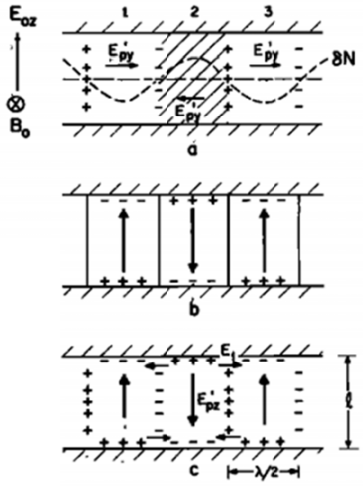

Figure 4.2: Movement of charges with a field-aligned perturbation is shown. Alternating electric field polarization (E'_{py}) are related with the density perturbation due to the presence of electric field E_{0z}. The alternately polarized electric fields drive electrons upward or downward in accord with the trough(section 1 and 2) or crest (sections 2, shadowed portion) of the density perturbation (b). As shown here, the upward and downward movements of electrons that produce space charges near the boundaries. The space charges produce secondary vertical polarization fields (E'_{pz}) and horizontal fields along the boundaries of the irregularity region (E_1) as shown in (c) [*Sato*, 1973].

Fig. 4.2 is extracted from *Sato* [1973] to illustrate more precisely what his approach was about. The shaded portion in Fig. 4.2(a) shows perturbation of the electrojet region caused by (in his case) large-scale structures moving to the west with a phase velocity v_{ph}. The polarization

electric field is generated through the density perturbation. The resulting electron motion in a reference frame moving with velocity v_{ph} is shown in Fig. 4.2(b). This movement of electrons help accumulate space charges near the vertical boundaries. For conducting boundaries, the charges would be short-circuited, and therefore the vertical motion of electrons and ions would no longer be affected. However, if there is a density inhomogeneity (as is the case in Sato's work since he uses nodes from a Fourier analysis of the densities in the vertical direction), a vertical polarization field is created instead. As shown in Fig. 4.2(c), the electrons move downward in regions 1 and 3 and they move upward in region 2. In Sato's view, an oscillating electric field is introduced at the vertical boundaries, given that a plane wave structured has been assumed in the horizontal direction [*Sato*, 1973].

4.2.2 The Hamza and St-Maurice approach

Based on work done by *Sudan* [1983b], a different approach to mode coupling was presented by *Hamza and St-Maurice* [1993] to study the relationship between Doppler shift and Doppler width. From the start, it was made clear that plane waves were not solutions to the nonlinear equations. However, plane waves provided an orthogonal basis to understand the plasma fluctuations. The physical reasoning that helps us understand the concept of wave decomposition technique is by analyzing the effects in weakly unstable situations introducing only small non-linear corrections. But if they are too strongly excited, new modes require corrections.

In principle. in the end, an infinite number of modes have to be considered so that, by then, none of the modes can exist without the influence of the other modes [*St.-Maurice and Hamza*, 2009]. *Hamza and St-Maurice* [1993] focused on the consequences of having a turbulent steady state at each wave-vector so that the average energy of the modes in the system neither grows nor decays on a time scale longer than that which was involved with the growth and/or decay time of structures associated with an individual mode coupling event. In the strong turbulence case of interest here, frequency broadening through mode coupling must be taken into account. By considering the waves perpendicular to the magnetic field (or very small aspect angles), the modes can be treated as being non-dispersive. Starting with the mode-coupling approach introduced by *Sudan* [1983a], *Hamza and St-Maurice* [1993] modified the original theory by removing the assumption that the phase velocity has to be close to the linear value. Instead, a self-consistent closure scheme was

invoked to determine the relationship between the mean Doppler shifts and the spectral widths in the E-region situation. The modes involved in the coupling did not have to be specified as long as the following condition was satisfied:

$$\mathbf{k_1} + \mathbf{k_2} = \mathbf{k_3} \tag{4.24}$$

However, at this point, in view of the strong turbulence conditions that could be taking place, the authors discarded the resonance condition described by weak turbulence, which reads

$$\omega_1 + \omega_2 = \omega_3 \tag{4.25}$$

In other words, the conservation of wave momentum and energy seem to be achievable through the three-wave interaction. However, this condition is not always followed in the cases related to strong turbulence [*St.-Maurice and Hamza*, 2009]. Many researchers have discussed how the spectral properties get affected while using mode-coupling (particularly, the three wave mode coupling) [*Hamza and St-Maurice*, 1993]. Their derivations start similarly to the framework introduced done by *Sudan* [1983b] and *Sahr* [1990]. In those treatments ions are considered to be collisional, strongly unmagnetized and non-convective. Electrons are strongly magnetized and weakly collisional and have negligible inertia. The plasma is, as always, quasi-neutral and chemistry, with its longer time scale, is not considered. However, background density gradients are included so that the gradient-drift instability can be included.

Just like *Hamza and St-Maurice* [1993] did, let us now focus only on the isothermal situation to avoid complications due to frictional heating, heat conduction and heat flows due to thermoelectric effect. The simplest case also involves negligible parallel fields. We need to recall that non-isothermal conditions are important below 100 km to study and understand the behavior of electrons. Similarly, at an altitude of 120 km, the growth rate of the ions is very small and therefore the non-linear ideas to relate amplitude with C_s do not apply [*Dimant and Oppenheim*, 2004]. We also define the parameters electron collision frequency (ν_e), ion collision frequency (ν_i), and electron gyro frequency (Ω_e).

In this framework, the starting equations are given by

$$\frac{\partial N}{\partial t} + \nabla \cdot (N\mathbf{V}_i) = 0 \tag{4.26}$$

$$\frac{\partial N}{\partial t} + \nabla \cdot (N\mathbf{V}_e) = 0 \tag{4.27}$$

$$\frac{\partial (N\mathbf{V}_i)}{\partial t} = -\frac{q_i}{m_i} N\nabla\Phi - \frac{\nabla P_i}{m_i} - \nu_i N\mathbf{V}_i \tag{4.28}$$

$$0 = -\frac{q_e}{m_e} N\big(\nabla\Phi - \mathbf{V}_e \times \mathbf{B}\big) - \frac{\nabla P_e}{m_i} - \nu_e N\mathbf{V}_e \tag{4.29}$$

After manipulating the electron momentum to the leading order in the ratio ν_e/Ω_e, we obtain

$$\mathbf{V}_e = \frac{1}{m_e\Omega_e^2}\mathbf{A} \times \Omega_e - \frac{\nu_e}{m_e\Omega_e^2}\mathbf{A} \tag{4.30}$$

$$\mathbf{A} = \nabla(q_e\Phi) + \frac{\nabla P_e}{N} \tag{4.31}$$

Zeroth-order gradients were considered by *Hamza and St-Maurice* [1993]. However, in my work, I have focused on the Farley-Buneman waves. Therefore, I did not include the effects due to parallel fields or the parallel density gradients. The resulting equation is given by

$$\frac{\partial n}{\partial t} + \mathbf{V}_\mathbf{E} \cdot \nabla n - \frac{\nu_e}{m_e\Omega_e^2 N_0}\nabla_\perp \cdot \{N\nabla_\perp(q_e\Phi) + \nabla_\perp P_e\} + \frac{1}{B}\nabla \cdot (\hat{\mathbf{z}} \times n\nabla\phi) = 0 \tag{4.32}$$

where

$$\mathbf{V}_E = \frac{1}{B}\mathbf{E}_0 \times \hat{\mathbf{z}} \tag{4.33}$$

I would like to inform the reader that $\hat{\mathbf{z}} = \mathbf{B}/B$ and only the perpendicular electric fields are considered here. With similar manipulations for ions and multiplying by the parameter Ψ a second equation relating n to Φ is obtained so as to close the system. The manipulations end up with

$$\frac{\psi}{\nu_i}\frac{\partial^2}{\partial t^2}n + (1+\Psi)\frac{\partial n}{\partial t} - \frac{\psi}{\nu_i m_i N_0}\nabla_\perp \cdot \{N\nabla_\perp(q_i\Phi) + \nabla_\perp P_i\} = 0 \tag{4.34}$$

where $\psi = \nu_e \nu_i / (\Omega_e \Omega_i)$. Next, 4.32 and 4.34 are combined to end up with

$$\frac{\psi}{\nu_i}\left(\frac{\partial^2}{\partial t^2} - C_s^2 \nabla_\perp^2\right) n + (1+\psi)\frac{\partial n}{\partial t} + \mathbf{V}_E \cdot \nabla n + \frac{1}{B}\nabla.(\hat{\mathbf{z}} \times n \nabla \phi) = 0 \tag{4.35}$$

where $C_s^2 = \frac{T_i + T_e}{m_i}$. Equation (4.35) involves two field variables, the number density and the potential fluctuations. Both terms come from electron equations. Because of that, another equation is still needed for system closure. To achieve this goal, and following *Sahr* [1990] Eqn. 4.35 is linearized in the limit of small frequencies ($\omega < \nu_i$) while throwing away the gradient effect on ions [*Hamza and St-Maurice*, 1993]. This produces the approximate balance:

$$\frac{\partial n}{\partial t} \approx \frac{q_i}{\nu_i m_i} \nabla_\perp^2 \phi \tag{4.36}$$

From Eqn. 4.36, we have the following:

$$i\omega_{\mathbf{k}} n_{\mathbf{k}} = -\frac{q_i}{\nu_i m_i} {k_1}^2 \phi_{\mathbf{k}} \tag{4.37}$$

Applying a Fourier transform on Eqn. 4.32 in space not in time and using Eqn. 4.37 to replace the potential fluctuations terms by density fluctuations, we get the following, after substituting $i\mathbf{k}_\perp$ for ∇:

$$\frac{\psi}{\nu_i}\left(\frac{\partial^2}{\partial t^2} - C_s^2 {k_\perp}^2\right) n + (1+\psi)\frac{\partial n}{\partial t} + i\mathbf{V}_E \cdot \mathbf{k} n - \frac{1}{B}\hat{\mathbf{z}}.[k_1 \phi_{k_1} \times k_2 n_{k_2}] = 0 \tag{4.38}$$

Now re-writing Eqn. 4.38 in a way where we can add all the modes together, we get

$$\left(\frac{\partial}{\partial t} + i\frac{\mathbf{k} \cdot \mathbf{V}_E}{1+\Psi}\right) n_{\mathbf{k}} + \sum_{\mathbf{k}_1, \mathbf{k}_2 = \mathbf{k} - \mathbf{k}_1} M_{\mathbf{k}\mathbf{k}_1\mathbf{k}_2} = -\frac{1}{1+\psi}\left\{\frac{\psi}{\nu_i}\left(\frac{\partial^2}{\partial t^2} + k_\perp^2 {C_s}^2\right)\right\} n_{\mathbf{k}} \tag{4.39}$$

$$M_{\mathbf{k}\mathbf{k}_1\mathbf{k}_2} = M_{\mathbf{k}\mathbf{k}_2\mathbf{k}_1} = M_{-\mathbf{k}-\mathbf{k}_1-\mathbf{k}_2} = i\frac{\nu_i}{2\Omega_i}\frac{\hat{\mathbf{z}} \cdot \mathbf{k}_1 \times \mathbf{k}_2}{1+\psi}\left(\frac{\omega_{\mathbf{k}_1}}{{k_1}^2} - \frac{\omega_{\mathbf{k}_2}}{{k_2}^2}\right) \tag{4.40}$$

In the linear approach, dropping the coupling coefficient terms, for the real-part of ω_k and for its imaginary-part (the growth rate γ_k), we get:

$$\omega_k = \frac{\mathbf{k} \cdot \mathbf{V}_E}{1+\Psi} \tag{4.41}$$

$$\gamma_k = \frac{1}{(1+\psi)}\left\{\frac{\psi}{\nu_i}({\omega_k}^2 - {k_\perp}^2 C_s^2)\right\} \tag{4.42}$$

From this, we find the coupling coefficient as,

$$M_{kk_1k_2} = i\frac{\nu_i}{2\Omega_i}\frac{\hat{\mathbf{z}}\cdot\mathbf{k_1}\times\mathbf{k}_2}{1+\psi}\left(\frac{\mathbf{k_1}\cdot\mathbf{V}_E}{{k_1}^2} - \frac{\mathbf{k}_2\cdot\mathbf{V}_E}{{k_2}^2}\right) \tag{4.43}$$

From Eqn. 4.43, it can be seen that $M_{kk_1k_2}$ is an imaginary term and therefore represents a nonlinear shift kn the eigenfrequency.

Important insights into the mode-coupling theory come from *Hamza and St-Maurice* [1993]. In this paper, a possible mechanism has been discussed to achieve steady-state turbulence. Steady-state turbulence is achieved when the amplitude of a wave could grow or decay at any time. Over a large volume and a longer period of time the structure would neither grow or decay [*St.-Maurice and Hamza*, 2001]. Therefore, temporal plane wave decomposition can be used to understand and describe the modes in terms of pure real frequencies. To define the spectrum $|n_k|^2$ for various modes, we start with defining, $n_{\mathbf{k}}(t)$, at time (t) as:

$$n_{\mathbf{k}\omega}(t) = n_{\mathbf{k}\omega}e^{-i\omega t} \tag{4.44}$$

If we multiply Eqn. 4.44 with the equation for $n^*_{\mathbf{k}}(t)$, then we get an equation for $|n_k|^2 = n_k n^*_k$. As defined in *Hamza and St-Maurice* [1993], the spectrum $N_{\mathbf{k}}$

$$N_{\mathbf{k}} = \Sigma_\omega |n_{\mathbf{k}}(\omega)|^2 \tag{4.45}$$

Now the average frequency ($\bar{\omega}_{\mathbf{k}}$) and a frequency spread ($\Delta\omega_{\mathbf{k}}$) are defined as:

$$\bar{\omega}_{\mathbf{k}} = \frac{1}{N_{\mathbf{k}}}\Sigma_\omega \omega |n_{\mathbf{k}}|^2 \tag{4.46}$$

$${\Delta\omega_{\mathbf{k}}}^2 = \frac{1}{N_{\mathbf{k}}}\Sigma_\omega(\omega - \bar{\omega}_{\mathbf{k}})^2 |n_{\mathbf{k}}|^2 \tag{4.47}$$

In terms of Eqn.4.47, the non-linear growth rate γ_k can be expressed as,

$$\gamma_k = \frac{\psi_0}{\nu_i(1+\psi_0)}(\bar{\omega}_k^2 + \Delta\omega_k^2 - k_\perp^2 C_s^2) \tag{4.48}$$

$$(\bar{\omega}_k^2 + \Delta\omega_k^2 - k_\perp^2 C_s^2) = 0 \tag{4.49}$$

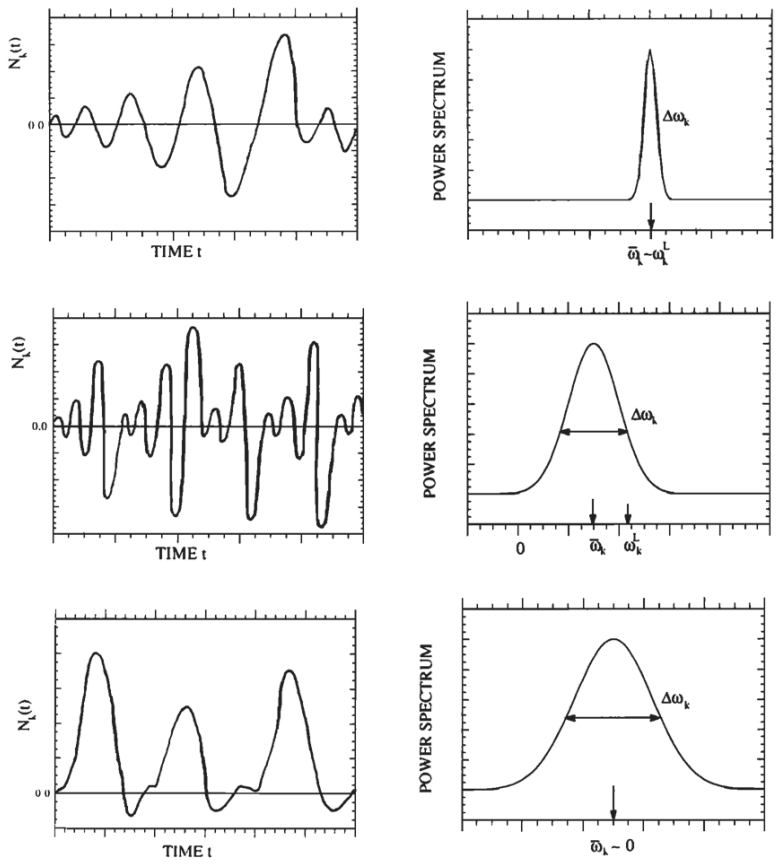

Figure 4.3: The top panel shows that linearly unstable waves loose energy fast after reaching a certain amplitude as can be shown through the spectrum. In the middle panel, the linear growth rate being large, the wave saturation is achieved quickly. The bottom panel shows what happens to the waves when they are fed energy periodically through mode-coupling. From *Hamza and St-Maurice* [1993]

In Eqn. 4.48, $\bar{\omega}_k$ is the mean frequency, and the $\Delta\omega_k^2$ is the square of the spectral width. Important insights to Eqn. 4.49 reveals that for a spectrum where the mean Doppler shift is larger than Doppler width, the mean Doppler-shift has to be comparable to the threshold speed. If the spectral width is very large while compared with the mean width, then according to this equation, the spectral width (in velocity units) is comparable to the ion-acoustic speed [*St.-Maurice and Hamza*, 2009]. If the modes are excited near the threshold frequency, that reflects a condition where the modes neither grow nor decay very fast *Hamza and St-Maurice* [1993]. Such modes usually have narrow spectra with large peak amplitudes as shown in top panel of Fig. 4.3. If a mode is excited way above the threshold, the mode can grow quickly followed by coupling to release

energy. This process happens very fast. Therefore spectrum around this kind of frequency is wide as shown in the middle panel of Fig. 4.3. To explain a similar situation where a particular mode receives energy through frequency below the threshold value, by the same mode-coupling process the amplitude can grow very fast and at the same time if that same mode decays fast, the spectrum becomes wide. At threshold value, the spectrum attains its peak and is symmetric around that frequency. This unique feature of mode-coupling explains the shape of type 1 spectra. However, type II echoes are observed when all modes decay very quickly after they grow from the other linear stable modes. Diffusion controls the decay rate and thereby the spectral widths are comparable to ion-acoustic speed [*St.-Maurice and Hamza*, 2009].

Eqn. 4.48 is very interesting because it also shows that for type II waves $\Delta\omega_k = kC_s$. Mean ω_k for waves in the $\mathbf{E}_0 \times \mathbf{B}$ direction is a little less than kC_s because there is always a spectral width involved. Still, the final equations explain how the primary waves move with C_s phase velocity and the secondary waves have a spectral width equal to kC_s. So the waves gain energy in the $\mathbf{k}$ direction and give it away in the other directions. On average, for steady-state turbulence, the energy of all modes neither grows nor decays. This has been the most important conclusion from the *Hamza and St-Maurice* [1993] work.

In his work, Sato explained that the mode-coupling with the modes that matter is $\mathbf{k}$ and $\mathbf{k}'$ as shown in Fig. 4.1. An interesting point to note is that the work based on Sudan's approach to mode-coupling allowed secondary modes to be in any direction and with any magnitude. This included for example modes that were all in the original $\mathbf{k}$ direction. However, from energy considerations, the most important modes would have been those considered by Sato, since they take energy from the fastest growing modes and deposit it into fast decaying modes. Earlier simulations by *Oppenheim et al.* [1995] had also found this. So, in the end, there is no contradiction. It is just that Sato focused on the most important part of the coupling, as it turns out.

4.3 Intermittency:

Sato's work and other mode-coupling theories have been done using plane waves. However, we do not need a plane wave description as much as we need individual elongated structures to describe the physics at hand, as shown in the rest of this thesis where the concept of "intermittency" will

be exploited. This can be done through a study of the electric field, currents and the anomalous properties within the sub-structures being in place, as I now explain.

To discuss this important issue, Fig. 4.4, which has already been presented in Chapter 3, has been brought back. It shows from observations that a different way to look at the turbulence, at least in the E region, is to consider the fact that it is intermittent. This approach is based on the fact that the unstable plasma is made of larger amplitude structures that are far from filling the whole plasma, particularly at large amplitude. This was illustrated by CW (continuous wave) experiments at 50 MHz that were reported by *Prikryl et al.* [1990]. Furthermore, it was found not only that the radar detected individual structures but also that they evolved dramatically on a time scale of the order of 0.5 s. When structures were first detectable, their phase velocities could be very high compared to the ion acoustic speed. As time progressed, however, the amplitude increased, but at the same time, the phase velocity went down. When the phase velocity became comparable to the ion acoustic speed, the amplitude was at its greatest and was considerably larger than when first observed [*Drexler et al.*, 2002]. An interesting point from the observation was that the structures also quickly decayed after having reached the ion-acoustic speed.

The CW observations drove *St.-Maurice and Hamza* [2001] to work on a nonlinear analysis that would be based on individual structures from the onset, which meant that a Fourier analysis (plane wave description) was not used to describe the initial structures. It was assumed instead that individual ('intermittent') structures had a finite elongation to start with. The authors then considered what would happen if the elongated structures could be described at least roughly by a uniform electric field inside of them (the elongation along the ambient electric field direction allowed the structures to grow, as inferred from linear theory).

Under the above assumptions, the electric field of the structures was then shown to rotate while its magnitude went down as the amplitude of the intermittent structures grew. This was, in fact, a very similar idea to the one proposed by *Sato* [1971] and which was described in the previous subsection. However, in the *St.-Maurice and Hamza* [2001] case, the work was used for 1-m to 10-m scale structures. The logic was nevertheless the same: the initial polarization field in the $\mathbf{E}_0 \times \mathbf{B}$ was making the electrons drift in the $\mathbf{E}_0$ direction, and a new polarization field was then introduced in the $\mathbf{E}_0$ direction under the assumption that electron currents were to be canceled by the background ions.

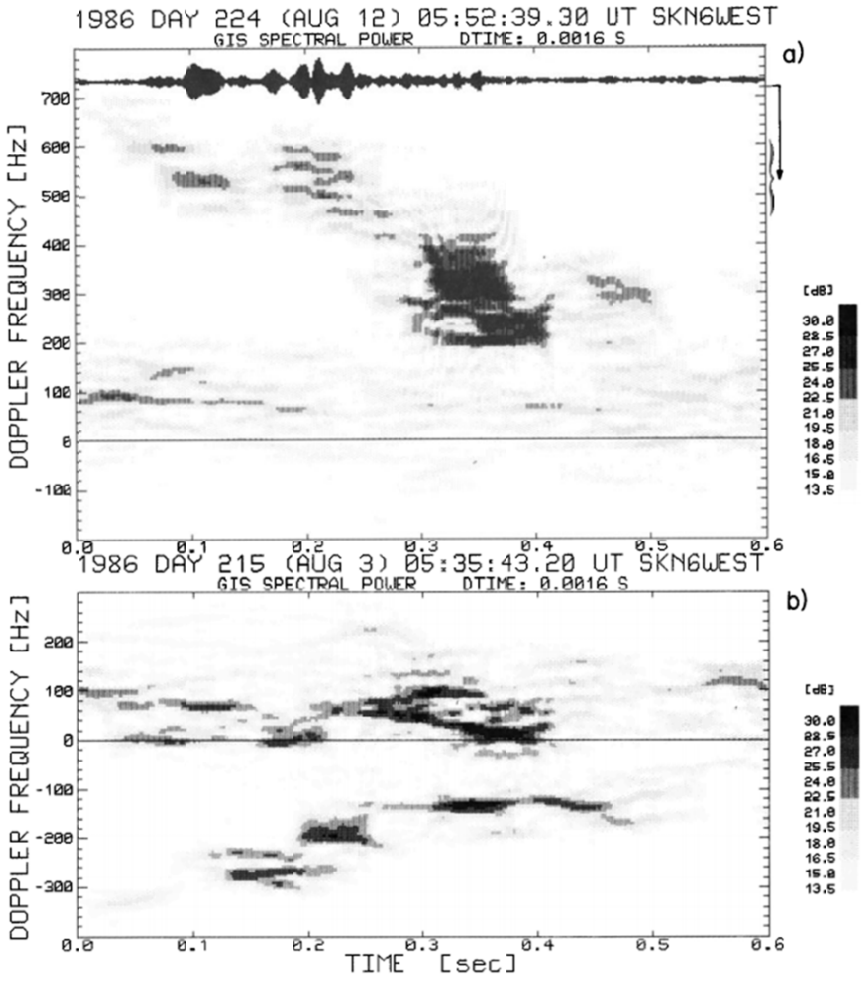

Figure 4.4: The 64-ms window FFT power spectra for two separate events during which the turbulent plasma was observed by a 50 MHz radar used during the CW experiments. The largest amplitude was found near the ion acoustic speed, while the smallest amplitude had a much larger Doppler shift that may well have been comparable to the plasma $\mathbf{E} \times \mathbf{B}$ [*Prikryl et al.*, 1990].

Thus if we have $\delta\mathbf{E}$ that arises from the polarization field created by electrons, the resultant electron Hall polarization produces total electric field ($\mathbf{E_t}$) inside the structure. According to the geometry, the $\delta\mathbf{E}$ has to be perpendicular to $\mathbf{E_t}$ with the condition $\mathbf{E_t} = \mathbf{E_0} + \delta\mathbf{E}$. We also note that $\mathbf{E_0}$ is the ambient electric field. Considering currents being non-divergent along the direction which is perpendicular along the long axis of the elongated structure, introduces the following result:

$$\mathbf{E_b} = \frac{\mathbf{E_0} + (\alpha\delta n_b/n_b)\mathbf{E_0} \times \hat{\mathbf{b}}}{1 + (\alpha\delta n_b/n_b)^2} \tag{4.50}$$

where $\alpha = (\nu_i/\Omega_i)/(1+\Psi)$ as already defined earlier in the present chapter. Eqn. 4.50 indicates that there is considerable amount of rotation and therefore a reduction in the overall $\mathbf{E_0} \times \mathbf{B}$ drift when $\alpha\delta n_b/n_b$ is of the order of 1. Therefore using 2D intermittent approach, it was found that once a large plane wave breaks down into sub-structures, the sub-structures undergo rotation as they grow. These structures eventually slow down to match with the background medium [*St.-Maurice and Hamza*, 2009]. These features are also taken into account while the results of the mode-coupling approach were analyzed by *Otani and Oppenheim* [1998] and *Otani and Oppenheim* [2006] using numerical simulations in 2D. The two approaches mode-coupling and intermittency are similar. The advantage of the approach of intermittency is that we could move from 2D to 3D while describing the evolution of the non-linear structures. Let's discuss the evolution of 2D to 3D through an example here. In 2D, a structure becomes quasi-stable when a structure grows to an amplitude in a way that its phase velocity is approximately equal to the threshold speed [*St.-Maurice and Hamza*, 2009]. Therefore, the structure neither grows or decays. While analyzing the problem in 3D, the same structures involve a rotation-rate that is altitude-dependent. As a result of this, the shears are introduced and thereby involving the non-local effects. Very similar effects have been discussed by *Drexler* [2005] in deca-meter situations.

4.4 Conclusions:

The work on mode-coupling has evolved to show that the most important modes in the coupling are actually perpendicular to one another, with a small wave vector along the long axis of the structures, namely, along the ambient electric field direction. This means that, inside the structures,

the electric field rotates with one component anti-parallel to the ambient electric field direction. In turn, this implies that the total electric field is going down. This agrees with the observations showing that the strongest structures move at the threshold speed along the $\mathbf{E}_0 \times \mathbf{B}$ direction. This explains why type I structures move at the ion-acoustic speed, which is the threshold speed. By the same token, type II structures are, from a mode-coupling perspective, of smaller amplitude, and more quickly decaying, as they come from viewing the structures into their long axis. They decay through ordinary diffusion once they are produced. This is in contrast to the type I structures which are subject to relatively slow growth and decay.

When mode-coupling theories evolved to become an intermittency theory, it was recognized that the plasma is not likely to be populated by large amplitude structures. Instead of a steady state statistical computation of the spectra, the theory addressed the evolution of individual structures. It showed that, structure by structure, the field rotates and decreases inside a structure until threshold conditions are achieved. It produced an analytical approximation for the maximum amplitude of each structure which agreed with the mode-coupling approach that had been proposed by *Sato* [1971].

The parallel E field plays a vital role in the decay of the structures because it increases monotonically with time, the frequency being a function of space (altitude). Once it becomes large enough, this parallel electric field leads to a decay of the structures while it heats the electrons. Therefore a model was proposed by *St.-Maurice and Hamza* [2001] wherein intermittency in 2D describes the quick evolution of the structures while non-local effects along the magnetic field direction imply that the structures decay once they have reached a maximum amplitude associated with a motion at the ion-acoustic speed. This parallel electric field evolution is enhanced by the fact that there is a rotation of the electric field vector in the plane perpendicular to the magnetic field which depends on altitude. This introduces shears and therefore becomes important for an understanding of the final evolution of the structures, which, as seen by the CW observations, vanish after having reached a maximum amplitude with a phase velocity of the order of the ion-acoustic speed.

In what follows in Chapter 5, I will construct a new intermittency theory rooted in the earlier work by *St.-Maurice and Hamza* [2001]. I will propose a new expression and a different view of the saturation, given that in the earlier work the long axis of the structures was assumed to rotate, though it has become clear that in a nonlinear situation, this is not what happens. My focus will

be on an understanding of the physics of the saturation and its implication for the average transport properties of the E region plasma.

Chapter 5

A new theory for the saturation of E field inside a structure and consequences

5.1 Electric Field Inside the Blob

I now present a new theory of the nonlinear evolution of Farley-Buneman (FB) waves. Instead of Fourier analyzing in space and time and getting caught in complex mode-coupling calculations I am following the approach initially taken by *Sato* [1973] and *St.-Maurice and Hamza* [2001]. This approach was discussed in the previous chapter. I will present my work in a way that facilitates the comparison between the observed data and the theoretical calculations. The calculation will start with the diffusion-like operator that was introduced in Chapter 1, where the linear theory was introduced. I will show that as the amplitude grows, the net electric field inside individual structures actually decreases through polarization effects. The polarization E field responsible for this will be shown to rotate while its strength goes down while the amplitude increases.

An essential difference with the intermittency theory presented in *St.-Maurice and Hamza* [2001] will be that instead of rotating elongated density structures, I will only rotate their electric field without changing the long axis orientation. This will require a different condition for the currents passing through the structures. This will introduce an important correction to the past results meaning that the net electric field inside structures that brings them to threshold velocity conditions will take a different form. This means in turn that I will be producing new expressions for the anomalous currents and conductivities as well as the average electric field in the system, not to mention new values for the density and electric field fluctuations as functions of E region altitude.

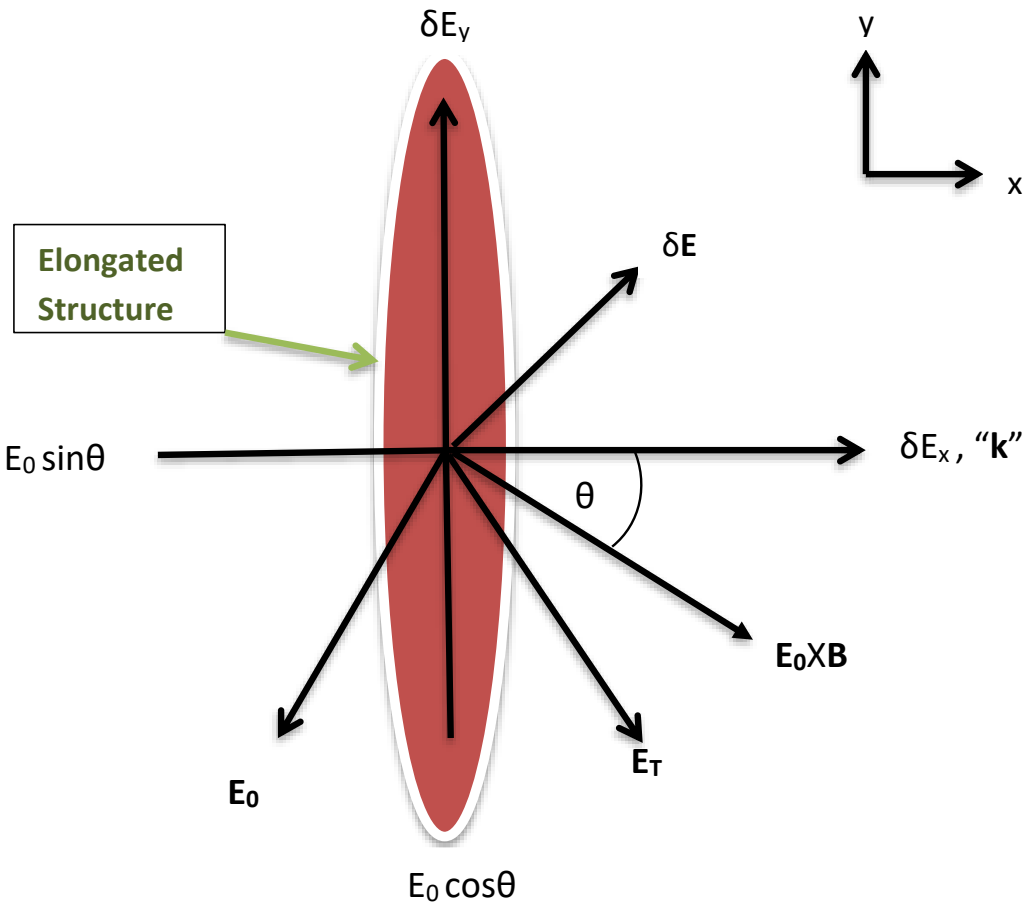

Figure 5.1: 'Model blob': the long axis of the structure is along y. The angle θ is the classical "flow angle". The dominant wave vector "**k**" that would be associated with the linear theory is perpendicular to long axis and **B** is along the z-direction coming out of the plane.

5.2 Presenting the new nonlinear evolution mechanism

As with previous work, with the approach used here, to leading order, the perturbed electric field and the perturbed density will not involve pressure fluctuations. The model is based on the cartoon shown in Fig. 5.1. The long axis of the structure is along y, and the background electric field $\mathbf{E}_0$ is perpendicular to **B**. The flow angle θ is between the $\mathbf{E}_0 \times \mathbf{B}$ drift and the equivalent **k** direction (i.e., the direction perpendicular to the long axis). That angle is equivalently the angle between $\mathbf{E}_0$ and the long axis of the density structure. The structures will be called blobs if they correspond to density enhancements and holes if they are associated with local depressions. Polarization fields

will develop in both types of objects in response to currents driven initially by electron drifts.

Nonlinearities are introduced through a change in the electric field seen inside "blobs" and "holes". The field inside the structure decreases while rotating at the same time. This modifies the velocity of a structure and consequently its growth rate or, equivalently, the rate of molecular diffusion or antidiffusion through a modification of the phase velocity. This means that the diffusion coefficients is in effect a function of the density fluctuation. The net result is that a blob (or hole) reaches a finite amplitude governed by the fact that when it finally slows to a speed perpendicualr to the long axis that is close to the ion-acoustic speed (or more generally the instability threshold speed) of the medium. At that point its amplitude stops growing [*St.-Maurice and Hamza*, 2001]. The amplitude from then on has to decay because, as discussed in Chapter 3, the aspect angle will continue to grow and cause the structures to decay while giving their energy to electrons through their heating through the growing parallel electric fields.

5.3 Discussion of evolution Equation

Recall first the evolution equation that was derived while discussing linear theory in Chapter 3:

$$\Big[\frac{\partial}{\partial t} + \frac{\mathbf{V}}{1+\psi}\cdot\nabla\Big]\frac{\delta n}{n_0} = -\frac{\psi}{\nu_i(1+\psi)}\Big[\frac{\partial^2}{\partial t^2}\frac{\delta n}{n_0} - C_s^2\nabla^2\frac{\delta n}{n_0}\Big] \tag{5.1}$$

where $C_s^2 = (\Omega_i/\Omega_e)C_e^2 + C_i^2 = [k(T_e+T_i)]/m_i$ is the square of ion-acoustic speed of the plasma and $\Psi = \Psi_0\Big(1 + \frac{k_\parallel^2\Omega_e^2}{k_\perp^2\nu_e^2}\Big)$ and $\Psi_0 = \frac{\nu_e\nu_i}{\Omega_e\Omega_i}$ with $\Psi_0 << 1$. Revisiting this equation is very important here. Consider that even when at first the RHS is not zero, its multiplicaion by $\Psi << 1$ means that that the left-hand-side has to be very close to zero. In that case, $\Big(\frac{\partial}{\partial t} + \frac{\mathbf{V}\cdot\nabla}{1+\Psi}\Big) \approx 0$ meaning that the structure is simply advected through the plasma at a velocity $\mathbf{V}/(1+\Psi)$. This stated, when the plasma is unstable to FB waves the RHS makes the amplitude of the advected structure grow. The point of the present thesis is to show that the amplitude growth introduces a reduction in $\mathbf{V}$. This then slows down the growth until a point is reached where both sides of the equation are exactly zero so that the structure then stops evolving. This stated, the aspect angle evolution discussed above means that Ψ keeps increasing, which the makes the amplitude decay until the structure disappears.

The remaining question is: when can the two terms on the RHS be equal? The answer is, that

we can make **V** small as δn increases so that the convective speed and with it the second time derivative goes down. Equating $C_s^2 = \frac{V^2}{(1+\Psi)^2}$ we get V. If V is greater than C_s we have growth and if V is less than C_s we have decay. There are two ways for V to go down. We can either increase Ψ or we can decrease **E**. Ignoring the changes in Ψ through the growth of $k_{\|}/k_{\perp}$ under the assumption that the growth due to antidiffusion is much faster, we focus on the changes in the electric field inside a structure, which slows its drift down quickly [*Hamza and St-Maurice*, 1993]. We now revisit this notion through the new theory presented here.

5.4 Electric field rotation in the absence of a rotation of the elongated structure

The motivation to work with the rotation of the electric field instead of working with a rotation of the elongated structure itself is based on the work of *Hysell and Drexler* [2006]. These authors have shown that elongated plasma blobs with a uniform density will undergo a rotation of the ambient electric field inside their bodies. That rotation is neither that of a pure conductor or of a pure dielectric. The authors provided several examples based on analytical computations.

Fig. 5.2(a) shows the equipotentials close to an elliptical irregularity oriented in such a way that the background electric field is parallel to its minor axis. It was found that the field inside the structure is at a different angle than the long axis. Through this, the authors have pointed out that the electric fields rotated inside the structures. This is the main idea of my work where I decided to study the rotation of electric fields inside the structure instead of the rotation of the structure itself in order to explain the growth and the decay of elongated small-scale structures.

In Fig. 5.2(a) the equipotentials outside the irregularity region are nearly parallel to its surface, and the flow around the structure is almost uninterrupted. In Fig. 5.2(b), which is or more interest for the present thesis, the same elliptical structure is oriented with its major axis parallel to the background electric field. In this case, the flow around the irregularity is drastically interrupted, and the electric field inside the elongated structure undergoes a drastic rotationis. *Hysell and Drexler* [2006] also show the variation in the amplitude of the electric field with respect to an angle between the major axis and the background electric field.

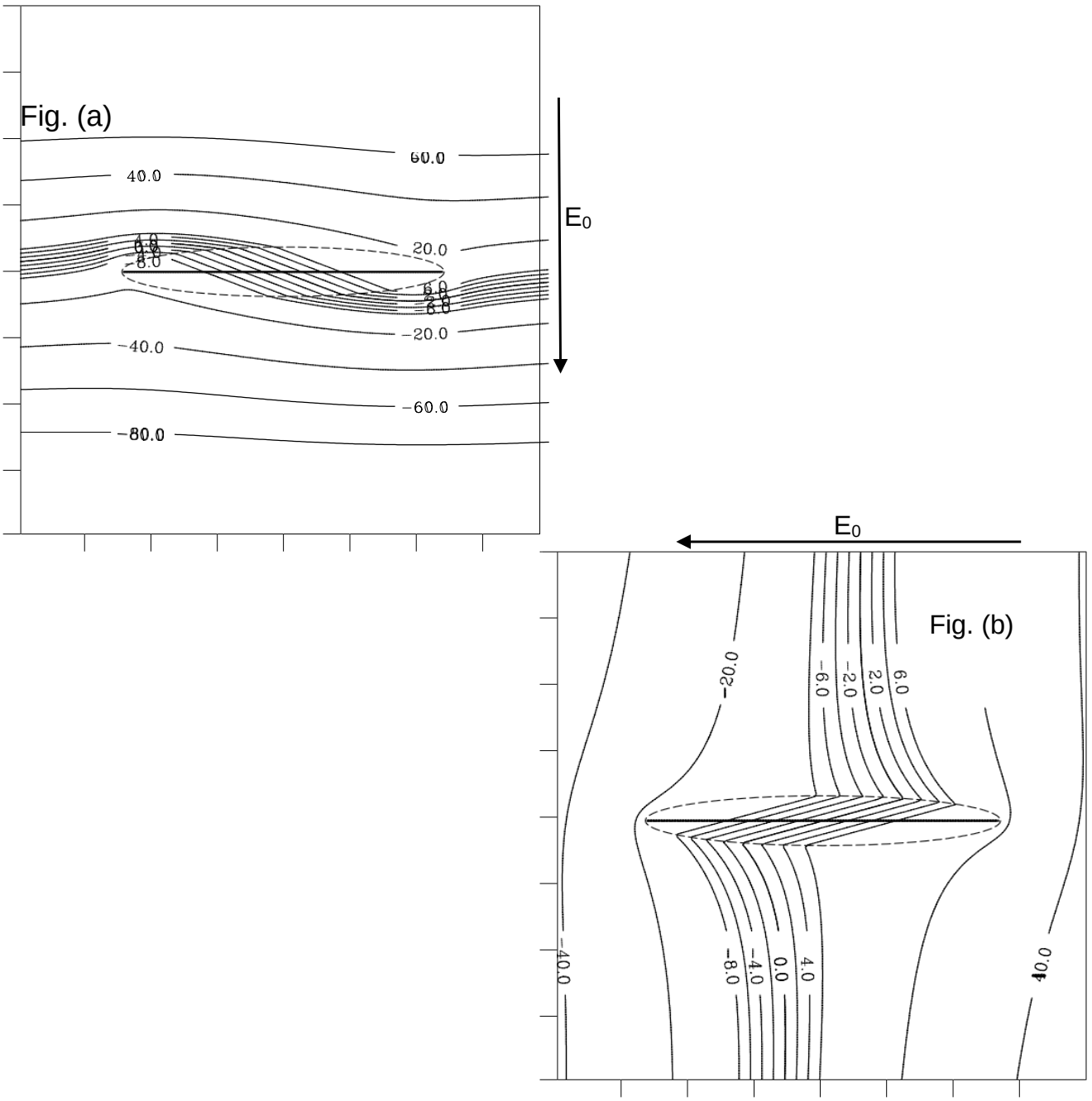

Figure 5.2: Analytical computation of equipotentials in a 2-dimensional plane perpendicular to the magnetic field. In case (a), the elongation is perpendicular to the ambient electric field. In case (b) the elongation is parallel to the ambient electric field direction. From *Hysell and Drexler* [2006].

5.5 Currents and Electric fields inside individual blobs or holes

The net current inside blob or holes comes from the sum of Pedersen currents (flowing along the electric field direction) and the Hall currents (flowing in a direction perpendicular to both electric and magnetic fields). This simply means that if σ_P^T and σ_H^T are the total Pedersen and Hall conductivities inside a blob or hole, we can write

$$\mathbf{J} = \sigma_P^T \mathbf{E} + \sigma_H^T \mathbf{E} \times \mathbf{B}/B \tag{5.2}$$

If the total conductivity due to the Pedersen current is represented by σ_P^T, the background conductivity as σ_P^0, and the change in conductivity due to polarization $\delta\sigma_P$, the resultant equation can be represented as,

$$\sigma_P^T = \sigma_P^0 + \delta\sigma_P \tag{5.3}$$

With similar concept, the total Hall conductivity can be defined as,

$$\sigma_H^T = \sigma_H^0 + \delta\sigma_H \tag{5.4}$$

Inside the structures, the $\mathbf{E} \times \mathbf{b}$ drift of electrons is responsible to setup the polarization of the electric field. Let's say the final polarization field inside the blob and the holes is $\delta\mathbf{E}$. Therefore, the total electric field $\mathbf{E}^T$,

$$\mathbf{E}^T = \mathbf{E}_0 + \delta\mathbf{E} \tag{5.5}$$

The next step consists in using the fact that $\nabla \cdot \mathbf{J} = 0$. We take it for granted that the ambient current density $\mathbf{J}_0 = \sigma_P^0 \mathbf{E}_0 + \sigma_H^0 \mathbf{E}_0 \times \mathbf{B}/B$ is divergence-free and need not be considered. The focus will be instead on the divergence of the perturbed currents, namely, on the perturbed current density $\mathbf{J}_{pert}$ inside the blobs or holes. This part of the current is simply described by

$$\mathbf{J}_{pert} = \delta\sigma_P \mathbf{E}_0 + \sigma_P^T \delta\mathbf{E} + \delta\sigma_H \mathbf{E}_0 \times \mathbf{b} + \sigma_H^T \delta\mathbf{E} \times \mathbf{b} \tag{5.6}$$

In setting $\nabla \cdot \mathbf{J}_{pert} = 0$ for an electrostatic situation we must consider that $\nabla \cdot (\delta\mathbf{E} \times \mathbf{b}) = 0$. This means that if there is a y-derivative in the δE_x component (which there has to be near the ends of

the long axis) then we have to include a x-derivative of δE_y. However, if the structure is sufficiently elongated, these contributions are only important near the end points and are simply describing the kinds of fringe electric fields that we have at the end of long plane capacitors. We then break $\mathbf{J}_{pert}$ into two parts as follows:

$$\mathbf{J}_{pert} = \mathbf{J}' + \sigma_H^0 \delta\mathbf{E} \times \mathbf{b} \tag{5.7}$$

where

$$\mathbf{J}' = \delta\sigma_P \mathbf{E}_0 + \sigma_P^T \delta\mathbf{E} + \delta\sigma_H \mathbf{E}_0 \times \mathbf{b} + \delta\sigma_H \delta\mathbf{E} \times \mathbf{b} \tag{5.8}$$

We look for solutions to $\nabla \cdot \mathbf{J}_{pert} = 0$. But the divergence of the second term in Eqn (5.7) is automatically zero. Then, if we integrate through all space around the blob, the perturbation terms in Eqn (5.8) all vanish meaning that $\mathbf{J}'$ itself must be zero while by the same token $\mathbf{J}_{pert} = \sigma_H^0 \delta\mathbf{E} \times \mathbf{b}$.

This is where the present thesis differs from the calculations carried by *St.-Maurice and Hamza* [2001]. In their work *St.-Maurice and Hamza* [2001] tilted the structures and required from the null current divergence that the total current passing across the narrow side of the structures be equal to the current reaching and leaving the structure. Importantly, *St.-Maurice and Hamza* [2001] also required the perturbed electric field in the structure to be perpendicular to the total electric field, itself along the long axis of the cylinder. Currents flowing along the long axis of the structures were not constrained meaning that any current divergence in that direction was never considered even though there had to be edge effects where the curl of the electric field needed to be taken into account. In *St.-Maurice and Hamza* [2001] the only constraint was that the component of the perturbed currents in the direction perpendicular to the long axis had to be zero. Here instead the perturbed electric field cannot be perpendicular to the long axis. However, we still keep a current associated with $\sigma_H^0 \delta\mathbf{E} \times \mathbf{b}$ because once again there are edge effects in association with the finite size of the structures. In *St.-Maurice and Hamza* [2001] this current was in effect given by the same expression in view of the chosen geometry.

5.5.1 Calculations

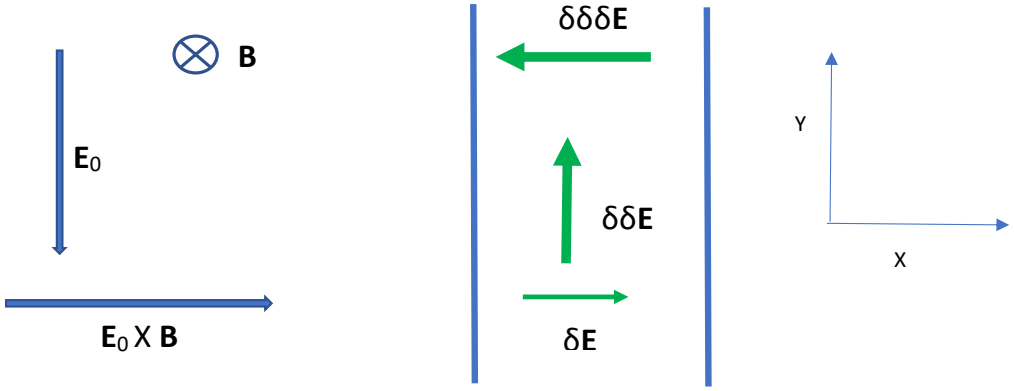

Figure 5.3: Perturbed E field inside the structure is initially in the X direction, and it produces a polarization field due to inhomogeneity in the structure along the long axis. As a result, the polarization field inside the structure rotates.

Working with the assumption that $\mathbf{J}^{'} = 0$, we added the Pedersen and the Hall currents together as follows

$$\sigma_P^T(\mathbf{E}_0 + \delta\mathbf{E}) - \sigma_P{}^0\mathbf{E}_0 + \delta\sigma_H(\mathbf{E}_0 + \delta\mathbf{E}) \times \mathbf{b} = 0 \tag{5.9}$$

Then, using Eqn. 5.5 we get the following:

$$\sigma_P^T\mathbf{E}^T + \delta\sigma_H\mathbf{E}^T \times \mathbf{b} = \sigma_P{}^0\mathbf{E}_0 \tag{5.10}$$

Taking the cross-product of Eqn. 5.10 with $\mathbf{b}$ we get,

$$\sigma_p^T\mathbf{E}^T \times \mathbf{b} - \delta\sigma_H\mathbf{E}^T = \sigma_P{}^0\mathbf{E}_0 \times \mathbf{b} \tag{5.11}$$

$$\mathbf{E}^T \times \mathbf{b} = \frac{\delta\sigma_H}{\sigma_P^T}\mathbf{E}^T + \frac{\sigma_P{}^0}{\sigma_P^T}\mathbf{E}_0 \times \mathbf{b} \tag{5.12}$$

Therefore, we end up with

$$\sigma_P^T \mathbf{E}^T + \frac{\delta\sigma_H^2}{\sigma_P^T}\mathbf{E}^T + \delta\sigma_H \frac{{\sigma_P}^0}{\sigma_P^T}\mathbf{E}_0 \times \mathbf{b} = {\sigma_P}^0 \mathbf{E}_0 \tag{5.13}$$

$$\sigma_P^T \left(1 + \frac{\delta\sigma_H^2}{\sigma_H^{T2}} \frac{\sigma_H^{T2}}{\sigma_P^{T2}}\right)\mathbf{E}^T = {\sigma_P}^0 \mathbf{E}_0 - \delta\sigma_H \frac{{\sigma_P}^0}{\sigma_P^T}\mathbf{E}_0 \times \mathbf{b} \tag{5.14}$$

Therefore we have the following:

$$\mathbf{E}^T = \frac{{\sigma_P}^0/\sigma_P^T \mathbf{E}_0 - \frac{\delta\sigma_H}{\sigma_H^T}\frac{\sigma_H^T}{\sigma_P^T}\frac{{\sigma_P}^0}{\sigma_P^T}\mathbf{E}_0 \times \mathbf{b}}{1 + \frac{{\delta\sigma_H}^2}{{\sigma_H^T}^2}\frac{{\sigma_H^T}^2}{{\sigma_P^T}^2}} \tag{5.15}$$

$$\mathbf{E}^T = \frac{n_0}{n_b}\frac{\mathbf{E}_0 + \alpha\frac{\delta n_b}{n_b}\mathbf{E}_0 \times \mathbf{b}}{1 + \alpha^2(\frac{\delta n_b}{n_b})^2} \tag{5.16}$$

with $\alpha = (\nu_i/\Omega_i)/(1 + \Psi)$. We have used

$$\begin{aligned} \frac{\sigma_H}{\sigma_P} = \frac{\delta\sigma_H}{\delta\sigma_P} &= -\alpha \\ \frac{{\sigma_P}^0}{\sigma_P^T} &= \frac{n_0}{n_b} \\ \frac{\delta\sigma_H}{\sigma_H} &= \frac{\delta n_b}{n_b} \end{aligned} \tag{5.17}$$

Note that the minus sign in the conductivity ratio is due to the Hall currents carried by electrons being in the $-\mathbf{E} \times \mathbf{b}$ direction while we had used the convection that the Hall currents were given by $+\sigma_H \mathbf{E} \times \mathbf{b}$.

Finally, we can write

$$\frac{n_0}{n_b} = \frac{n_0 + \delta n_b}{n_b} - \frac{\delta n_b}{n_b} \sim 1 - \frac{\delta n_b}{n_b} \tag{5.18}$$

to arrive at

$$\mathbf{E}^T = (1 - \frac{\delta n_b}{n_b})\frac{\mathbf{E}_0 + \alpha\frac{\delta n_b}{n_b}\mathbf{E}_0 \times \mathbf{b}}{1 + \alpha^2(\frac{\delta n_b}{n_b})^2} \tag{5.19}$$

Eqn. 5.19 verifies that if there is no perturbation in the density, then the electric field is equal to the background electric field $\mathbf{E}_0$. This result is independent of the orientation of the blob except that

$\frac{\delta n_b}{n_b}$ will change with its orientation and be larger for a more unstable geometry.

For an explicit handling of the angle between the long axis of the density structures and the electric field direction we simply have to consider the angle between **k** (the direction of the narrow axis) and $\mathbf{E}_0$ or $\mathbf{E}_0 \times \mathbf{b}$. We need to be aware that $\mathbf{E}^T$ is total electric field inside the blob. To study the growth or decay of the structures, we require the drift velocity along the **k** (or x-) direction to be approximately close to $C_s(1 + \Psi)$. However, the drift is $\mathbf{E}^T \times \mathbf{b}$ and therefore

$$\mathbf{V} = \frac{\frac{n_0}{n_b}\left[\frac{\mathbf{E}_0 \times \mathbf{b}}{B} - \frac{\alpha \frac{\delta n}{n} \mathbf{E}_0}{B}\right]}{1 + \alpha^2 \left(\frac{\delta n}{n}\right)^2} \tag{5.20}$$

We want $V_x = C_s(1 + \Psi)$: the structure is moving along x with a speed close to C_s when the density amplitude reaches its maximum (so the growth rate becomes nearly zero). However, from the last equation we must have

$$V_y = \frac{n_0/n_b\left[\frac{\mathbf{E}_{0x} \times \mathbf{b}}{B} \cdot \hat{\mathbf{y}} - \frac{\alpha \frac{\delta n}{n} E_{0y}}{B}\right]}{1 + \alpha^2 \left(\frac{\delta n}{n}\right)^2} \tag{5.21}$$

$$V_x = \frac{n_0/n_b\left[-\frac{E_{0y}}{B} - \alpha \frac{\delta n}{n} \frac{E_{0x}}{B}\right]}{1 + \alpha^2 \left(\frac{\delta n}{n}\right)^2} \tag{5.22}$$

If θ is the angle between $\mathbf{E}_0$ and the long axis of the object (blob or hole) and if we use the geometry presented in Fig 5.1 we have

$$-E_{0y} = |E_0| \cos\theta \tag{5.23}$$

$$E_{0x} = -|E_0| \sin\theta \tag{5.24}$$

Therefore

$$V_x = \frac{n_0/n_b}{1 + \alpha^2 \left(\frac{\delta n}{n}\right)^2} \frac{E_0}{B}\left[\cos\theta + \alpha \frac{\delta n}{n} \sin\theta\right] = C_s(1 + \Psi) \tag{5.25}$$

Defining $\tan(\phi) = \alpha \frac{\delta n}{n}$, we finally obtain from the $\cos(\theta - \Phi)$ applied to the previous equation the

final result

$$V_x = \frac{n_0/n_b}{\sqrt{1+\alpha^2\left(\frac{\delta n}{n}\right)^2}}\frac{E_0}{B}\cos(\theta-\phi) \tag{5.26}$$

We find similar expressions for V_y, namely

$$V_y = \frac{n_0/n_b}{1+\alpha^2\left(\frac{\delta n}{n}\right)^2}\frac{E_0}{B}\left[\sin\theta - \alpha\frac{\delta n}{n}\cos\theta\right] \tag{5.27}$$

so that from Eq. 5.20, we end up with

$$V_y = \frac{n_0/n_b}{\sqrt{1+\alpha^2\left(\frac{\delta n}{n}\right)^2}}\frac{E_0}{B}\sin(\theta-\phi) \tag{5.28}$$

5.5.2 Component by Component Derivation

If we refer to Fig. 5.1 and redo the derivation considering the components of the electric field, then we start with the following equations to find the electric field along each direction.

$$\delta J_x = \delta\sigma_P(\delta E_x - |E_0|\sin\theta) + \sigma_P^0\delta E_x + \delta\sigma_H(\delta E_y - |E_0|\cos\theta) + \sigma_H^0\delta E_y \tag{5.29}$$

$$\delta J_y = -\delta\sigma_P(|E_0|\cos\theta - \delta E_y) - \sigma_P^0\delta E_y - \delta\sigma_H(\delta E_x - |E_0|\sin\theta) - \sigma_H^0\delta E_x \tag{5.30}$$

Based on $\nabla\times\delta\mathbf{E} = 0$ as explained earlier we have

$$\delta\sigma_P(\delta E_x - |E_0|\sin\theta) + \sigma_P^0\delta E_x + \delta\sigma_H(\delta E_y - |E_0|\cos\theta) = 0 \tag{5.31}$$

$$-\delta\sigma_P(|E_0|\cos\theta - \delta E_y) - \sigma_P^0\delta E_y - \delta\sigma_H(\delta E_x - |E_0|\sin\theta) = 0 \tag{5.32}$$

Defining

$$\begin{aligned}(\delta E_x - |E_0|\sin\theta) &= E_x^{tot}\\ (\delta E_y - |E_0|\cos\theta) &= E_y^{tot}\end{aligned} \tag{5.33}$$

we have from the above

$$\delta\sigma_P E_x^{tot} + \sigma_P^0 \delta E_x + \delta\sigma_H E_y^{tot} = 0 \tag{5.34}$$

$$\delta\sigma_P E_y^{tot} - \sigma_P^0 \delta E_y - \delta\sigma_H E_x^{tot} = 0 \tag{5.35}$$

From Eqn. 5.34 we have

$$\delta\sigma_P E_x^{tot} + \sigma_P^0(\delta E_x - |E_0| \sin\theta) + \sigma_P^0 |E_0| \sin\theta + \delta\sigma_H E_y^{tot} = 0 \tag{5.36}$$

If $\sigma_P^T = \sigma_P^0 + \delta\sigma_P$, then we have

$$\sigma_P^T E_x^{tot} + \sigma_P^0 |E_0| \sin\theta + \delta\sigma_H E_y^{tot} = 0 \tag{5.37}$$

and

$$\delta\sigma_P E_y^{tot} - \sigma_P^0(\delta E_y - |E_0| \cos\theta) - \sigma_P^0 |E_0| \cos\theta - \delta\sigma_H E_x^{tot} = 0 \tag{5.38}$$

If ${\sigma_H}^T = \sigma_H^0 + \delta\sigma_H$, then we have

$$\sigma_P^T E_y^{tot} + \sigma_P^0 |E_0| \sin\theta - \delta\sigma_H E_x^{tot} = 0 \tag{5.39}$$

From Eqn. 5.37 we get

$$E_x^{tot} = \frac{-\sigma_P^0 |E_0| \sin\theta - \delta\sigma_H E_y^{tot}}{\sigma_P^T} \tag{5.40}$$

Using Eqn. 5.40 in Eqn. 5.39 we arrive at

$$\sigma_P^T E_y^{tot} - \sigma_P^0 |E_0| \cos\theta - \delta\sigma_H \Big(- \frac{\sigma_P^0 |E_0| \sin\theta - \delta\sigma_H E_y^{tot}}{\sigma_P^T} \Big) = 0 \tag{5.41}$$

$$E_y^{tot} \sigma_P^T \Big(1 + \frac{\delta{\sigma_H}^2}{\sigma_P^{T2}} \Big) = \sigma_P^0 |E_0| \Big(\cos\theta - \frac{\delta\sigma_H}{\sigma_P^T} \sin\theta \Big) \tag{5.42}$$

Recalling that

$$\frac{\sigma_P^0}{\sigma_P^T} = \frac{n_0 + \delta n}{n_0 + \delta n} - \frac{\delta n}{n_0 + \delta n} = 1 - \frac{\delta n}{n} \tag{5.43}$$

$$\frac{\delta\sigma_H}{\sigma_P^T} = \frac{\delta\sigma_H}{\sigma_H^T} \frac{\sigma_H^T}{\sigma_P^T} = -\frac{\delta n}{n} \alpha \tag{5.44}$$

we finally get, like before

$$E_y^{tot} = \frac{(1 - \delta n/n)E_0(\cos\theta + \alpha\frac{\delta n}{n}\sin\theta)}{1 + \alpha^2\delta n^2/n^2} \tag{5.45}$$

and

$$E_x^{tot} = \frac{(1 - \delta n/n)E_0(-\sin\theta + \alpha\frac{\delta n}{n}\cos\theta)}{1 + \alpha^2\delta n^2/n^2} \tag{5.46}$$

5.5.3 Computation of the maximum density fluctuation level

The total electric field in the structures has to be given by

$$|E^T| = \sqrt{E_x^{tot2} + E_y^{tot2}} = \frac{|E_0|(1 - \delta n/n)}{\sqrt{(1 + \alpha^2\delta n^2/n^2)}} \tag{5.47}$$

with $\alpha = (\nu_i/\Omega_i)/(1 + \Psi)$. At maximum amplitude we have $V_x \approx C_s(1 + \psi)$. Using Eqn 5.25 and defining D as

$$D = \frac{|E_0|/B}{C_s(1 + \psi)} > 1 \tag{5.48}$$

we would seem to have all we need to solve numerically for $\delta n/n$. However, this would not be quite right because the instability is actually seen in the ion frame of reference. So, the parameter E_0/B should be replaced by $|\mathbf{V}_e - \mathbf{V}_i|$. As seen and demonstrated in Chapter 3, the solution to the ion and electron momentum equations would then change D to the following

$$D = \frac{|E_0|/B}{C_s(1 + \psi)}\frac{\nu_i/\Omega_i}{\sqrt{1 + \nu_i^2/\Omega_i^2}} \tag{5.49}$$

Using this value for D we can proceed to find that the maximum perturbed density value, which is given by the solution to the equation

$$\Big[\frac{E_0/B}{C_s(1 + \psi)}\Big]\frac{(1 - \delta n/n)}{\sqrt{(1 + \alpha^2\delta n^2/n^2)}}\cos(\theta - \phi) = 1 \tag{5.50}$$

with $\tan\phi = \alpha\delta n/n$. The flow angle θ could be anything that prodcues growth, including zero. The last equation can be written in the form

$$D\cos(\theta-\phi)(1-\delta n/n) = \sqrt{(1+\alpha^2\delta n^2/n^2)} \tag{5.51}$$

Taking the square of Eqn. 5.51 we get,

$$D^2\cos^2(\theta-\phi)(1-\delta n/n)^2 = (1+\alpha^2\delta n^2/n^2) \tag{5.52}$$

We now have to solve for $X \equiv \delta n/n$, namely for the combined system of nonlinear equations given by

$$\begin{aligned} D^2\cos^2(\theta-\phi)(1-2X+X^2) - (1+\alpha^2X^2) = 0 \\ \phi = \arctan(\alpha\delta n/n) = \arctan(\alpha X) \end{aligned} \tag{5.53}$$

The solution to these equations depends strongly on altitude through α and of course on the electric field E_0 and on the threshold velocity, assumed here to be the ion-acoustic speed in the absence of gradient-drift contributions to the instability. The parameter α depends mostly on the ion collision frequency, but there is also an electron collision frequency contribution through Ψ. The collision frequencies were extracted from the values presented by *Schunk and Nagy* [2009] using the MSIS neutral density model that is widely available on the internet. A calculation of the ion and electron temperatures were needed in order to extract the ion acoustic speed. The ion temperature depends on frictional heating when the electric field accelerates the ions through the neutral gas. The expressions are well known and presented for example in the comprehensive paper by *St.-Maurice and Chau* [2016]. For the electron temperature a new empirical model produced by St-Maurice (private communication) was used, based on a collection of observations. The model produces electron temperatures that differ from the neutral temperature above 40 mV/m electric fields. When that electric field value is exceeded, a linear relation between $T_e - T_n$ and the electric field is used. This is done for 10 different altitudes, all of which have a different slope. The model

is extremely simple to implement since it is simply given by

$$T_e = T_{e0} + S(E_0/B - 800) \tag{5.54}$$

The coefficients that are used for this model are presented in Table 5.1. The model fits all existing observations rather well (St-Maurice, private communication). A more sophisticated model was also constructed by *Chau and St.-Maurice* [2016]. It is far more complicated to implement and offers a smoother behavior as a function of altitude. But in the end it produces essentially the same numbers.

Altitude(km)	Te_0	Slope
101.0	200	0.424
103.7	200	0.848
106.3	200	1.150
108.9	250	1.364
111.6	300	1.520
114.2	400	1.273
116.9	500	0.727
119.5	500	0.670

Table 5.1

The parameter D is important for the calculations of the density fluctuations and is therefore shown in Fig. 5.4 in the form of various altitude profiles that change with the electric field E_0 or, equivalently, the value of E_0/B. The parameter D can be seen to increase steadily with decreasing altitude mostly because the ion-acoustic speed decreases markedly with decreasing altitude while Ψ remains smaller than 0.1 even at 100 km.

From the model values of D I calculated $\delta n/n$ from Eqn (5.53) for $\theta = 0$, which should be the most unstable direction, meaning that the calculations are providing an estimate for the largest amplitudes possible. The results from the calculations are presented for different electric field values in Fig. 5.5. It should be kept in mind before comparing the calculations that that there is a difference between maximum amplitudes and average or rms magnitudes of the perturbed densities. Only a fraction of a given volume is populated by the largest amplitude structures. That fraction corresponds to the packing ratio discussed below and it should be of order 0.2 or 0.3. Thus a 30% maximum amplitude would actually correspond to a 6 to 9% broadband density level.

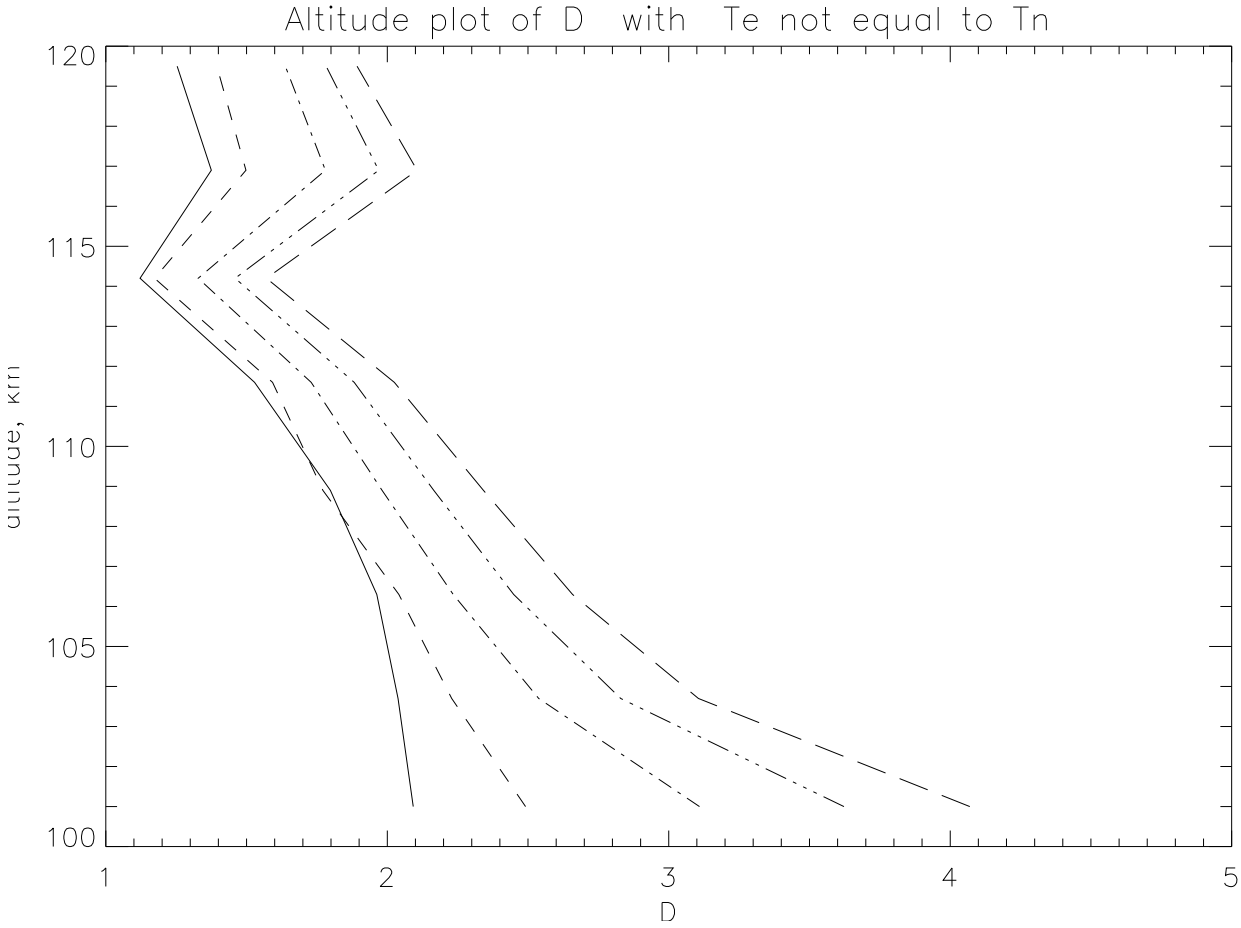

Figure 5.4: Altitude variation of the parameter D defined by equation 5.49. The various profiles are for different values of E_0/B being, from left to right, equal to 750, 1000, 1500, 2000, and 2500 m/s respectively.

Comparing Fig 5.5 with observations of the kind that were presented in Chapter 2 with this in mind we find a reasonable agreement between profiles, although the calculations produce peak values that appear to be at too high an altitude. The bottom portion of the plot in particular is found lacking in the calculations. However we need to keep in mind that the lower regions also exhibit lower frequencies in rocket observations. In fact that region is prone to the presence of Gradient-Drift instabilities [*Haldoupis et al.*, 2000]. This means that we should be able to use a lower threshold speed [*St.-Maurice et al.*, 1994b] which in turn would mean larger density fluctuations for the calculations.

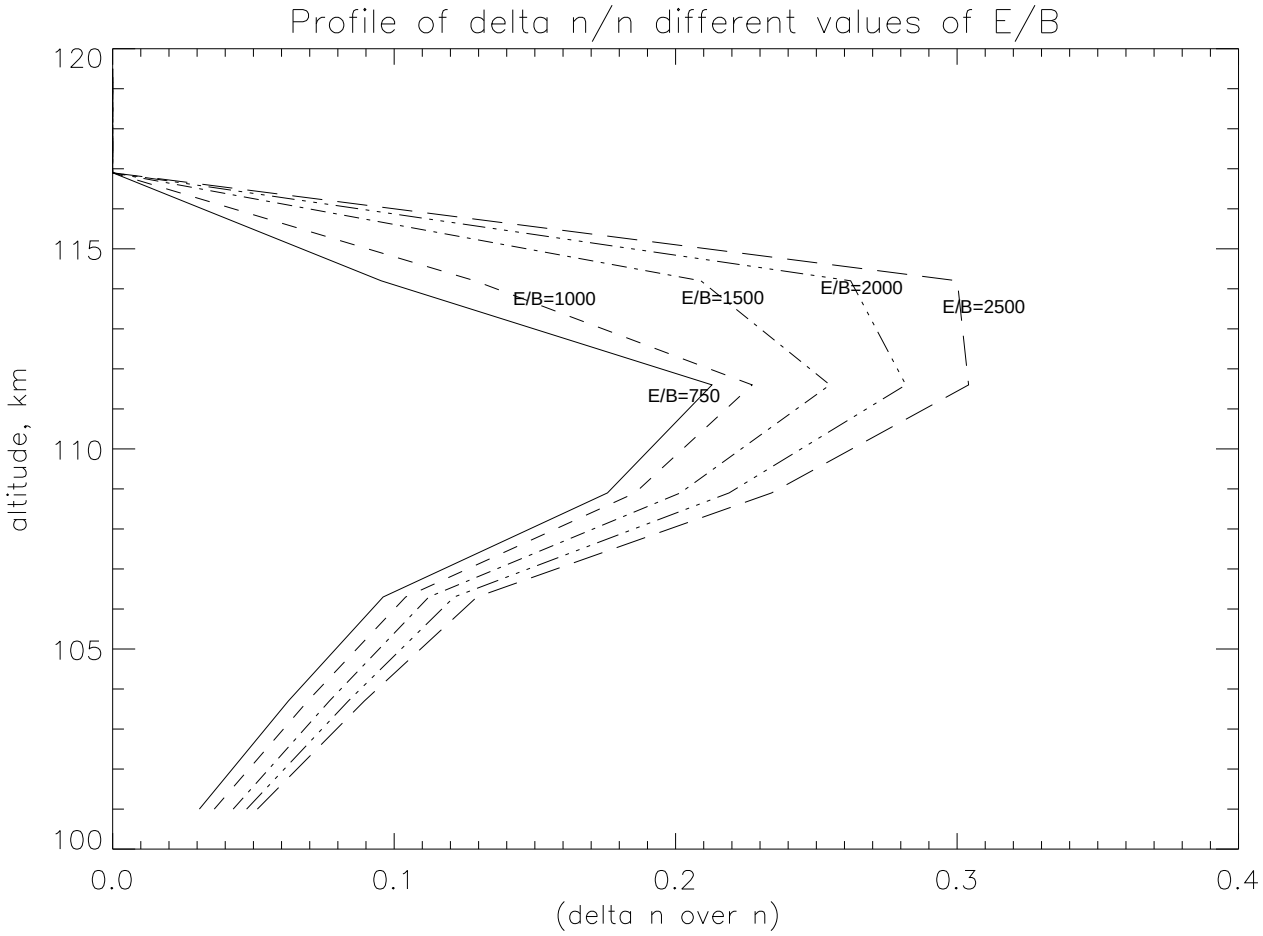

Figure 5.5: This figure shows various obtained values of the maximum value of $\delta n/n$ and its variation with altitude. The calculations were done for the different values of (E/B) shown with each trace. The calculations are for a flow angle $\theta = 0$.

As an exercise to assess the role played by electron heating the calculations shown in Fig. 5.5 were repeated for $T_e = T_n$ with the results presented in Fig. 5.6. The comparison between the two figures indicates that the density fluctuation level can go down by a factor close to 2 in the presence of strong electric fields owing to electron heating alone.

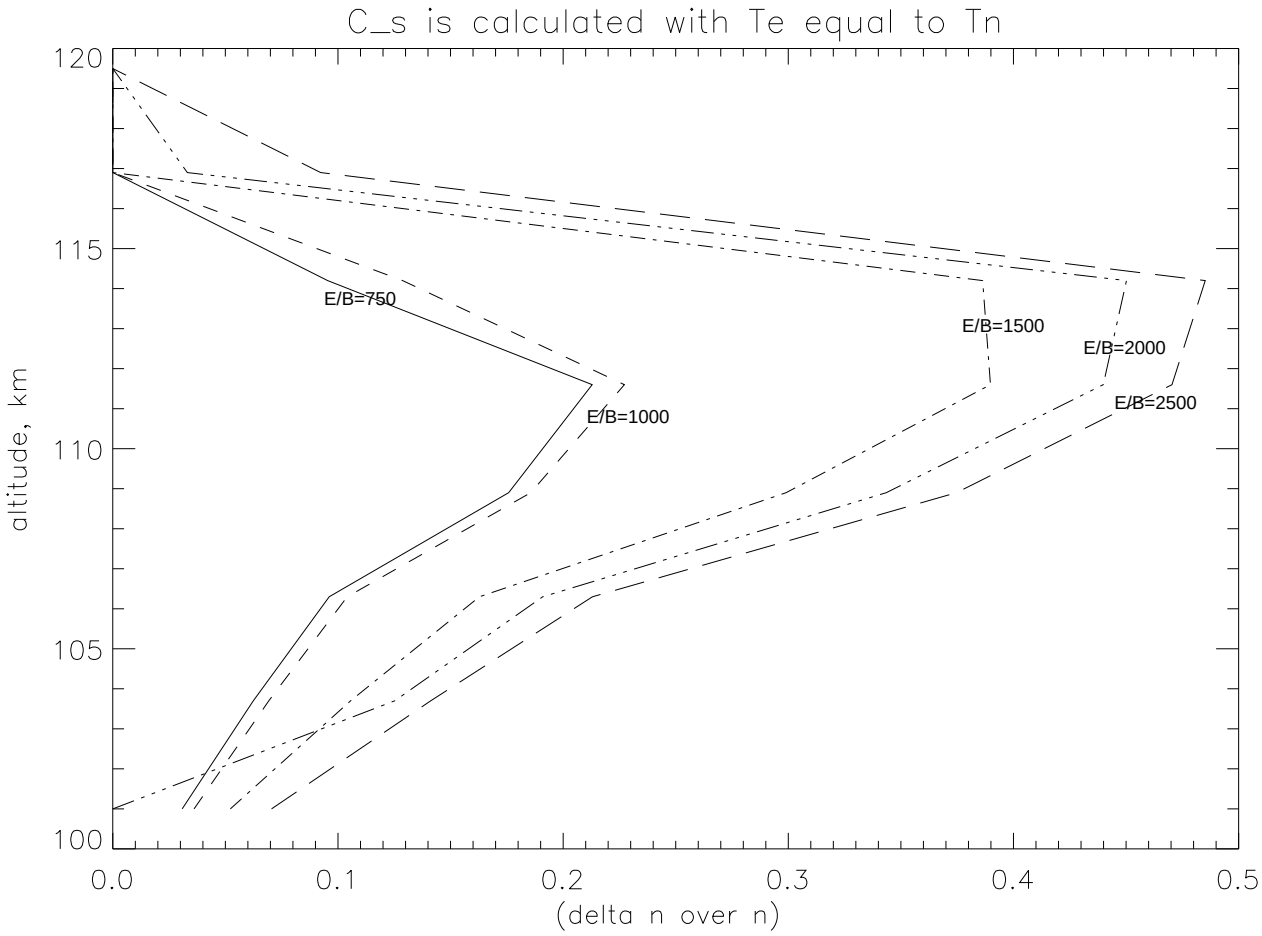

Figure 5.6: Same as Fig. 5.5 but with $T_e = T_n$ i.e., in the absence of electron heating by the plasma waves.

5.5.4 Irregularity impact on currents and average electric fields

As already discussed in an earlier section, currents must pass through the irregularities if the electric fields in the system have to be electrostatic (i.e., curl-free). Since we know the electric fields inside the structures we can then compute the currents they carry. In parallel to these calculations we can also address the question of the difference between the applied electric field and the average electric field in the turbulent medium. The latter is evidently smaller than the background field since the electric field of each structure is smaller than the ambient (e.g.Eqn 5.47).

5.5.4.1 A word about packing ratios

We have already ran into the question of a packing ratio in our discussion of the computed perturbed density profiles. The concept was first introduced for E region irregularities by *St.-Maurice and Hamza* [2001]. It should be obvious that since the structures are intermittent and grow through growth and decay stages the volume cannot be filled with the largest amplitude structures. This has been seen in CW observations by *Prikryl et al.* [1990] presented earlier. It is also quite clear in the computer simulations presented by, e.g., *Oppenheim et al.* [2008], that the plasma is far from being filled with very large amplitude density blobs or holes.

The calculations that will now be presented will depend on the value we choose for the packing ratio, R, which will be defined as $R = 2\delta\tau/\tau$, where τ is the volume and $\delta\tau$ will be the volume occupied by blobs, with an assumed similar number for holes and blobs (hence the factor 2 in the expression for R). In fact we can use the comparison between the computations of the maximum amplitudes shown in Fig. 5.5 and the observed rms (broadband) values from rocket measurements to conclude that R must be of the order of 0.2 to 0.3 when turbulence is strongly driven.

5.5.4.2 Electric fields in blobs versus holes

The expressions for electric fields inside blobs have already been presented. For clarity we should also show the electric fields inside holes and explicitly take into account the fact that their density fluctuations are negative rather than positive. Going back to 5.15 and using the conductivity ratios in terms of n_0/n_{tot} this means that we should use

$$\mathbf{E}_b^T = \left(1 - \frac{\delta n_b}{n_b}\right) \frac{\mathbf{E}_0 + \alpha \frac{\delta n_b}{n_b} \mathbf{E}_0 \times \mathbf{b}}{1 + \alpha^2 \left(\frac{\delta n_b}{n_b}\right)^2} \tag{5.55}$$

$$\mathbf{E}_h^T = \left(1 - \left|\frac{\delta n_h}{n_h}\right|\right) \frac{\mathbf{E}_0 - \alpha |\frac{\delta n_h}{n_h}| \mathbf{E}_0 \times \mathbf{b}}{1 + \alpha^2 \left(\frac{\delta n_h}{n_h}\right)^2} \tag{5.56}$$

In the eletric field expression for the hole we have chosen to use a negative sign in front of an absolute value instead of a positive sign in front of what should have been a negative value. Dealing with only positive values makes checking the algebra much easier.

With the signs explicitly sorted out, we will go back to the use of $\delta n/n$ inside both blobs and

holes, based on the fact that this number should be the same for blobs and holes now that the signs have all been defined as positive [*St.-Maurice and Hamza*, 2001].

5.5.4.3 Current density calculations

The total current densities in the system can now be computed in terms of $\delta n/n$ and of the packing ratio by adding the contributions from the background to those of blobs and holes. That is to say,

$$\mathbf{J}_{tot} = \Big[\sigma_{Pb}\mathbf{E}_b + \sigma_{Hb}\mathbf{E}_b \times \mathbf{b}\Big]\frac{\delta\tau}{\tau} + \Big[\sigma_{P0}\mathbf{E}_0 + \sigma_{H0}\mathbf{E}_0 \times \mathbf{b}\Big]\Big[1 - 2\frac{\delta\tau}{\tau}\Big] + \Big[\sigma_{Ph}\mathbf{E}_h + \sigma_{Hh}\mathbf{E}_H \times \mathbf{b}\Big]\frac{\delta\tau}{\tau} \quad (5.57)$$

We also know that $\sigma_{Pb} = \sigma_{P0}\frac{n_b}{n_0}$ and are about to use $|\frac{\delta\sigma_H}{\sigma_H}| = \frac{\delta n_b}{n_b} \simeq \frac{\delta n}{n}$. Defining $\Delta = 1 + \alpha^2\frac{\delta n^2}{n^2}$ we then find for the total current density in the system

$$\begin{aligned}
\mathbf{J}_{tot} = \Big[\sigma_{P0}\mathbf{E}_0 + \sigma_{H0}\mathbf{E}_0 \times \mathbf{b}\Big]\Big(1 - 2\frac{\delta\tau}{\tau}\Big) \\
+\frac{\delta\tau}{\tau\Delta}\Big\{\sigma_{P0}\mathbf{E}_0 + \sigma_{P0}\alpha\mathbf{E}_0 \times \mathbf{b} \\
+\sigma_{H0}\mathbf{E}_0 \times \mathbf{b} - \sigma_{H0}\alpha\frac{\delta n}{n}\mathbf{E}_0 \\
+\sigma_{P0}\mathbf{E}_0 - \sigma_{P0}\alpha\frac{\delta n}{n}\mathbf{E}_0 \times \mathbf{b} \\
+\sigma_{H0}\mathbf{E}_0 \times \mathbf{b} + \sigma_{H0}\alpha\frac{\delta n}{n}\mathbf{E}_0\Big\}
\end{aligned} \quad (5.58)$$

This gives the simple result,

$$\begin{aligned}
\mathbf{J}_{tot} = \Big[\sigma_{P0}\mathbf{E}_0 + \sigma_{H0}\mathbf{E}_0 \times \mathbf{b}\Big]\Big(1 - 2\frac{\delta\tau}{\tau}\Big) \\
+2\frac{\delta\tau}{\tau}\Big(\sigma_{P0}\mathbf{E}_0 + \sigma_{H0}\mathbf{E}_0 \times \mathbf{b}\Big)\frac{1}{\Delta}
\end{aligned} \quad (5.59)$$

That is to say,

$$\mathbf{J}_{tot} = \Big[\sigma_{P0}\mathbf{E}_0 + \sigma_{H0}\mathbf{E}_0 \times \mathbf{b}\Big]\Big(1 - 2\frac{\delta\tau}{\tau} + 2\frac{\delta\tau}{\tau}\frac{1}{1 + \alpha^2\frac{\delta n^2}{n^2}}\Big) \quad (5.60)$$

In turn this can be written as

$$\mathbf{J}_{tot} = \Big[\sigma_{P0}\mathbf{E}_0 + \sigma_{H0}\mathbf{E}_0 \times \mathbf{b}\Big]\Big[1 - 2\frac{\delta\tau}{\tau}\frac{\alpha^2\delta n^2/n^2}{1 + \alpha^2\frac{\delta n^2}{n^2}}\Big] \quad (5.61)$$

Expressed in a succinct manner this amounts to state that

$$\mathbf{J}_{tot} = \Big[\sigma_{P0}\mathbf{E}_0 + \sigma_{H0}\mathbf{E}_0 \times \mathbf{b}\Big](1-h) \tag{5.62}$$

$$h = R\frac{\alpha^2\delta n^2/n^2}{1+\alpha^2\frac{\delta n^2}{n^2}} \tag{5.63}$$

This means, interestingly, that both Pedersen and Hall currents are affected in exactly the same way. Also, as a check, if $\delta\tau \rightarrow 0$ or $\frac{\delta n}{n} \rightarrow 0$, and the results are those found in the absence of any irregularity. On the other hand, if the turbulence is very strong, we find from Eqn. 5.63 that $(1-h)$ becomes equal to $(1-R)$. A magnetometer would register Hall currents that are $(1-R)$ times smaller than expected from an applied field with magnitude E_0. This could mean current densities that could be as little as 70% of expectation. But this is not the full story, as we have to investigate not only the difference between average electric field and imposed electric fields for E region measurements and also whether or not there might be currents flowing between the E and F region so that F region measurements E_0 might not correspond to the E region E_0. The easier situation to assess is that of average versus background E region electric field.

5.5.4.4 Calculation of Average Electric Field

Radars, and even rockets, observe average electric fields, and not $\mathbf{E}_0$ when the measurements are from the E region. Calculating the average electric field is therefore very important if we are to relate the parameters to the direct observations. Using the same approach as for the total currents we must have

$$< \mathbf{E} >= \Big(1-2\frac{\delta\tau}{\tau}\Big)\mathbf{E}_0 + \frac{\delta\tau}{\tau}\mathbf{E}_b + \frac{\delta\tau}{\tau}\mathbf{E}_h \tag{5.64}$$

But

$$\begin{aligned}\mathbf{E}_b + \mathbf{E}_h = &\frac{n_0}{n_b}\Big[\mathbf{E}_0 + \alpha\frac{\delta n_b}{n_b}\mathbf{E}_0 \times \mathbf{b}\Big]/\Delta \\ &+\frac{n_0}{n_h}\Big[\mathbf{E}_0 - \alpha\frac{\delta n_b}{n_b}\mathbf{E}_0 \times \mathbf{b}\Big]/\Delta\end{aligned} \tag{5.65}$$

with, we recall, $\alpha = (\nu_i/\Omega_i)/(1+\Psi)$ and $\Delta = 1 + \alpha^2 \frac{\delta n^2}{n^2}$. Once again using

$$\frac{n_0}{n_b} = \frac{n_0 + \delta n_b}{n_b} - \frac{\delta n_b}{n_b} = 1 - \frac{\delta n_b}{n_b} \tag{5.66}$$

$$\frac{n_0}{n_h} = \frac{n_0 - |\delta n_h|}{n_h} + \frac{|\delta n_h|}{n_h} = 1 + \frac{\delta n_b}{n_b} \tag{5.67}$$

we end up with

$$\begin{aligned}
\mathbf{E}_b + \mathbf{E}_h &= \mathbf{E}_0 \Big\{ \frac{(1 - \frac{\delta n_b}{n_b} + 1 + \frac{\delta n_b}{n_b}}{\Delta} \Big\} \\
&+ \frac{\mathbf{E}_0 \times \mathbf{b}}{\Delta} \Big\{ (1 - \frac{\delta n_b}{n_b}) \alpha \frac{\delta n_b}{n_b} - (1 + \frac{\delta n_b}{n_b}) \alpha \frac{\delta n_b}{n_b} \Big\} \\
&= \frac{1}{\Delta} \Bigg[2\mathbf{E}_0 + \mathbf{E}_0 \times \mathbf{b} \Big[\alpha \frac{\delta n}{n} - \alpha (\delta n/n)^2 - \alpha \frac{\delta n}{n} - \alpha (\delta n/n)^2 \Big] \Bigg] \\
&= \frac{1}{\Delta} \Bigg[2\mathbf{E}_0 - 2\mathbf{E}_0 \times \mathbf{b} \;\; \alpha (\delta n/n)^2 \Bigg]
\end{aligned} \tag{5.68}$$

Therefore,

$$< \mathbf{E} >= \Big(1 - 2\frac{\delta\tau}{\tau}\Big)\mathbf{E}_0 + 2\frac{\delta\tau}{\tau\Delta} \Bigg[\mathbf{E}_0 - \mathbf{E}_0 \times \mathbf{b} \;\; \alpha \Big(\frac{\delta n}{n}\Big)^2 \Bigg] \tag{5.69}$$

$$= \mathbf{E}_0 \Bigg[1 + \frac{2\delta\tau}{\tau} \Big(\frac{1}{\Delta} - 1 \Big) \Bigg] - \mathbf{E}_0 \times \mathbf{b} \frac{2\delta\tau}{\tau} \frac{\alpha (\delta n/n)^2}{\Delta} \tag{5.70}$$

$$= \mathbf{E}_0 - \mathbf{E}_0 \frac{2\delta\tau}{\tau} \Bigg[\frac{\alpha^2 \delta n^2/n^2}{1 + \alpha^2 \delta n^2/n^2} \Bigg] - \mathbf{E}_0 \times \mathbf{b} \frac{2\delta\tau}{\tau} \frac{\alpha \delta n^2/n^2}{1 + \alpha^2 \delta n^2/n^2} \tag{5.71}$$

The end result is

$$< \mathbf{E} >= \mathbf{E}_0 \Big[1 - h \Big] - \mathbf{E}_0 \times \mathbf{b} \frac{h}{\alpha} \tag{5.72}$$

The magnitude of this average electric field is given by

$$| < \mathbf{E} > | = E_0 \sqrt{(1-h)^2 + \frac{h^2}{\alpha^2}} \tag{5.73}$$

The average electric field includes a rotation away from the imposed electric field direction. However, even with the limiting case $h = 0.3$ the rotation does not amount to much since α should

normally be expected to be of order 5 or greater. Likewise the magnitude is reduced from the background value by a factor close to $(1 - h)$. This is an upper limit however. More detailed calculations in terms of packing ratios and broadband density values as a function of altitude and E_0 would be needed for a more precise determination with values that would obviously be smaller than this upper estimate.

5.5.4.5 Impact on the estimation of 'Anomalous' Conductivities

Expressions for the total currents and average electric fields were presented above. The question this raises is the following: if the input is the average E region electric field and if currents are recorded from the E region (for example, magnetometers measure essentially Hall currents from below 120 km) then what would be the conductivity expression that should be used? There would be every reason to define the new relation between total currents and average electric fields as coming from an 'anomalous' conductivity tensor.

There is more than one way to do the calculation. One is to simply write

$$\mathbf{J}_{tot} = \left[\sigma_P^* < \mathbf{E} > + \sigma_H^* < \mathbf{E} > \times \mathbf{b}\right]$$

and to use the expressions posted above for $\mathbf{J}_{tot}$ and for $< \mathbf{E} >$. This would introduce two linear equations with two unknowns from which the anomalous conductivities would be extracted. Here, however, a different approach based on taking dot products of the current with each of the two average field components. The results from both approaches are of course the same.

Using the second approach first write

$$\mathbf{J}_{tot} = \left[\sigma_{P0}\mathbf{E}_0 + \sigma_{H0}\mathbf{E}_0 \times \mathbf{b}\right](1 - h) \tag{5.74}$$

This means that

$$\mathbf{J}_{tot} \cdot < \mathbf{E} > = \sigma_P^* < \mathbf{E} >^2 \tag{5.75}$$

Also,

$$\sigma_H^* \mathbf{E}_0^2 = \mathbf{J}_{tot} \cdot < \mathbf{E} \times \mathbf{b} > \tag{5.76}$$

In more concise form

$$\mathbf{J}_{tot} = \Big[\sigma_{P0}\mathbf{E}_0 + \sigma_{H0}\mathbf{E}_0 \times \mathbf{b}\Big](1-h) \tag{5.77}$$

$$< \mathbf{E} >= \mathbf{E}_0\Big[1-h\Big] - \mathbf{E}_0 \times \mathbf{b}\frac{h}{\alpha} \tag{5.78}$$

where

$$h = \frac{2\delta\tau}{\tau}\Big[\frac{\alpha^2\delta n^2/n^2}{1+\alpha^2\delta n^2/n^2}\Big] \tag{5.79}$$

We know that

$$\mathbf{J}_{tot}\cdot < \mathbf{E} >= \sigma_P^* < \mathbf{E} >^2 \tag{5.80}$$

From Eqns. 5.77 and 5.78 the left hand side (LHS) of Eqn. 5.80 has to be given by

$$\mathbf{J}_{tot}\cdot < \mathbf{E} >= \Big(\sigma_{P0}(1-h)^2 - \sigma_{H0}(1-h)\frac{h}{\alpha}\Big){E_0}^2 \tag{5.81}$$

However, from 5.80 and 5.78 the right hand side (RHS) of 5.81 has to be equal to

$$\sigma_P^* E_0^2\Big[(1-h)^2 + \frac{h^2}{\alpha^2}\Big] \tag{5.82}$$

With, as discussed previously, $\sigma_{P0}/\sigma_{H0} = -1/\alpha$, we then find

$$\sigma_P^* = \frac{\sigma_{P0}(1-h)}{(1-h)^2 + \frac{h^2}{\alpha^2}} \tag{5.83}$$

The anomalous Hall conductivity is computed in a similar manner, starting with

$$\sigma_H^* \mathbf{E}_0^2 = \mathbf{J}_{tot}\cdot < \mathbf{E} > \times\mathbf{b} \tag{5.84}$$

This means that

$$\mathbf{J}\cdot < \mathbf{E} > \times\mathbf{b} = \sigma_H^* < \mathbf{E} >^2 \tag{5.85}$$

$$\sigma_{H0}\Big[(1-h)^2 + \frac{h}{\alpha^2}(1-h)\Big]E_0^2 = \sigma_H^* E_0^2\Big[(1-h)^2\frac{h}{\alpha^2}\Big] \tag{5.86}$$

and therefore,

$$\sigma_H^* = \sigma_{H0}\frac{\left[(1-h)^2 + \frac{h}{\alpha^2}(1-h)\right]}{(1-h)^2 + h^2/\alpha^2} \tag{5.87}$$

where h has been defined in Eqn. 5.79

5.5.4.6 Changes in the mean electric field

Rocket measurements have produced not just density fluctuation profiles but also rms profiles of electric field fluctuations. We investigate here what could be done to produce similar profiles from the new theory.

As a first step we set out to compute the magnitude of the difference between the average and background electric fields, namely the magnitude of $\frac{|\Delta E|}{E_0}$. For starting point consider

$$\Delta\mathbf{E} = <\mathbf{E}> - \mathbf{E}_0 \tag{5.88}$$

$$|\Delta\mathbf{E}|^2 = |<\mathbf{E}> - \mathbf{E}_0|^2 \tag{5.89}$$

From the expressions presented in a previous section we then obtain

$$<\mathbf{E}> - \mathbf{E}_0 = (1 - \frac{2\delta\tau}{\tau})\mathbf{E}_0 - \mathbf{E}_0 + \frac{\delta\tau}{\tau}\frac{1}{\Delta}\Big[2\mathbf{E}_0 - 2\mathbf{E}_0\times\mathbf{b}\ \alpha\frac{\delta n^2}{n^2}\Big] \tag{5.90}$$

$$= 2\frac{\delta\tau}{\tau}\Big[-\mathbf{E}_0 + \frac{\mathbf{E}_0}{\Delta} - \frac{2\mathbf{E}_0\times\mathbf{b}}{\Delta}\ \alpha\frac{\delta n^2}{n^2}\Big] \tag{5.91}$$

$$= 2\frac{\delta\tau}{\tau}\Big[-\frac{\mathbf{E}_0}{\Delta}\ \alpha^2\frac{\delta n^2}{n^2} - \frac{\mathbf{E}_0\times\mathbf{b}}{\Delta}\ \alpha\frac{\delta n^2}{n^2}\Big] \tag{5.92}$$

with $\alpha = (\nu_i/\Omega_i)/(1+\Psi)$. This means that

$$|<\mathbf{E}> - \mathbf{E}_0|^2 = \Big(\frac{2\delta\tau}{\tau}\Big)^2\frac{E_0^2\Big[\alpha^4\frac{\delta n^4}{n^4} + \alpha^2\frac{\delta n^4}{n^4}\Big]}{\Big(1+\alpha^2\frac{\delta_n^2}{n^2}\Big)^2} \tag{5.93}$$

so that we therefore get

$$\frac{|<\mathbf{E}> - \mathbf{E}_0|^2}{E_0^2} = \Big(\frac{2\delta\tau}{\tau}\Big)^2\frac{\Big(\alpha^2\frac{\delta n^2}{n^2}\Big)^2\Big(1+\frac{1}{\alpha^2}\Big)}{\Big(1+\alpha^2\frac{\delta n^2}{n^2}\Big)^2} \tag{5.94}$$

In conclusion

$$\left|\frac{<\mathbf{E}> -\mathbf{E}_0}{E_0}\right| = R\frac{\left(\alpha^2\frac{\delta n^2}{n^2}\right)\left(\sqrt{1+\frac{1}{\alpha^2}}\right)}{\left(1+\alpha^2\frac{\delta n^2}{n^2}\right)} \tag{5.95}$$

where we recall that R is the packing ratio $(2\delta\tau/\tau)$. From Eqn. 5.95 we can conclude that if $\alpha\frac{\delta n}{n} > 1$ and $\alpha >> 1$ then

$$\left(\frac{\Delta E}{E_0}\right) \cong 2\frac{\delta\tau}{\tau} = R \tag{5.96}$$

Alternatively, we can assume that if the electric field measurement comes from the E region itself then we should be interested in the ratio $|\Delta E|/|<\mathbf{E}>|$ instead of $|\Delta E|/|E_0|$. In that case we need to compute

$$\frac{|\Delta\mathbf{E}|^2}{|<\mathbf{E}>|^2} = \frac{|<\mathbf{E}> -\mathbf{E}_0|^2}{<\mathbf{E}>^2} = \left|\frac{<\mathbf{E}> -\mathbf{E}_0}{E_0}\right|^2\frac{E_0^2}{<\mathbf{E}>^2} \tag{5.97}$$

But from (5.73) we have found

$$\frac{<\mathbf{E}>^2}{E_0^2} = (1-h)^2 + \frac{h^2}{\alpha^2} \tag{5.98}$$

Using

$$h = R\frac{\alpha^2\frac{\delta n^2}{n^2}}{\left(1+\alpha^2\frac{\delta n^2}{n^2}\right)} \tag{5.99}$$

we find in fact from 5.95 that

$$\left|\frac{<\mathbf{E}> -\mathbf{E}_0}{E_0}\right| = h\sqrt{(1+1/\alpha^2)} \tag{5.100}$$

This means that we have

$$\frac{|\Delta\mathbf{E}|}{|<\mathbf{E}>|} = \frac{h\sqrt{(1+1/\alpha^2)}}{\sqrt{(1-h)^2+\frac{h^2}{\alpha^2}}} \tag{5.101}$$

5.5.4.7 Electric field fluctuations

While it may have some usefulness the equations presented thus far offer only different perspectives on the average electric field. For rocket observations we should calculate the perturbation electric field in various blobs or holes at a given altitude for a given E_0 field and from various computations obtain a broadband value for the electric field magnitude. As a simple first crack at the problem we will assume that there is a narrow amplitude and electric field fluctuation around the maximum

value that has been already produced above.

To go from a density fluctuation to an electric field fluctuation associated with an individual blob we simply need to go back to the beginning of this chapter and write the total electric field $\mathbf{E}^T$ inside a blob in the form

$$\mathbf{E}^T = A\mathbf{E}_0 + B\mathbf{E}_0 \times \mathbf{b} \tag{5.102}$$

So, we have

$$\delta\mathbf{E} = \mathbf{E}^T - \mathbf{E}_0 = (A-1)\mathbf{E}_0 + B\mathbf{E}_0 \times \mathbf{b} \tag{5.103}$$

This can be written in the form

$$\delta\mathbf{E} = \frac{[(n_0/n_b - 1) - G^2]\mathbf{E}_0 + n_0/n_b G\mathbf{E}_0 \times \mathbf{b}}{1+G^2} \tag{5.104}$$

where $G = \alpha\delta n_b/n_b$. Then, with $n_0/n_b - 1 = -G/\alpha$ we end up with the magnitude given by

$$\left|\frac{\delta\mathbf{E}}{E_0}\right| = \frac{G\sqrt{(1+1/\alpha^2)}}{\sqrt{1+G^2}} \tag{5.105}$$

This expression should be multiplied by the packing ratio to allow for the integration over all realizations, even though we have essentially modeled the process through a delta function at the maximum amplitude. The final result then resembles what was found for the deviation of the average field from the ambient field but is not quite the same. Usually $\alpha > 1$ and large enough that the factor $1/\alpha^2$ does not contribute much. Then for large $\delta n/n$ values this means $|\delta E| \rightarrow E_0$. By contrast, for very small density fluctuations i.e $G << 1$, this expression gives instead $|\delta E| \rightarrow E_0 G$, which is, as expected for such a situation, the linear theory result. Note that we should expect G to not be much greater than 1, so that the perturbed E field inside a structure should not be expected to be more than 0.7 times the ambient field.

In tables 5.2 and 5.3, some estimates are provided for the parameters that have been discussed in the present chapter. The first column gives the various altitudes. It is followed by the broadband density fluctuation level estimated from the maximum amplitude calculations multiplied by R. The third column gives the model values of D used for the calculations of the density and electric field perturbations at maximum amplitude. The factor h is calculated from Eqn. 5.63. The next column gives the magnitude of $< \mathbf{E} > /E_0$ using Eqn. 5.73. Eqn. 5.105 has been used to calculate $|\delta\mathbf{E}/E_0|$.

Height(km)	δn/n	D	h	$\|<\mathbf{E}>\|/E_0$	$\|\delta\mathbf{E}/E_0\|$	σ_P^*/σ_{P0}	σ_H^*/σ_{H0}
103.700	0.062	2.047	0.048	0.952	0.693	1.050	1.000
108.900	0.176	1.855	0.032	0.968	0.588	1.033	1.002
111.600	0.214	1.694	0.017	0.983	0.453	1.017	1.004
114.200	0.099	1.568	0.001	0.999	0.141	1.001	1.001

Table 5.2: Turbulence-related parameters for a packing ratio $R = 0.1$

Height(km)	δn/n	D	h	$\|<\mathbf{E}>\|/E_0$	$\|\delta\mathbf{E}/E_0\|$	σ_P^*/σ_{P0}	σ_P^*/σ_{P0}
103.700	0.062	2.047	0.143	0.857	0.693	1.167	1.001
108.900	0.176	1.855	0.097	0.903	0.588	1.107	1.006
111.600	0.214	1.694	0.050	0.950	0.453	1.052	1.011
114.200	0.099	1.568	0.003	0.997	0.142	1.003	1.003

Table 5.3: Turbulence-related parameters for a packing ratio $R = 0.2$

The last two columns in the tables give the anomalous to ordinary conductivity ratios calculated from Eqns. (5.83) and (5.87 respectively.

As seen through Eqn. 5.99, h is proportional to R and has a significant role is reducing the values of the calculated parameters. From the expression for h it is easy to show that for large density fluctuation levels $h \rightarrow R$. The results shown in tables 5.3 and 5.2 indicates that the Pedersen conductivity goes down significantly with altitude while the Hall conductivity remains unaffected, whereas the average E field can go down become smaller than the background E_0 field by as much as 12 percent.

5.6 Summary

The nonlinearities associated with the Farley-Buneman and gradient-drift instabilities in the E-region have been described here using intermittency instead of mode-coupling based on a Fourier analysis. New equations were created to describe the evolution of blobs and holes based on a rotation of the electric field inside elongated structures.

The treatment of the electric field rotation inside the structures differs from the one used by *St.-Maurice and Hamza* [2001] because the latter authors rotated the electric field together with the density structures. The new insights whereby the field rotated within the structures themselves was inspired by the work of *Hysell and Drexler* [2006].

The results presented with the new model has a lot of similarity to the expressions presented by *St.-Maurice and Hamza* [2001] but the differences remain mathematically important owing the an additional term of the form a factor of $(1-\delta n/n)$ multiplying the previous values. The basic physics used here has been based on the notion that elongated structures create an initial polarization field which eventually helps to bring the E field down inside the structures through multiple polarization effects. The corrected total E field inside the structure has been calculated for both blobs and holes.

With the results from the new calculations of electric field inside the structures and using parameters based on the MSIS 90E model, profile plots of broadband density fluctuation levels estimates were produced. The profiles do resemble observed profiles particularly for strong electric field conditions, but some tweaking seems to be needed. It seems that gradient drift waves excited near the bottom side of the E region would be needed to produce a better agreement with observed profiles. Such a calculation has not been carried out here, but it would in the end be a simple matter of changing the threshold speed of the instability from C_s to something smaller.

Average electric fields and currents were also calculated in this chapter. Both were found to decrease by non-negligible amounts owing to the presence of the turbulent structures. Expressions for anomalous conductivities were also produced.

It should be noted that the packing ratio is a parameter that could not be obtained from first principles in the present work. This parameter can however be found indirectly by scaling the calculated maximum density fluctuations obtained here to make them agree with observed profiles. For strongly turbulent situations, a packing ratio of order 0.2 is indicated. With the R factor in hand, it becomes feasible to calculate the overall reduction of currents and conductivities from the initial values. Those values are important since they imply electric field reductions and conductivity changes by as much as 30%.

Chapter 6

Conclusions and Suggestions for Future Work

6.1 Conclusion

The research carried out in this thesis is based on an approach previously adopted by *St.-Maurice and Hamza* [2001]. In their approach, rotation of the structures were used to study the electric fields and various other parameters inside blobs and holes.

Hysell and Drexler [2006], in their research showed that the electric field inside elongated structures would rotate by comparison to the field outside the structures. I carried out my research by using the same idea, starting with elongated enhanced density structures aligned along the background electric field $\mathbf{E}_0$. When an enhancement moves along the $\mathbf{E}_0 \times \mathbf{b}$ direction, an initial polarization field $\delta\mathbf{E}$ is generated which in turn, creates a $\delta\mathbf{E} \times \mathbf{b}$ drift. This process continues until the growth rate is almost zero. At that point the monotonic increase in the aspect angle of a structure makes it decay until its amplitude matches the background density of the medium.

The new electric field derivation has produced the following expression for the electric field inside density structures:

$$\mathbf{E}^T = (1 - \frac{\delta n_b}{n_b}) \frac{\mathbf{E}_0 + \alpha \frac{\delta n_b}{n_b} \mathbf{E}_0 \times \mathbf{b}}{1 + \alpha^2 (\frac{\delta n_b}{n_b})^2} \tag{6.1}$$

The factor $(1 - \delta n/n)$ did not appear in the expressions obtained by *St.-Maurice and Hamza* [2001] who used a different model in which the structures were rotated in sync with the electric field. This new factor is a result of the different geometry being used here. It eliminates the conundrum that *St.-Maurice and Hamza* [2001] had, which was that all large amplitude structures were to be found on the edge of the instability cone.

In order to verify this newly derived concept of electric field rotation and properties, I have used a particular method to input various values of $\delta n/n$ to understand the growth and decay of

the structures. Therefore, using the concept that large amplitude structures are observed along C_S, calculations were done to relate the electric field amplitude inside the structures with C_s. The MSIS 90E model provided various parameters to calculate α for the ions and the electrons,Ψ. For the C_s calculation a standard ion frictional heating calculation was used while a new empirical model based on many observations was used for the electrons. It was also assumed that $\theta = 0$ along the $\mathbf{E}_0 \times \mathbf{B}$ direction provided representative density fluctuation estimates. This lead to the production of profile plots of the broadband density fluctuations. The produced profile plot Fig. 5.5 has some important similarities with the broadband density fluctuation levels published in *Kelley and Mozer* [1973], *Pfaff* [1991] as mentioned in their rocket observations. Therefore an important contribution from this thesis is the introduction of an approach where we can stay away from Fourier analysis. Even though the approach is in some ways quite similar to what has been uncovered in mode-coupling studies, it provides a rather clear physical understanding for the growth and decay of density enhancements or depletions as function of electric field strength.

The structures discussed in the thesis are intermittent structures. Even if these structures have 30 percent amplitude, it's far from filling entirely with plasma. If the observed broadband density fluctuations from the rocket is 10 percent then it implies that the packing ratio is of the order of $1/3$. Therefore, using the concept of packing ratio (R) brought up by *St.-Maurice and Hamza* [2001], the ratio of average electric field to the background electric field E_0 seems to go down by roughly 10-12 percent as a result of the electric field rotation inside the structures for moderately strong background electric fields. The focus here has been on various expressions to obtain the strength of the fluctuation electric fields based on the packing ratio. It's also important to note that the fluid theory amplitude calculations are independent of the wavelength of the structures. However it should be recalled that R includes parameters that change with the wave number. Large values of $\delta n/n$ implies large value of k and vice-versa. Therefore, the packing ratio includes the presence of cut-off at smaller wavelengths while at larger wavelengths there is another cut-off as the growth rate depends on k^2. At that point the theoretical model described in the thesis doesn't apply.

Understanding the anomalous transport properties caused by the irregularities is important. Based on the ideas presented in the *St.-Maurice and Hamza* [2001] I studied the anomalous transport properties in my thesis. Due to the rotation of the electric field inside the structures, the electrons acquire anomalous drift along the original E_0 direction and similarly the anomalous

Hall drift. The IS radars can measure the average ion drift. Therefore, the ion mobility should be computed using the work presented in this thesis. As for the anomalous conductivities, they could introduce unexpected currents that would affect things like the interpretation of magnetometer data. This stated, with a packing ratio of R=0.1, the Pedersen conductivity would only go down by goes 5% while a value of R=0.2 would have it go down by 10 percent. However, the Hall conductivities for the ions remain largely unaffected, as shown in tables 5.1 and 5.2.

While using T_e as a function of altitude to calculate C_s, it was also found that $\delta n/n$ is significantly greater (almost a factor of 2 for very strong ambient electric fields) if we use $T_e = T_n$. This emphasizes the fact that the plasma is less turbulent owing to electron heating from the very plasma waves that affect them.

An important message conveyed through my calculations is that if we impose an outside E field, then the average **<E>** could be as much as 10 percent to even 20 percent smaller. There is absolutely no doubt to the fact that E inside the structure is smaller than the outside E field because when you look at a structure, they go with the ion-acoustic speed and they will not do so unless E field of the structure is of the threshold value. I have shown how to calculate this. Unfortunately, the only catch is the packing ratio, and it is difficult to obtain. Future research would go into how to handle $\delta n/n$ and relate it to a packing ratio (R) in a way that does not require observations.

6.2 Suggestions for Future Work

One question to explore in the future is the following: since the average E region electric field is weaker than the imposed E_0 field seen higher up in the F region, should there be an average parallel current to take care of the change in the electric field with altitude? The answer might be yes. Given that blob and hole electric fields are produced by the same perpendicular velocity shears along the magnetic field, the parallel E fields (which heat the electrons) should be similar but with opposite signs. The symmetry between blob and hole fields means that no net parallel electric field should be expected. Paradoxically, this should mean that there would a net parallel current on average because the average $< \delta n \delta E_{\parallel} >$ cannot be zero if the only difference between parallel fields is their signs. With their smaller number densities the holes have to carry a smaller current density than the blobs, so that a net downward parallel current would be triggered by the large amplitude density

structures.

As mentioned in Chapter 5, one limitation of the work is that we have been unable to determine the packing ratio R from first principles. We had to resort to a scaling of the derived maximum amplitude fluctuation level to introduce an agreement between our calculations and the observations. Another avenue to check would be through the use of the electron temperature, from which the heating rates from the waves could be extracted. The heating rate has to be proportional to the square of the density fluctuation levels. This would offer an alternative scaling method for the empirical determination of R.

Another study would consist in comparing <**E**> seen by radars with instantaneous **E** fields observed by rockets. Because ERRRIS measured the E field with rockets and radars at the same time, we could find a good comparison of <**E**> and **E**. A puzzling aspect of the rocket observations is that at least during the ERRRIS campaign, on both the upleg and downleg, the background (average?) electric field reached a maximum at the very altitude where the turbulence was most intense, near 110 km. A detailed comparison with radar data retrieved from the F region would have helped to either establish that this was a strange coincidence or would have been useful to sort a mechanism related to the physics dealt with in the present thesis.

Related to the above questions is the question of the electric field generation. A careful study based for instance on simultaneous E and F region observations by an Incoherent Scatter Radar might help establish from the ion motion throughout the E and F regions if the system is driven by a power generator versus a current generator. For instance a smaller E field in the presence of the irregularities would imply that the system is driven by a current generator but we might have the opposite trend if the generator is driven by a perpendicular potential drop.

Another point to note is, if we go with the imposed $\mathbf{E}_0$ field, the Hall currents are reduced by a certain factor $(1 - h)$. We should not be calling this an anomalous current, and instead, we should say that when this $\mathbf{E}_0$ field is applied, the $(1 - h)$ factor gives us currents that are 85 percent of the actual value because of the reduction. That is something cannot be spotted easily unless there is excellent electron density data in the region. The possible solution could be to measure currents from a magnetometer with good radar coverage of the region. The electron densities are important for the calculation of Hall currents. They have to be in the field of view of the radar. Magnetometers would measure the currents. If we have the needed electron density and the <**E**>

field, we can address the question about the currents. The problem with σ_H^* is that we are only getting a few percents off with my calculations. If we think about it, it is not going to work if we start with <**E**>. However, if we measure **E** from rockets, then we would have an actual imposed **E** field and eventually would end up with much smaller Hall currents.

People could argue that using coupling models for ionosphere and magnetosphere might have an imposed **E** field and they would calculate currents as if the activities were normal. However, it will not be right as the **E** field will always be changed by irregularities. The effect needs to be quantified better in the future. In this regard, it should be noted that *Dimant and Oppenheim* [2011] estimated much higher anomalous conductivities than were retrieved in the present thesis, with density perturbations of the order of the background and even larger! However, those authors based their estimates on quasilinear arguments whereby the electrons were assumed to follow a $\delta\mathbf{E} \times \mathbf{B}$ drift along the original electric field direction. With fewer electrons in depletions (our holes) than in the enhancements (our blobs), they obtained large 'anomalous' currents. There are two problems with that approach. First, it ignored the effect of the packing ratio which should cut down their estimates by a factor of order 3 or more. Secondly, it ignored the fact that with any inhomogeneity along the long structures, polarization electric fields would partially stop the electron currents (apart from fringe electric fields, as described in Chapter 4). In this regard, it is important to recall once again that the observations are showing that the field of the structures is indeed smaller than the ambient field, which is why the structures move at the threshold speed at their maximum amplitude. It is important to realize that there is simply no reasonable way to reduce the electric field inside the structures unless there is a polarization electric field along the elongated axis of the structures. If the quasilinear arguments of Dimant and Oppenheim had been valid, the ambient electric field itself would have gone down instead of the field inside the elongated structures.

A broadband density fluctuation peak seems to often be observed around 100 km altitude. *Haldoupis et al.* [2000], using EISCAT data, found that presence of gradient-drift scales to be significant in the presence of auroral precipitation. A non-linear gradient-drift (GD) theory should be revisited with the approach used in my work. The calculations can be done the way it is used in the equatorial regions and then introduce the chemistry in the growth rates. It has been done by

St-Maurice and Choudhary [2006] but needs to be revisited because these authors used a theory where they were tilting the whole structures as opposed to rotating the E field inside of them.

Bibliography

Balsley, B. B., and W. L. Ecklund (1972), VHF power spectra of the radar aurora, *Journal of Geophysical Research*, *77*, 4746–4760.

Baumjohann, W., and R. A. Treumann (2012), *Basic space plasma physics*, World Scientific Publishing Company.

Brower, L., J. P. Thayer, and J.-P. St.-Maurice (2009), Frictionally heated electrons in the high-latitude d region, *Journal of Geophysical Research: Space Physics*, *114*(A12), doi:10.1029/2009JA014421.

Buneman, O. (1963), Excitation of field aligned sound waves by electron streams, *Phys. Rev. Lett.*, *10*, 285–287.

Chaturvedi, P. K., and S. L. Ossakow (1979), Nonlinear stabilization of the ExB gradient drift instability in ionospheric plasma clouds, *Journal of Geophysical Research: Space Physics*, *84*(A2), 419–421.

Chau, J. L., and J.-P. St.-Maurice (2016), Unusual 5 m E region field-aligned irregularities observed from northern Germany during the magnetic storm of 17 march 2015, *Journal of Geophysical Research: Space Physics*, *121*(10), 10,316–10,340.

Chen, D. (1996), Convective properties of Farley-Buneman waves at high latitude E-region, *Ph.D. thesis, The University of Western Ontario, London, Ontario, Canada*.

Chian, A.-L., and Y. Kamide (2007), An overview of the solar-terrestrial environment, *Handbook of the Solar-Terrestrial Environment*, p. 2.

Cohen, R., and K. L. Bowles (1967), Secondary irregularities in the equatorial electrojet, *Journal of Geophysical Research*, *72*(3), 885–894.

Davies, K. (1965), *Ionospheric Radio Propagation*, National Bureau of Standards.

Dettwiler, M. (2017), RADARSAT Constellation-Canadian Space Agency, [online] Available at: http://http://www.asc-csa.gc.ca/eng/satellites/radarsat/what-is-rcm.asp [Accessed 25 Sept. 2018].

Dimant, Y., and M. Oppenheim (2011), Magnetosphere-ionosphere coupling through E region turbulence: 2. Anomalous conductivities and frictional heating, *Journal of Geophysical Research: Space Physics*, *116*(A9).

Dimant, Y., and R. Sudan (1997), Physical nature of a new cross-field current-driven instability in the lower ionosphere, *Journal of Geophysical Research: Space Physics*, *102*(A2), 2551–2563.

Dimant, Y. S., and M. Oppenheim (2004), Ion thermal effects on E-region instabilities: linear theory, *Journal of atmospheric and solar-terrestrial physics*, *66*(17), 1639–1654.

Donovan, E. (2014), UofC Auroral Imaging - RISR-C, [online] Available at: http://aurora.phys.ucalgary.ca/resu/index.html [Accessed 25 Aug. 2018].

Drexler, J. (2005), Convective E region irregularities at high latitudes., *Ph.D. thesis, The University of Western Ontario, London, Ontario, Canada*.

Drexler, J., J.-P. S. Maurice, D. Chen, and D. Moorcroft (2002), New insights from a nonlocal generalization of the Farley-Buneman instability problem at high latitudes, *Annales Geophysicae*, *20*(12), 2003–2025.

Eglitis, P., T. R. Robinson, I. W. McCrea, K. Schlegel, T. Nygren, and A. S. Rodger (1995), Doppler spectrum statistics obtained from three different-frequency radar auroral experiments, *Annales Geophysicae*, *13*, 56–65.

Endawoke, Y. (2018), Dr Endawoke Yizengaw Personal website, [online] Available at: https://www2.bc.edu/endawoke-kassie/ionosphere.html [Accessed 25 Aug. 2018].

Farley, D. T. (1963), Two-stream plasma instability as a source of irregularities in the ionosphere, *Phys. Rev. Lett.*, *10*, 279–282.

Farley, D. T., H. M. Ierkic, and B. G. Fejer (1981), Radar interferometry: A new technique for studying plasma turbulence in the ionosphere, *Journal of Geophysical Research: Space Physics*, *86*(A3), 1467–1472.

Fejer, B. G., and D. T. Farley (1975), The effect of the gradient drift term on type 1 electrojet irregularities, *Journal of Geophysical Research*, *80*(10), 3087–3090.

Fejer, B. G., and M. C. Kelley (1980), Ionospheric irregularities, *Reviews of Geophysics*, *18*(2), 401–454.

Fejer, B. G., J. Providakes, D. T. Farley, and W. E. Swartz (1986), Auroral E region plasma waves and elevated electron temperatures, *Journal of Geophysical Research: Space Physics*, *91*(A12), 13,583–13,592.

Foster, J., and P. Erickson (2000), Simultaneous observations of e-region coherent backscatter and electric field amplitude at f-region heights with the millstone hill uhf radar, *Geophysical research letters*, *27*(19), 3177–3180.

Friker, A., and F.-J. Lübken (1992), Neutral air density and temperature measurements by the TOTAL instrument aboard the ROSE payloads, *Journal of Atmospheric and Terrestrial Physics*, *54*(6), 693–701.

Ghosh, B. (2014), *Basic plasma physics*, Alpha Science International.

Greenwald, R. A., and W. L. Ecklund (1975), A new look at radar auroral motions, *Journal of Geophysical Research*, *80*(25), 3642–3648.

Gurnett, D. A., and A. Bhattacharjee (2017), *Introduction to Plasma Physics: With Space, Laboratory and Astrophysical Applications*, 2 ed., Cambridge University Press.

Haldoupis, C. (2011), A tutorial review on sporadic E layers, in *Aeronomy of the Earth's Atmosphere and Ionosphere*, pp. 381–394, Springer.

Haldoupis, C., K. Schlegel, and G. Hussey (2000), Auroral e-region electron density gradients measured with eiscat, *18*(9), 1172–1181.

Hamza, A. M., and J. P. St-Maurice (1993), A turbulent theoretical framework for the study of current-driven E region irregularities at high latitudes: Basic derivation and application to gradient-free situations, *Journal of Geophysical Research: Space Physics*, *98*(A7), 11,587–11,599.

Hargreaves, J. K. (1992), *The solar-terrestrial environment: an introduction to geospace-the science of the terrestrial upper atmosphere, ionosphere, and magnetosphere*, Cambridge University Press.

Hysell, D. L., and J. Drexler (2006), Polarization of elliptic E region plasma irregularities and implications for coherent radar backscatter from Farley-Buneman waves, *Radio Science*, *41*, RS4015.

Ichimaru, S. (1973), *Basic principles of plasma physics, a statistical approach.*, W.A. Benjamin, Reading, MA (USA), 1973.

Ierkic, H. M., B. G. Fejer, and D. T. Farley (1980), The dependence on zenith angle of the strength of 3-meter equatorial electrojet irregularities, *Journal of Geophysical Research: Space Physics*, *7*(7), 497–500.

Kelley, M. C. (2009), *The Earth's ionosphere: plasma physics and electrodynamics*, vol. 96, Academic press.

Kelley, M. C., and F. S. Mozer (1973), Electric field and plasma density oscillations due to the high-frequency Hall current two-stream instability in the auroral E region, *Journal of Geophysical Research*, *78*(13), 2214–2221.

Kirkwood, S., and U. Von Zahn (1991), On the role of auroral electric fields in the formation of low altitude sporadic-E and sudden sodium layers, *Journal of Atmospheric and Terrestrial Physics*, *53*(5), 389–407.

Kissack, R. S., J.-P. St-Maurice, and D. R. Moorcroft (1995), Electron thermal effects on the Farley-Buneman fluid dispersion relation, *Physics of Plasmas*, *2*(4), 1032–1055.

Kivelson, A. (1995), *Introduction to space physics*, Cambridge university press.

Kofman, W., and E. Nielsen (1990), STARE and EISCAT measurements: Evidence for the limitation of STARE Doppler velocity observations by the ion acoustic velocity, *Journal of Geophysical Research: Space Physics*, *95*(A11), 19,131–19,135.

Kohl, H., E. Nielsen, K. Rinnert, and K. Schlegel (1992), EISCAT results during the ROSE campaign and comparison with STARE measurements, *Journal of Atmospheric and Terrestrial Physics*, *54*(6), 733–739.

Kustov, A. V., G. C. Hussey, J. A. Koehler, G. J. Sofko, and J. Mu (1995), Spectral width of type 2 coherent echoes at large magnetic aspect angles, *Journal of Geophysical Research: Space Physics*, *100*(A4), 5733–5742.

Lühr, H. (1992), In situ ionospheric current measurements during ROSE rocket flights: evidence for tilted current layers, *Journal of Atmospheric and Terrestrial Physics*, *54*(6), 725–731.

McWilliams, K. (2012), Space Weather-Institute of Space and Atmospheric Studies, [online] Available at: https://artsandscience.usask.ca/physics/isas/overview/spaceweather.php [Accessed 25 Aug. 2018].

Moorcroft, D. (2006), Origins of Radar-based Research in Canada, [online] Available at: http://www.physics.uwo.ca/ drm/history/radar/radar-history.html [Accessed 25 Aug. 2018].

Moorcroft, D. R. (1984), Propagation of plasma wave energy in the auroral E region, *Journal of Geophysical Research: Space Physics*, *89*(A5), 2963–2970.

Moorcroft, D. R. (2002), Outstanding issues in the theory of radar aurora: Evidence from the frequency dependence of spectral characteristics, *Journal of Geophysical Research: Space Physics*, *107*(A10), 1301–1309.

Ogawa, T., H. Mori, and S. Miyazaki (1976), Rocket observations of electron density irregularities in the antarctic auroral E region, *Journal of Geophysical Research*, *81*(22), 4013–4015.

Oppenheim, N. Otani, and C. Ronchi (1995), Hybrid simulations of the saturated Farley-Buneman instability in the ionosphere, *Journal of Geophysical Research: Space Physics*, *22*(4), 353–356.

Oppenheim, M., Y. Dimant, and L. Dyrud (2008), Large-scale simulations of 2-d fully kinetic farley-buneman turbulence, in *Annales geophysicae: atmospheres, hydrospheres and space sciences*, vol. 26, p. 543.

Otani, N. F., and M. Oppenheim (1998), A saturation mechanism for the Farley-Buneman instability, *Geophysical Research Letters*, *25*(11), 1833–1836.

Otani, N. F., and M. Oppenheim (2006), Saturation of the Farley-Buneman instability via three-mode coupling, *Journal of Geophysical Research: Space Physics*, *111*(A3).

Pfaff, R. (1991), Rocket observations in the equatorial electrojet : current status and critical problems, *Journal of Atmospheric and Terrestrial Physics*, *53*(8), 709 – 728.

Pfaff, R., J. Sahr, J. Providakes, W. Swartz, D. Farley, P. Klntner, I. Häggström, A. Hedberg, H. Opgenoorth, G. Holmgren, A. McNamara, D. Wallis, B. Whalen, A. Yau, S. Watanabe, F. Creutzberg, P. Williams, E. Nielsen, K. Schlegel, and T. Robinson (1992), The E-region rocket/radar instability study (ERRRIS): scientific objectives and campaign overview, *Journal of Atmospheric and Terrestrial Physics*, *54*(6), 779 – 808.

Pfaff, R. F., M. C. Kelley, B. G. Fejer, E. Kudeki, C. W. Carlson, A. Pedersen, and B. Hausler (1984), Electric field and plasma density measurements in the auroral electrojet, *Journal of Geophysical Research: Space Physics*, *89*(A1), 236–244.

Pfaff, R. F., M. C. Kelley, E. Kudeki, B. G. Fejer, and K. D. Baker (1987a), Electric field and plasma density measurements in the strongly driven daytime equatorial electrojet: 1. the unstable layer and gradient drift waves, *Journal of Geophysical Research: Space Physics*, *92*(A12), 13,578–13,596.

Pfaff, R. F., M. C. Kelley, E. Kudeki, B. G. Fejer, and K. D. Baker (1987b), Electric field and plasma density measurements in the strongly driven daytime equatorial electrojet: 2. two-stream waves, *Journal of Geophysical Research: Space Physics*, *92*(A12), 13,597–13,612.

Prakash, S., B. H. Subbaraya, and S. P. Gupta (1972), Rocket measurements of ionization irregularities in the equatorial ionosphere at thumba and identification of plasma instabilities, *Indian Journal of Radio and Space Physics*, *01*(01), 72–80.

Prikryl, P., D. Andre, J. Koehler, G. Sofko, and M. McKibben (1990), Evidence of highly localized auroral scatterers from 50-MHz CW radar interferometry, *Planetary and Space Science*, *38*(7), 933 – 944.

Providakes, J., D. Farley, B. Fejer, J. Sahr, W. Swartz, I. Hoggstrom, A. Hedberg, and J. Nordling (1988), Observations of auroral E-region plasma waves and electron heating with EISCAT and a VHF radar interferometer, *Journal of Atmospheric and Terrestrial Physics*, *50*, 339–356.

Rinnert, K. (1992), Plasma waves observed in the auroral E-region-ROSE campaign, *Journal of Atmospheric and Terrestrial Physics*, *54*(6), 683–692.

Robinson, T., and F. Honary (1990), A resonance broadening kinetic theory of the modified two-stream instability: Implications for radar auroral backscatter experiments, *Journal of Geophysical Research: Space Physics*, *95*(A2), 1073–1085.

Robinson, T. R. (1986), Towards a self-consistent non-linear theory of radar auroral backscatter, *Journal of Atmospheric and Terrestrial Physics*, *48*, 417–422.

Rogister, A., and N. d'Angelo (1970), Type ii irregularities in the equatorial electrojet, *Journal of Geophysical Research*, *75*(19), 3879–3887.

Rogister, A., and N. D'Angelo (1972), On the origin of small-scale type II irregularities in the equatorial electrojet, *Journal of Geophysical Research*, *77*(31), 6298–6299.

Rose, G., K. Schlegel, K. Rinnert, H. Kohl, E. Nielsen, G. Dehmel, A. Friker, F.-J. Lübken, H. Lühr, E. Neske, and A. Steinweg (1992), The ROSE project: Scientific objectives and discussion of first results, *Journal of Atmospheric and Terrestrial Physics*, *54*(6), 657 – 667.

Russel, R. (2014), The Ionosphere | UCAR Center for Science Education. , [online] Available at: https://scied.ucar.edu/ionosphere [Accessed 25 Aug. 2018].

Sahr, J. D. (1990), Observation and theory of the radar aurora, Ph.D. thesis, Cornell Univ., Ithaca, NY.

Sahr, J. D., and B. G. Fejer (1996), Auroral electrojet plasma irregularity theory and experiment: A critical review of present understanding and future directions, *Journal of Geophysical Research: Space Physics*, *101*(A12), 26,893–26,909.

Sato, T. (1971), Nonlinear theory of the cross-field instability:explosive mode coupling, *The Physics of Fluids*, *14*(11), 2426–2435.

Sato, T. (1973), Unified theory of type I and II irregularities in the equatorial electrojet, *Journal of Geophysical Research: Space Physics*, *78*(13), 2232–2243.

Sato, T., and T. Tsuda (1968), Erratum: Computer study of nonlinear cross-field instability, *Physics of Fluids*, *11*, 259–260.

Schlegel, K. (1992), Measurements of electron density fluctuations during the ROSE rocket flights, *Journal of Atmospheric and Terrestrial Physics*, *54*(6), 715 – 723.

Schunk, R., and A. Nagy (2009), *Ionospheres: physics, plasma physics, and chemistry*, Cambridge university press.

St.-Maurice, J. P. (1987), A unified theory of anomalous resistivity and joule heating effects in the presence of ionospheric E region irregularities, *Journal of Geophysical Research: Space Physics*, *92*(A5), 4533–4542.

St.-Maurice, J.-P. (1990), Wave-induced diffusion in the turbulent e-region, *Physics of Space Plasma*, *8*, 323.

St.-Maurice, J.-P., and J. L. Chau (2016), A theoretical framework for the changing spectral properties of meter-scale Farley-Buneman waves between 90 and 125 km altitudes, *Journal of Geophysical Research: Space Physics*, *121*(10), 10–341.

St-Maurice, J.-P., and R. Choudhary (2006), East-west and vertical spectral asymmetry associated with equatorial type I waves during strong electrojet conditions: 2. theory, *Journal of Geophysical Research: Space Physics*, *111*(A11).

St.-Maurice, J.-P., and A. M. Hamza (2001), A new nonlinear approach to the theory of E region irregularities, *Journal of Geophysical Research: Space Physics*, *106*(A2), 1751–1759.

St.-Maurice, J.-P., and A. M. Hamza (2009), Small scale irregularities at high latitudes. in "characterising the ionosphere", ed. G. Wyman, *Technical Report RTO-TR-IST-051*, *Chapter 1*, 70–95.

St-Maurice, J.-P., and K. Schlegel (1983), A theory of coherent radar spectra in the auroral E region, *Journal of Geophysical Research: Space Physics*, *88*(A5), 4087–4095.

St.-Maurice, J. P., P. Prikryl, D. W. Danskin, A. M. Hamza, G. J. Sofko, J. A. Koehler, A. Kustov, and J. Chen (1994a), On the origin of narrow non-ion-acoustic coherent radar spectra in the high-latitude E region, *Journal of Geophysical Research: Space Physics*, *99*(A4), 6447–6474.

St.-Maurice, J.-P., P. Prikryl, D. Danskin, A. Hamza, G. Sofko, J. Koehler, A. Kustov, and J. Chen (1994b), On the origin of narrow non-ion-acoustic coherent radar spectra in the high-latitude e region, *Journal of Geophysical Research: Space Physics*, *99*(A4), 6447–6474.

SteinWeg, A., D. Krankowsky, P. Lämmerzahl, and B. Anweiler (1992), Metal ion layers in the auroral lower E-region measured by mass spectrometers, *Journal of Atmospheric and Terrestrial Physics*, *54*(6), 703 – 714, doi:https://doi.org/10.1016/0021-9169(92)90108-W.

Sudan, R. N. (1983a), Nonlinear theory of type I irregularities in the equatorial electrojet, *Journal of Geophysical Research: Space Physics*, *10*(10), 983–986.

Sudan, R. N. (1983b), Unified theory of type I and type II irregularities in the equatorial electrojet, *Journal of Geophysical Research: Space Physics*, *88*(A6), 4853–4860.

Tsuda, T., and T. Sato (1968), Structure of plasma turbulence due to nonlinear cross-field instability, *The Physics of Fluids*, *11*(3), 676–678.

Watermann, J., A. G. McNamara, G. J. Sofko, and J. A. Koehler (1989), Distribution of mean Doppler shift, spectral width, and skewness of coherent 50-MHz auroral radar backscatter, *Journal of Geophysical Research: Space Physics*, *94*(A6), 6979–6985.

Wayne, R. P. (1991), Chemistry of atmospheres., *Chemistry of atmospheres., by Wayne, RP. Clarendon Press, Oxford (UK), 1991, 460 p., ISBN 0-19-855571-7,.*

Yau, A. (2013), e-POP Science, [online] Available at: https://epop.phys.ucalgary.ca/science/ [Accessed 25 Aug. 2018].